Multiscale Modeling of Non-crystalline Ceramics (Glass) (Final Report)

by George A. Gazonas, James W. McCauley, Iskander G. Batyrev,
Richard C. Becker, Sergei Izvekov, Timothy A. Jenkins, Parimal Patel,
Betsy M. Rice, Brian E. Schuster, N. Scott Weingarten,
and Raymond A. Wildman

NOTICES

Disclaimers

Army Research Laboratory

Aberdeen Proving Ground, MD 21005-5066

Multiscale Modeling of Non-crystalline Ceramics (Glass) (Final Report)

George A. Gazonas, James W. McCauley, Iskander G. Batyrev,

Richard C. Becker, Sergei Izvekov, Timothy A. Jenkins, Parimal Patel,

Betsy M. Rice, Brian E. Schuster, N. Scott Weingarten, and Raymond A. Wildman

Weapons and Materials Research Directorate, ARL

REPORT DOCUMENTATION PAGE

1. REPORT DATE (DD-MM-YYYY)	2. REPORT TYPE	3. DATES COVERED (From - To)
March 2013	Final	April 2010-November 2012

4. TITLE AND SUBTITLE	5a. CONTRACT NUMBER
Multiscale Modeling of Non-crystalline Ceramics (Glass) (Final Report)	
	5b. GRANT NUMBER
	5c. PROGRAM ELEMENT NUMBER

6. AUTHOR(S)	5d. PROJECT NUMBER
George A. Gazonas, James W. McCauley, Iskander G. Batyrev, Richard C. Becker, Sergei Izvekov, Timothy A. Jenkins, Parimal Patel, Betsy M. Rice, Brian E. Schuster, N. Scott Weingarten, Raymond A. Wildman	AH84
	5e. TASK NUMBER
	5f. WORK UNIT NUMBER

7. PERFORMING ORGANIZATION NAME(S) AND ADDRESS(ES)	8. PERFORMING ORGANIZATION REPORT NUMBER
U.S. Army Research Laboratory ATTN: RDRL-WMM-B Aberdeen Proving Ground, MD 21005-5069	ARL-TR-6353

9. SPONSORING/MONITORING AGENCY NAME(S) AND ADDRESS(ES)	10. SPONSOR/MONITOR'S ACRONYM(S)
	11. SPONSOR/MONITOR'S REPORT NUMBER(S)

12. DISTRIBUTION/AVAILABILITY STATEMENT

Approved for public release; distribution is unlimited.

13. SUPPLEMENTARY NOTES
primary author's email: <george.a.gazonas.civ@mail.mil>

14. ABSTRACT

This third-year final report describes results on the multiscale modeling of noncrystalline ceramics (glass) funded from the Director's Strategic Initiative (DSI) in support of the U.S. Army Research Laboratory's (ARL) Strategic Research Initiative. The long-term research goal of the program is to develop a concurrent multiscale computational finite element code for optimizing or enhancing the performance of various glasses against ballistic threats; the initial work focuses on pure fused-silica (a-SiO_2) and chemically varied a-SiO_2 materials. As such, this objective falls squarely within the purview of the Weapons and Materials Research Directorate, since multiscale models are constitutive models (specific to a particular material) wherein time-evolving short- and intermediate-range atomic structure, order, and microcrack initiation and growth are fully coupled to the macroscale, a phenomenon that cannot be modeled or accounted for using classical homogenization methods. A more immediate research objective is to understand why certain chemically substituted a-SiO_2 materials exhibit enhanced performance when defeating shaped-charge jets and other ballistic threats.

15. SUBJECT TERMS multiscale modeling; fused silica; amorphous quartz; molecular dynamics; quantum mechanics; shaped charge jet; Director's Strategic Initiative (DSI)

16. SECURITY CLASSIFICATION OF:			17. LIMITATION OF ABSTRACT	18. NUMBER OF PAGES	19a. NAME OF RESPONSIBLE PERSON
a. REPORT	b. ABSTRACT	c. THIS PAGE	UU	128	George A. Gazonas
Unclassified	Unclassified	Unclassified			19b. TELEPHONE NUMBER (Include area code) 410-306-0863

Contents

List of Figures

List of Tables

Intentionally left blank.

1. Introduction

Non-crystalline (amorphous) ceramics or ceramic glasses are used in a variety of vital Army personnel, ground, and air vehicle applications that require transparent armor—it is ubiquitous in tactical vehicular windshields and side windows. Ceramic glass is inexpensive and formable into large, flat plate, and curved shapes. For many years it has been known that the properties of glass can be modified and enhanced through compositional modification, chemical strengthening, annealing, and process control of melt cooling. Glass ceramics, the controlled crystallization of nanosized single crystals in a glass matrix, offer another avenue for designed and enhanced property modifications for transparent and opaque material applications. In addition, certain glass formulations have been shown to exhibit enhanced performance against shaped-charge jets (SCJs) (figure 1) and other ballistic threats, but it is not understood why. This is in part due to various short- and longer-range atomic structural characteristics including atomic free volumes, cation coordinations, bridging and non-bridging oxygen (O) atoms, bonding energies, and nanoscale order characteristics (short and longer range) that are difficult or impossible to quantify experimentally for ceramic glass.

In contrast, crystalline ceramics like silicon carbide (SiC), aluminum oxynitride ($AlON$), and others have easily characterizable microstructures/mesostructures, which consist of assemblies of individual single-crystal grains. Ceramic glasses, on the other hand, do not have a conventional micro- or mesostructure, as it is understood for crystalline ceramics. However, there are microstructural-scale variations in ceramic glass that may include density variations from atomic free volume variations or microporosity, size of local atomic order, defects (inclusions, large pores, etc.), and others yet to be determined. The interaction of a stress/shock wave from a dynamic impact involves many structural changes not easily characterized by conventional equations of state and can involve reversible and irreversible densification and changes in bulk short-range order structures comparable to phase changes in crystalline ceramics. For example, in simple Hertzian indentation testing, a wide range of plastic or inelastic deformation mechanisms have been observed in a variety of glasses. Multiscale computational design methodologies (figure 2) for this class of materials will, nevertheless, require quantitative and possibly statistically based descriptions of the mesoscale, although current efforts to develop such models have fallen far short of this goal.

(a)   (b)
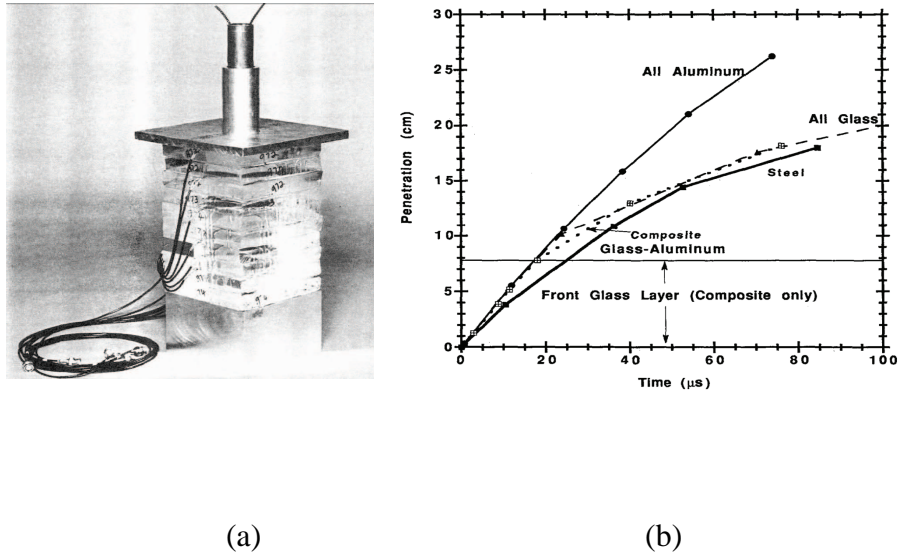
Figure 1. Enhanced performance of SCJs into glass (a) test configuration for glass targets, and (b) penetration vs. time for several targets, after Moran et al. (*1*).
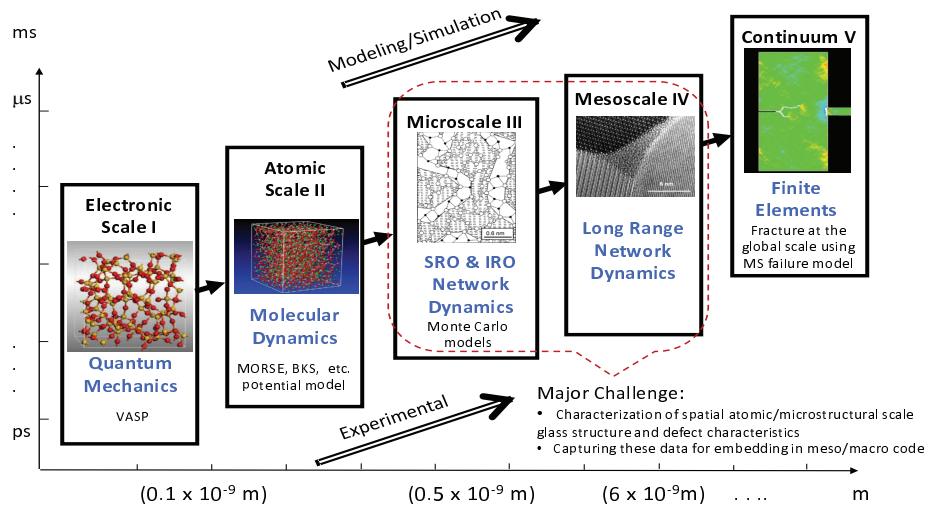
Figure 2. A multiscale model for non-crystalline ceramics (glass).

2

Our specific long-term research goals are threefold:

1. Develop molecular dynamics (MD) process models for a series of chemically substituted amorphous silica (a-SiO_2 or fused silica) materials for the prediction of glass elastic properties assuming completely uniform glass "mesostructures." If successful, such models will enable ab initio prediction of structure-property relations in glass that will be validated with experimentally determined elastic properties.

2. Extend the MD models to study densification of chemically substituted a-SiO_2 materials under high pressures (∼60 GPa Materials in Extreme Dynamic Environments [MEDE]) relevant to ballistic events where reversible and irreversible density changes and structural transformations have been observed. If successful, such models will enable ab initio prediction of a-SiO_2 compressibility, kinetics, and "glass" phase transformations that will be used to develop equations of state for a-SiO_2 materials, and thus form a direct link to the continuum scale.

3. Develop a fully validated multiscale finite element computational model and code incorporating the effects of reversible and irreversible densification, inelastic deformation, and overlain by a spatiotemporally evolving population of growing defects, which coalesce and ultimately lead to fracture and fragmentation. It is envisioned that at some time in the not too distant future, fully concurrent multiscale computational finite element codes will be used by analysts on a regular basis for optimal material design.

1.1   Organization of the Report

The remainder of the report is organized as follows. General program objectives are outlined in section 2, and the approach for modeling the multiscale behavior of glass appears in section 3. Experimental work on various glasses is described in section 4, which is highlighted by indentation experiments, edge-on-impact ballistic experiments, ballistic impact and fragmentation studies conducted at the Ernst-Mach Institute, and high pressure diamond anvil cell experiments conducted at the U.S. Army Research Laboratory (ARL). Section 5 describes the development of a new short-range pairwise potential for silica using ab initio molecular dynamics (AIMD) methods; the discovery of an $O - O$ soft repulsive shoulder in silica may explain multi-stability behavior of glasses under pressure and anomalous densification behavior. The new potential is used to simulate glass nanoindentation experiments, described earlier in section 4.2.1. Section 6 introduces similarity analysis for elastic media that exhibit fracture induced by indentation; a universal scaling law is derived, which is invaluable for validating computational methods

capable of simulating crack propagation. The mechanics of indentation is studied in section 7, where fully three-dimensional stress and displacement fields are presented, which are also useful for verification of computational simulation methods. First principles quantum mechanical methods are used to model densification and bulk modulus variation with pressure in section 8. Since inelastic deformation and a polyamorphic transformation occurs simultaneously in fused silica, a model is developed to account for this coupled behavior in section 9 and compared to plate impact experiments. A peridynamics computational code (section 10) has been developed to enable modeling of quasistatic and dynamic fracture observed in glasses. Initial efforts to model indentation experiments and validation with the universal scaling law are described in section 6. Section 11 outlines a one-day short course on the "Fundamentals of Glass Science," that was taught by Professor Arun K. Varshneya, Alfred University, at ARL on October 29, 2010. Course attendees received copies of Varshneya's *Fundamentals of Inorganic Glasses* (*26*). A short-term conceptual project to determine an effective experimental and theoretical approach to model and characterize the role of glassy materials in resisting ballistic impact was conducted by Professor Richard Lehman, Rutgers University, detailed in section 12. Section 13 describes ARL's new glass processing facility and our initial efforts in processing borosilicate systems for evaluation in the transition of this program to the Weapons and Materials Research Directorate's (WMRD) core mission in fiscal year 2013 and beyond. Section 14 summarizes the conclusions of this final report. Metrics including presentations, publications, hires, and transition of the DSI program to a core mission program within WMRD are listed in section 15.

2. Program Objectives

The long-term research goal of the program is to develop a concurrent multiscale computational finite element code for optimizing or enhancing the performance of various glasses against SCJs; the initial work focuses on pure a-SiO_2 and chemically varied a-SiO_2 materials. As such, this objective falls squarely within the purview of the WMRD, since multiscale models are constitutive models (specific to a particular material) wherein time-evolving microstructural changes, such as microcrack growth, are fully coupled to the macroscale, a phenomenon that cannot be modeled or accounted for using classical homogenization methods. A more immediate research objective is to understand why certain chemically substituted a-SiO_2 materials exhibit enhanced performance in the defeat of SCJ and other ballistic threats.

Our program objectives are threefold:

1. Develop MD process models for a series of chemically substituted a-SiO_2 materials to predict glass elastic properties. This glass plays an important role in many technological applications and its structure has been inferred from neutron-diffraction, nuclear magnetic resonance, and small-angle x-ray scattering (SAXS) analysis to reveal a three-dimensional network consisting of tetrahedrally coordinated silicon (Si) whose structure is constant throughout the glass and defines its short-range order (SRO). Long-range disorder in the structure is manifested by a seemingly random variation in the Si-O-Si bond angle in adjacent tetrahedra. Despite the intense study of a-SiO_2 glass over the last several decades, much controversy still exists on the best method to model (i.e., via density functional theory, MD, Monte Carlo methods, or master equation techniques) this archetypal material to predict of elastic properties, diffusivity, surface interactions, bond angle distribution, polyamorphism, and melt solidification. Current models in the literature are often not fully validated and progress towards this goal will be made when model predictions of elastic constants for a series of chemically substituted a-SiO_2 glasses agree with experimentally determined constants.

2. Extend the MD models to study densification of chemically substituted a-SiO_2 materials under high pressures. Since long-range order in glass is non-existent, variations in the SRO and intermediate range order (IRO) must be responsible for the enhanced performance observed in ballistic tests on certain a-SiO_2 glasses. If this is the case, it may be possible to use MD models to predict macroscopic ballistic performance. Since glass is subjected to extreme pressure and temperature during an SCJ event, it will be necessary to study the relationship between compressibility, kinetics, and phase transitions during high-pressure densification of a-SiO_2 glasses as manifested by changes in coordination number, ring size, and free volume. Progress towards this goal will be made when MD-derived equations of state (EOSs) agree with those obtained experimentally via diamond anvil press and plate impact experiments.

3. Develop a fully validated multiscale finite element computational model and code that incorporates the effects of reversible and irreversible densification and inelastic deformation, overlain with a spatiotemporally evolving population of defects that grow, coalesce, and ultimately lead to fragmentation. This objective will develop a computational framework to combine the objectives from (1) and (2), and incorporate the influence of fracture initiation, growth, coalescence, and fragmentation of surface and volume defects in glass into a comprehensive concurrent multiscale finite element model and code. Microcrack initiation, growth, and coalescence (sometimes referred to as failure waves) is a multiscale phenomenon that bridges all scales in a-SiO_2 glasses despite the apparent absence of a structural mesoscale for this class of materials (figure 2). Algorithms to develop fully two-way coupled multiscale

codes are in their infancy, and progress on this objective will be realized with the successful development and implementation of a consistent scheme for coarse-graining localization phenomena such as fracture failure observed in glass.

3. Planned Approach

The planned approach consists of three components, which are outlined in figure 3:

1. *Validate the MD models for a series of chemically substituted a-SiO_2 materials to predict glass elastic properties.* Although there is no effort within WMRD to predict a-SiO_2 elastic properties, a hierarchical multiscale modeling effort is currently underway, which is focused on the study of polycrystalline ($\sim$200 μm grain size) $AlON$ and validation of quantum and MD predictions of anisotropic elastic constants using diamond anvil cell (DAC) and focused-ion-beam (FIB)/scanning electron microscopy (SEM) compression tests on oriented $AlON$ single crystals (*27*). We plan to use MD methods (with possible MD coarse-graining) to simulate glass process modeling during melt solidification by quenching a high-density, high temperature, and pressure (with possible polyamorphic phases) melt for a series of chemically substituted a-SiO_2 materials. Next, the resulting room-temperature, chemically modified structures will be reversibly deformed to predict the elastic properties that will be validated with experimentally determined elastic properties.

2. *Validate the MD models for densification of chemically substituted a-SiO_2 materials under high pressures.* Although there is currently no effort within WMRD to predict the EOS of chemically substituted a-SiO_2 materials, MD methods have been used to predict high-pressure densification in these materials. MD simulations of pure a-SiO_2 materials reveal a Hugoniot elastic limit (HEL) of about 10 GPa, and an anomalous maximum in compressibility at around 3 GPa. Experiments where samples have been compressed to pressures lower than 10 GPa are indistinguishable from the original material, whereas above 10 GPa, materials can sustain an irreversible density increase from 10%–20% higher than the starting material, although there is controversy as to whether the mechanism is due to irreversible coordination defects or permanent ring size modification. In contrast to the behavior of a-SiO_2, crystalline quartz (α-SiO_2) undergoes very well-known high pressure polymorphic phase transitions into a Coesite phase and a Stishovite phase (figure 4), which involve changes in coordination of the Si cation from four to six O atoms. A combination of

6

FY11	FY12	FY13	FY14	FY15

Glass (DSI)

I. Glass Fabrication

FY12: Fabricate pure & chemically substituted a-SiO2 mat'ls (fused silica)

II. Glass Characterization

FY11: • Evaluate a-SiO2 samples in ballistic & SCJ tests • Glass Technology Short Course (October 2010) • Experimental determination of microstructural scale variations in glass (SRO & LRO)

FY13: • Quantitative description of initial defect distributions in a-SiO2 materials • Radial distribution function measurements

FY14: • Novel metrics to predict ballistic performance based on MD model results

III. Quantum & Molecular Dynamics of Glass

FY11: • MD process models of pure & chemically substituted a-SiO2 mat'ls validated by SRO & bond length distributions from II

FY13: • MD process models for densification of pure & chemically substituted a-SiO2 materials for Analytical EOS development

IV. Meso/Macroscale Modeling and Validation

FY12: • Validate MD model predictions of elastic properties w/ experiments • Begin evaluation of coarse-graining algorithms (CZ->XFEM)

FY13: • Develop analytical EOS based for chemically substituted a-SiO2 materials • Validate MD model densification predictions w/plate impact experiments

FY14: • Implement EOS into continuum codes & validate w/analysis & experiments

FY15: • Concurrent multiscale computational code for a-SiO2 materials

V. Fundamental Aspects of Glass Deformation & Failure

FY13: • Coherent gradient sensing/high-speed imaging experiments on pure & chemically substituted a-SiO2 mat'ls • Plate impact experiments on pure & chemically substituted a-SiO2 mat'ls

FY14: • Fragmentation experiments on a-SiO2 mat'ls

FY15: • Implement & validate coarse-graining algorithms for mat'l failure of a-SiO2 mat'ls

Figure 3. Five-year roadmap consistent with the WMRD brittle materials program.

diamond anvil press and plate impact experiments will be conducted on a series of chemically substituted a-SiO_2 materials and compared with MD densification simulations in glass in order to understand the influence of glass modifiers on changes in the shock response of these materials. EOSs for a subset of promising chemically substituted materials will be developed and implemented into a continuum code to determine if any of the chemically substituted materials exhibit enhanced ballistic performance.

3. *Develop a fully validated multiscale finite element computational model and code that incorporates the effects of reversible and irreversible densification and inelastic deformation overlain with a spatiotemporally varying population of defects that grow, coalesce, and ultimately lead to fragmentation.* The ultimate research objective is to develop a physics-based multiscale computational finite element code for studying densification and
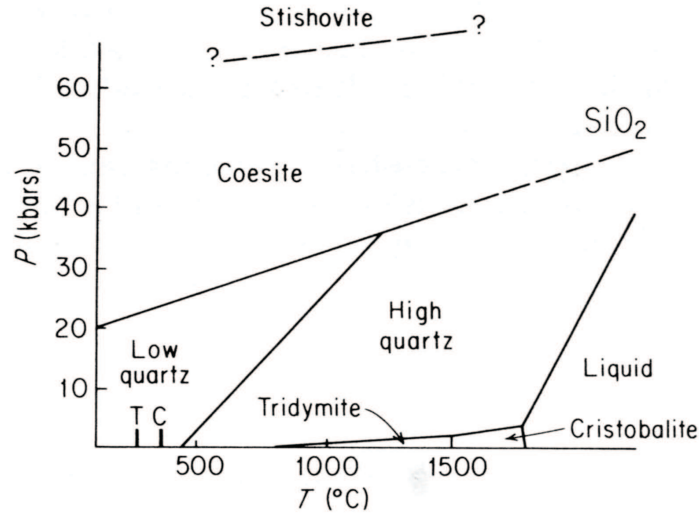
Figure 4. Crystal structures of quartz, after Frye (*2*).

dynamic fracture in non-crystalline ceramics (see figure 2). Atomistic behavior will be linked to macroscopic elastic properties and densification behavior through development of an EOS from first principles as outlined in components (1) and (2). At this stage, what remains to be accomplished, is to successfully link, in a concurrent fashion, multiscale failure phenomena in a-SiO_2 materials by incorporating the important role that pre-existing surface and volume defects have on the microcrack growth, coalescence, and fragmentation in this class of materials. Over the past five years, the first author has also been directly involved in development of a parallel, concurrent multiscale code for heterogeneous viscoelastic composites (*28*) under the auspices of an ARL/University of Nebraska cooperative agreement, which will be leveraged and used as the framework for the development of a concurrent multiscale model of a-SiO_2 materials.

The chief challenge for brittle materials is to correctly account for the growth kinetics of microcracks in a multiscale computational environment. The propagation of free internal boundaries at lower scales will be "coarse-grained" to higher scales, where global fracture failure and fragmentation is observed. As such, coarse-graining algorithms will need to be validated through continuum-scale experiments on a-SiO_2 materials that measure dynamic crack propagation speeds, mixed-mode failure, and crack bifurcation phenomena using coherent gradient sensing and high-speed imaging techniques; ARL possesses capabilities for

8

conducting such dynamic fracture experiments in a-SiO_2 materials through the recent establishment of a coherent gradient sensing/imaging facility funded by the ongoing multiscale modeling effort of $AlON$. Models and validation of the initiation and propagation of discrete fractures in a-SiO_2 materials should transition naturally into models of fragmentation and comminution for behind-armor-debris applications. Fragmentation experiments have classically been conducted using dynamically expanding ring experiments for defining fragment size versus strain rate and will be used to validate computational models of fragmentation. The development of consistent coarse-graining algorithms for fracture in materials, which is associated with failure and loss of material stability, is largely unexplored and is the primary high-risk goal of this section.

4. Experimental Work and Background

4.1 Background

4.1.1 Compositions

Silicate-based ceramic glasses are based on chemical substitutions into a SiO_4 tetrahedral-based polymeric-like structure; fused silica is an amorphous (non-crystalline) form of pure SiO_2. Table 1 lists the compositions and properties of typical glasses.

Table 1. Glass compositions in % and selected properties.

Glass	SiO_2	Al_2O_3	CaO	B_2O_3	Na_2O	K_2O	ρ (g/cm^3)	E (GPa)	ν
Borofloat	80.5	2.5	0.02	12.7	3.55	.64	2.23	62.3	.207
Starphire	73.2	1.44	10.27	-	14.72	.01	2.51	72.3	.23
Fused Silica	100	-	-	-	-	-	2.2	73.0	.17

4.1.2 Structural Characteristics of Ceramic Glasses

Simplistically, the predominant macro-characteristics (micron and larger) can be a variety of defects including inclusions, bubbles, large pores, and residual compressive or tensile stress. The notion of an array of crystalline grains separated by grain boundaries (a microstructure) does not exist in glass. Rather, there is a complete lack of long-range order, but short- and intermediate-range order at the nanostructural scale:

- Short-range order: Mostly atom to atom bond lengths, less than 0.5 nm and bond angles; characterized by radial distribution functions (RDFs) and SAXS.

- Intermediate-range order: In silica-based glasses, this is the polymerization of the silica atomic tetrahedra (one Si atom surrounded by four oxygen atoms) into various size ring structures of joined tetrahedra, which can consist of 4, 5, 6, 7, 8, or so ring groups of tetrahedra. Substitution of other cations (Na, K, Mg, Ca, etc.) and B into silica-based glasses can have profound effects on the IRO. It is also important to note that B bonds to three oxygen atoms in flat triangles.

- Free-volume: In crystalline materials, using the theoretical density, it is straightforward to calculate the atomically unoccupied free space. In glasses, this unoccupied atomic space is referred to as "free volume," but because of an unknown periodic structure, it is extremely difficult to quantify in glasses. The free volume plays a critical role in glass densification under stress/pressure.

- There can be significant complex spatial variations of defects, free volume, atomic structure, and resulting properties at the nanoscale.

- It is the current wisdom of the glass community that the short- and intermediate-range order at the nanoscale in glasses can have a significant influence on some properties.

4.1.3 Effect of Stress/Pressure

Deformation and failure in ceramic glasses begins with reversible to irreversible densification and/or critical cracks nucleating at defects:

- High pressure can have significant effect on coordination of Si changing from typical fourfold to sixfold coordination of oxygen around Si - (quartz-like to coesite-like to stishovite-like structures, as for crystalline quartz shown in figure 4).

- The degree of polymerization or distribution of the ring structures can also change as a function of pressure.

- The common consensus is that the ring distribution is the primary control of some properties; however, at very high pressures, the change from four to sixfold Si coordination will significantly influence properties as well.

- Some properties of fused silica (pure SiO_2 glass) are anomalous, e.g., a negative change in shear modulus as a function of pressure. Bando et al. (*3*) show that the radius of curvature of a crack in glass (figure 5) can be about 1.5 nm, suggesting that the IRO can significantly influence crack propagation.
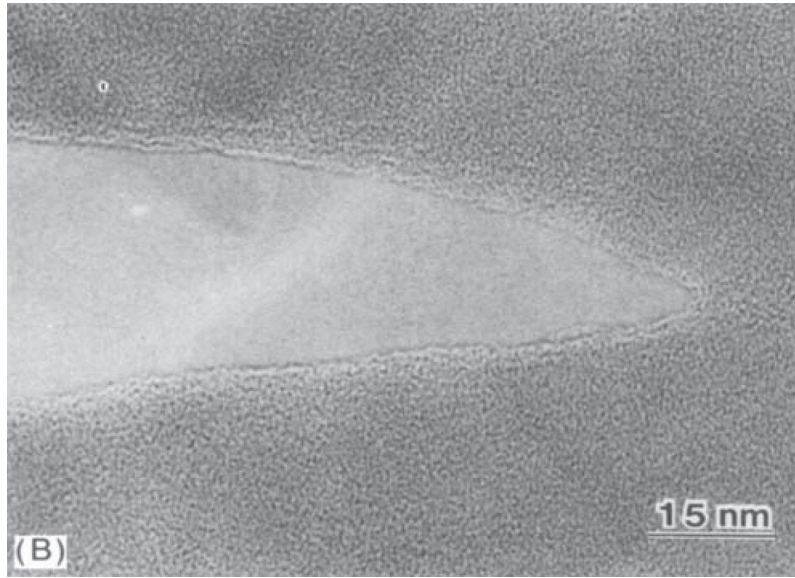
Figure 5. The radius of curvature of a crack in glass after Bando (*3*).

4.1.4 Plasticity in Glass

Ito (*4*) has presented fairly simple methods of determining the brittleness (figure 6) or, conversely, the plasticity of glasses, which he uses to suggest that the brittleness is dependent of IRO or the distribution of ring structures seen in figure 7. Table 2 lists values for the brittleness parameters.
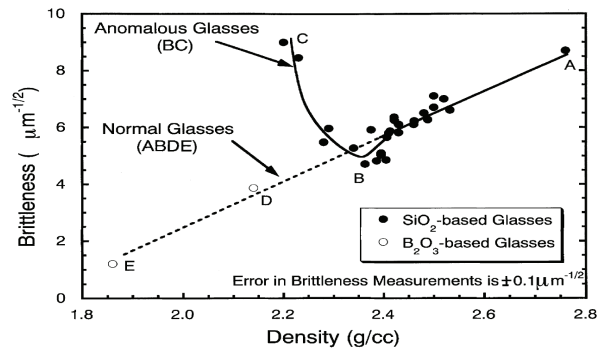
Figure 6. Brittleness vs. density for glasses in the SiO_2 and B_2O_3-based glasses, after Ito (*4*).

(a)

(b)
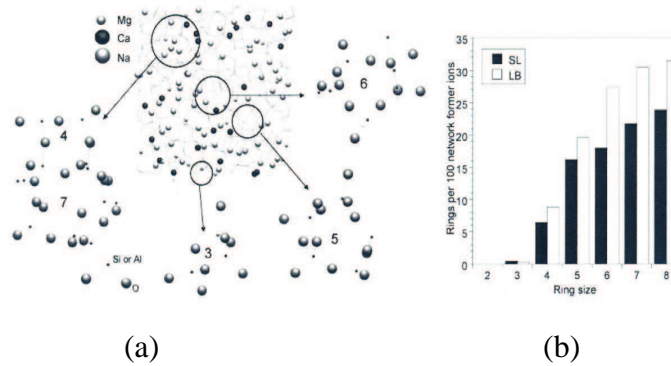
Figure 7. (a) Structure of soda lime glass by MD simulation where the number shown is the ring size and (b) Number of network rings in soda lime (SL) and less brittle (LB) glasses; LB glass are more polymerized than SL glass after Ito (*4*).

Table 2. Brittleness parameters.

Glass	Brittleness Parameter (μm$^{-1/2}$)
Fused Silica	~10
B_2O_3 Based glass	~1
Soda Lime	~5 - 7

The brittleness, therefore, seems to be dependent on the deformation and fracture behavior, which depends on flow and densification before crack initiation and on the bond strength of the network and seems to decrease with a decrease in density—a free volume effect. This is addressed by Ito (*4*) in the same paper.

Conclusions from this work are as follows:

- Both glasses are commercial SL based glasses: $(Na, K)_2O - (Mg, Ca)O$ - SiO_2.

- The LB glass appears to have a higher polymerized network than the SL glass, i.e., a significant difference in the ring structure distribution.

- IRO at the nanoscale seems to be controlling the brittleness of these glasses.

4.2   Experimental Results

The absorption/dissipation of deposited energy in an extreme impact event depends on the various deformation and failure/fracture mechanisms that are activated during the event. In addition, in a multiscale modeling and simulation "Protection Materials by Design" approach, it is absolutely critical to experimentally determine the key properties at the various scales to validate the theoretical computational results. We have used various quasi-static indentation, edge-on-impact (EOI), and ballistic impact tests for this purpose.

4.2.1   Indentation

Studies on the deformation and fracture of glasses and AlON using a spherical 500-μm-diameter diamond indenter was recently carried out by Wilantewicz (*5*). Results for a SL (Starphire), boron substituted glass (Borofloat), fused silica, and AlON are illustrated in figure 8 and tables 3 and 4. There are significant differences in the deformation and fracture behavior of these materials.
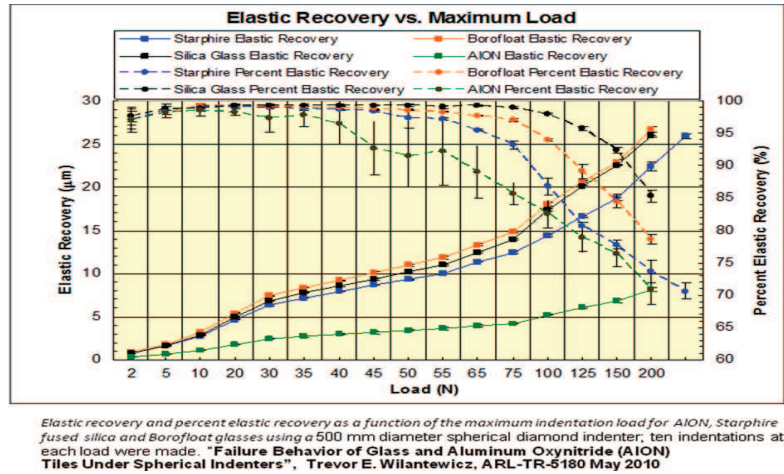
Figure 8. Elastic recovery vs. load for a variety of glasses after Wilantewicz (5).

Table 3. Elastic recovery in
indentation tests at 200 N.

Material	% Elastic Recovery
AlON	71
Starphire	73
Borofloat	79
Fused silica	86

Table 4. Deformation and fracture loads after Wilantewicz (5).

Material	Onset Dimpling (N)	All Tests Dimpled (N)	Onset Ring Cracking (N)	All Tests Ring Cracked (N)	Onset Radial Cracking (N)	All Tests Radial Cracked (N)
Starphire (tin)	30	30	65	75	75	100
Starphire (air)	20	30	65	100	100	125
Borofloat (tin)	30	35	30	45	100	200
Silica Glass	75	100	20	30	65	75
AlON	35	45	45	65	40	75

14

It is clear that these materials behave in significantly different ways. The onset of dimpling is the result of a permanent plastic deformation. The normal expectation for these materials is that as a function of increasing indentation load the material response would proceed through an elastic regime, then through a plastic regime, and finally into a cracking/fracturing regime. Table 5 summarizes the observations. Silica glass (fused silica), however, behaves in a dramatically different way, fracturing prior to a plastic mechanism.

Table 5. Onset of elastic, plastic, and
fracture responses after
Wilantewicz (5).

Material	Response
Starphire:	elastic → plastic → fracture
Borofloat:	elastic → plastic → fracture
Silica Glass:	elastic → fracture → plastic
AlON:	elastic → plastic → fracture

4.2.2 Edge-on-impact Studies of Fused Silica

The experimental arrangement is illustrated in figure 9 and a series of time-resolved photographs are presented in figure 10.
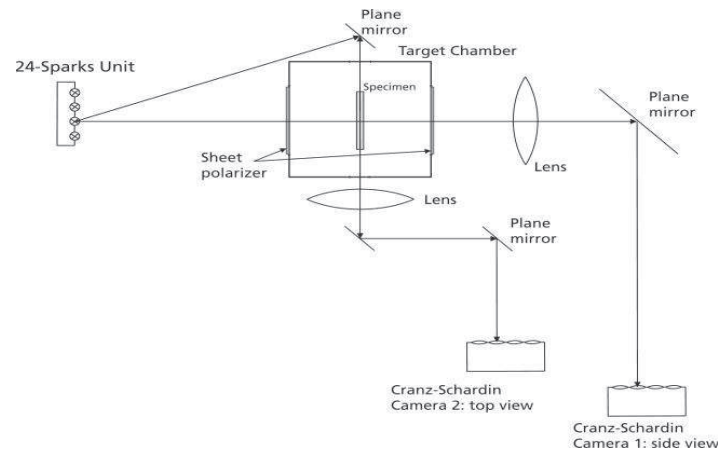
Figure 9. EOI experimental arrangement after Strassburger et al. (6).

(a)   (b)
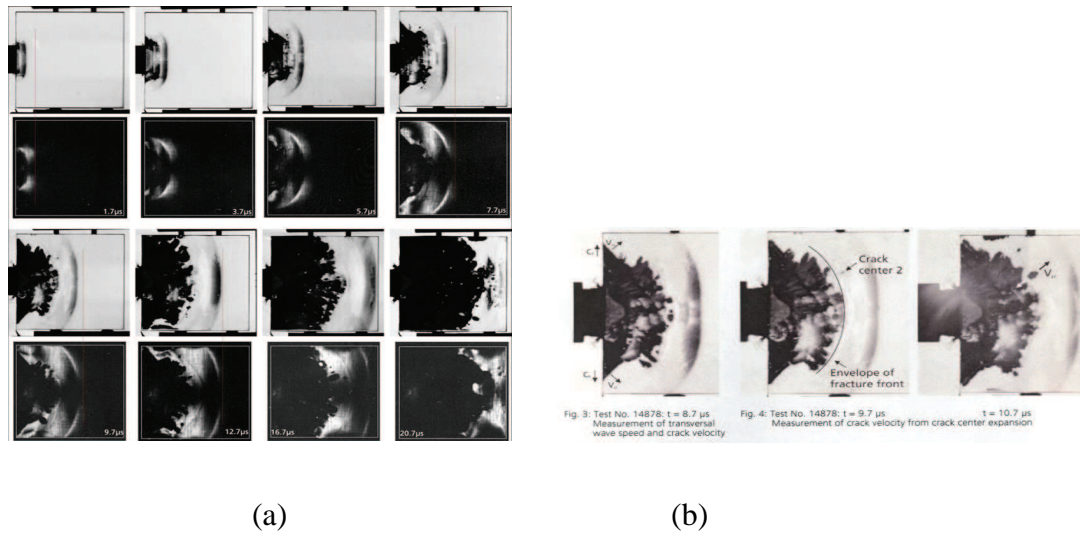
Figure 10. (a) Illustration of a series of EOI tests in fused silica by a solid steel
             cylinder at 350 m/s at various times; first and third rows illustrate
             shadowgraph photographs in plane light showing damage; second and
             fourth rows are photos in crossed polarized light, which show the
             propagation of stress via a photoelastic effect; and (b) illustrates the
             irregular nature of the damage front due to the presence of
             macro-defects from the same test after Strassburger et al. (*6*).

Table 6 lists the measured velocities of the longitudinal waves, transverse waves (shear waves), and crack and damage front velocities in fused silica. Note that the longitudinal wave velocity for fused silica is 5.93 km/s and the shear wave velocity is 3.77 km/s.

Table 6. Compilation of measured wave, crack, and damage velocities in fused silica after Strassburger et al. (*6*).

Impact velocity (m/s)		150	260	350
Longitudinal wave speed (m/s)	shadowgraphs	5975	6076	5823
Longitudinal wave speed (m/s)	crossed polarizers	5814	5796	5491
Transverse wave speed (m/s)	shadowgraphs	-	3500	3670
Crack velocity (m/s)	shadowgraphs	2234	2149	2120
Damage velocity (m/s)	shadowgraphs	5641	5728	5121

4.2.3 Visualization and Analysis of Ballistic Impact Damage and Fragmentation in Various Glass Plates

In this series of experiments Borofloat, Starphire, and fused silica were tested in a standard ballistic configuration. The plates were impacted by a 7.62-mm armor-piercing (AP) round, and a solid steel cylinder inside of a box to contain all of the resulting fragments. The fragments were removed from the box with a vacuum and then sorted by sieves. Figure 11 illustrates the experimental arrangement.

Table 7 lists the details of the various tests conducted on the three glass types. Note that the dimensions of the Borofloat glass plate used in test, #17742, were significantly different than the others, which has skewed the fragmentation results at the largest sieve size 2 mm. Figure 12 illustrates a series of very-high-speed photographs as a function of time for the four tests listed in table 7.

Table 7. Test parameters with different types of glass.

EMI Test No.	Type	Dimensions (mm)	Thickness (mm)	Projectile	Impact Velocity (m/s)
17742	Borofloat	149.4 x 149.7	12.94	cylinder	1089
17749	Fused silica	101.65 x 101.67	12.75	cylinder	1107
17750	Fused silica	101.62 x 101.62	12.75	7.62 AP	824
17751	Starphire	99.9 x 99.7	10.06	cylinder	1115

(a)   (b)
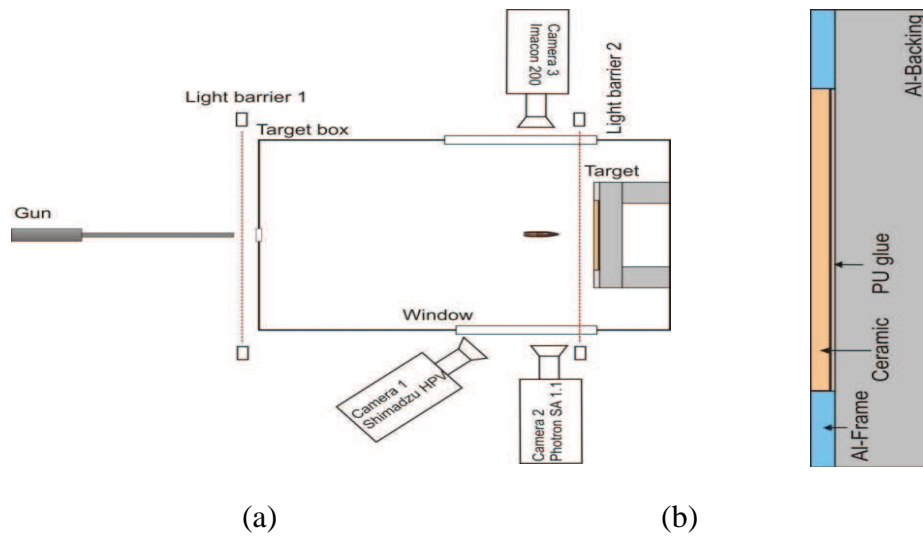
Figure 11. Schematic of (a) ballistic test configuration and (b) target after
            Strassburger et al. (7).

#17751; soda lime; v_P =   #17742; Borofloat,   #17749; fused silica;   #17750; fused silica;
1115 m/s; Solid cylinder   solid cylinder; 1089 m/s solid cylinder; 1100 m/s   7.62 AP; 800 m/s
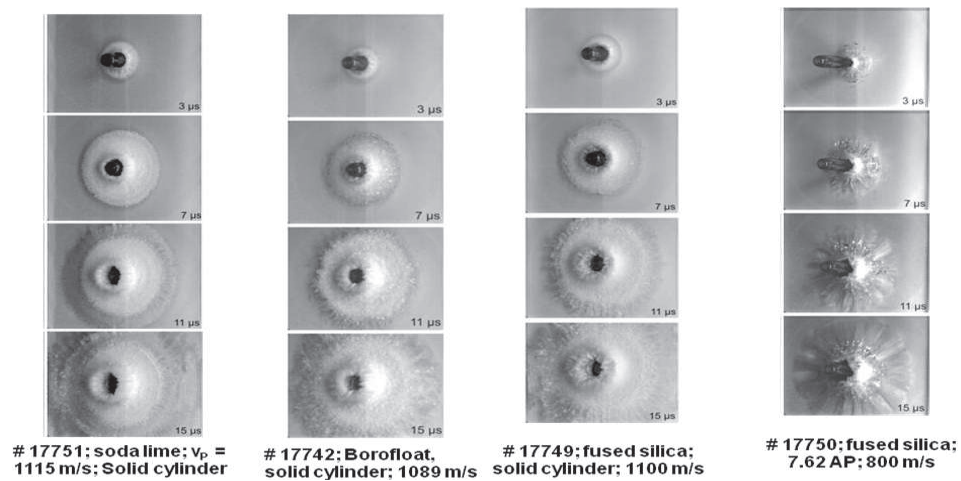
Figure 12. Selection of high-speed photographs from impact on various glasses
            after Strassburger et al. (7).

18

The observed propagation velocities of the damage zone under impact of the steel cylinder are all below the transverse wave velocities of the materials, as seen in table 8, which compiles the wave and fracture velocity data determined from EOI tests along with data from the actual test series. When fused silica was impacted by the 7.62-mm AP projectile, the formation of single radial cracks were observed, which propagated at an average velocity of 2394 m/s, which is in very good agreement with the crack velocity determined for fused silica from EOI tests.

Table 8. Compilation of wave and fracture velocity data after Strassburger et al. (*7*).

Glass Type	Longitudinal Wave Velocity (m/s)	Transverse Wave Velocity (m/s)	Terminal Crack Velocity (m/s)	Damage Velocity (m/s)
Starphire	5890	3570	1580	3073[⊕]
Borosilicate	5543	-	2034	2857[⊕]
Fused Silica	6021	3858	2400	3007,[⊕] 2394[†]

[⊕] steel cylinder, $v = 1100$ m/s

[†] AP projectile, $v = 824$ m/s

4.2.4   High-speed Photography

The three types of glass tested exhibited a very similar fracture pattern under impact of a steel cylinder at 1100 m/s. A circular damage zone developed around the impact site, in which the glass was strongly fragmented and no single cracks could be distinguished during the first 10 μs after impact. After this first damage propagation phase, single cracks became discernible at the perimeter of the damage zone. In the following, a severely damaged inner zone and an outer zone with a lower fracture density could be distinguished. Selections of 16 high-speed photographs from each test with the cylindrical projectile are presented in figures 13, 15, and 17. The analysis of damage propagation revealed different velocities with the three types of glass. The corresponding path-time histories are depicted in figures 14, 16, and 18.

When fused silica was impacted by the 7.62-mm AP projectile the formation of single radial cracks could be observed, which propagated at an average velocity of 2394 m/s. This is in very good agreement with the crack velocity determined for fused silica from EOI tests (*29*). A selection of 16 high-speed photographs from the AP projectile impact on fused silica at 824 m/s is presented in figure 19. The corresponding path-time history of fracture propagation shows the diagram in figure 20.
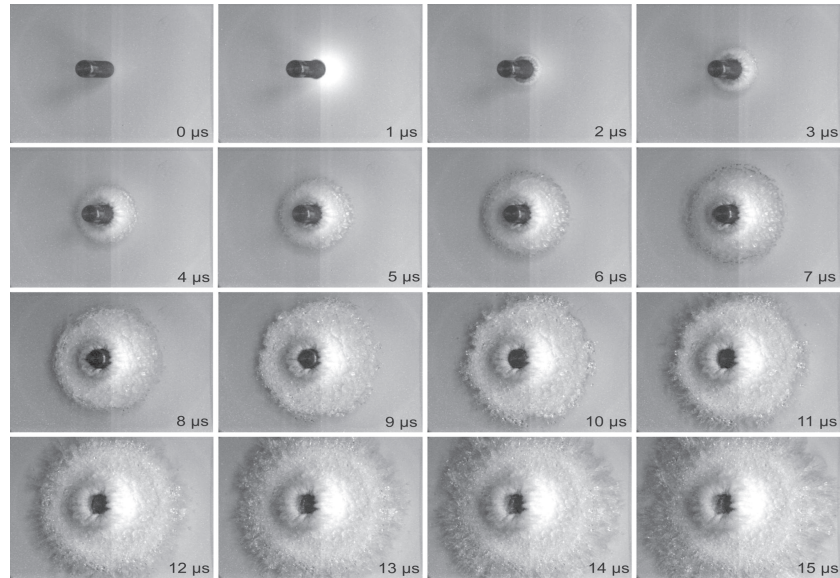
Figure 13. Selection of high-speed photographs from impact on Borofloat glass at 1089 m/s; Test #17742 .
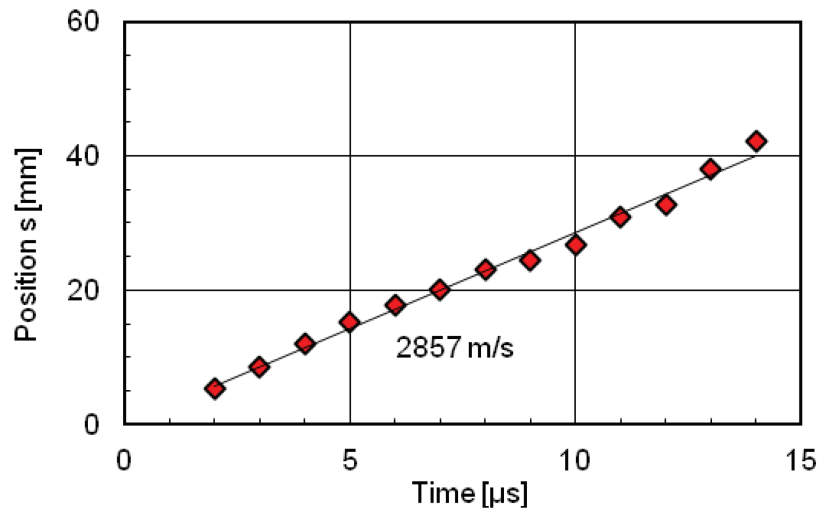
Figure 14. Position-time history of damage propagation in Borofloat glass at 1089 m/s; Test #17742 .
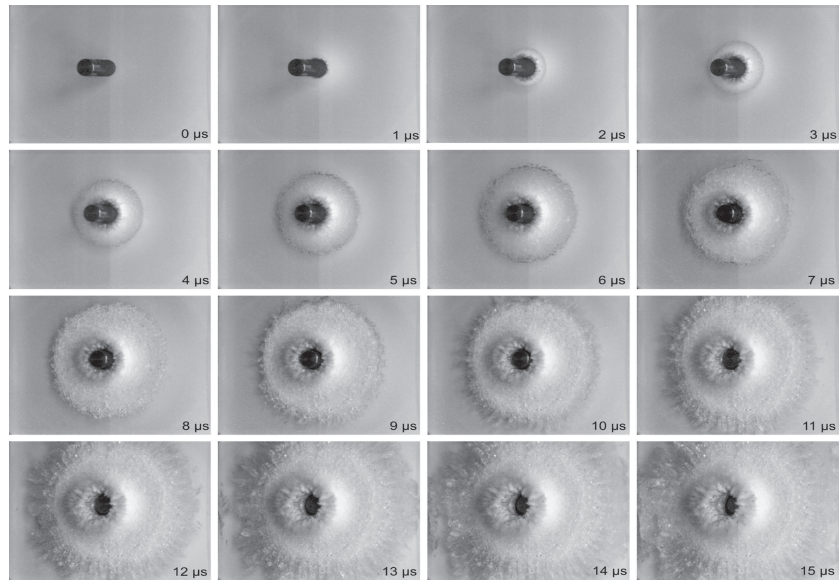
Figure 15. Selection of high-speed photographs from impact on fused silica glass at 1107 m/s; Test #17749 .
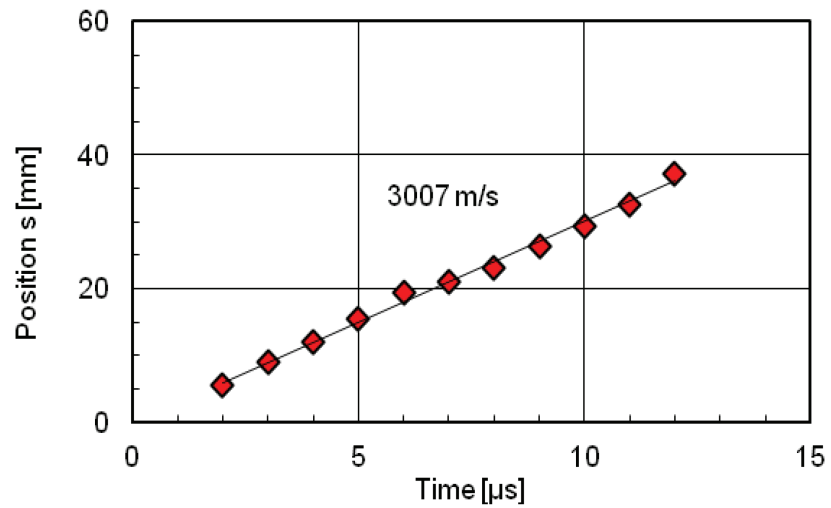
Figure 16. Position-time history of damage propagation in fused silica glass at 1107 m/s; Test #17749 .
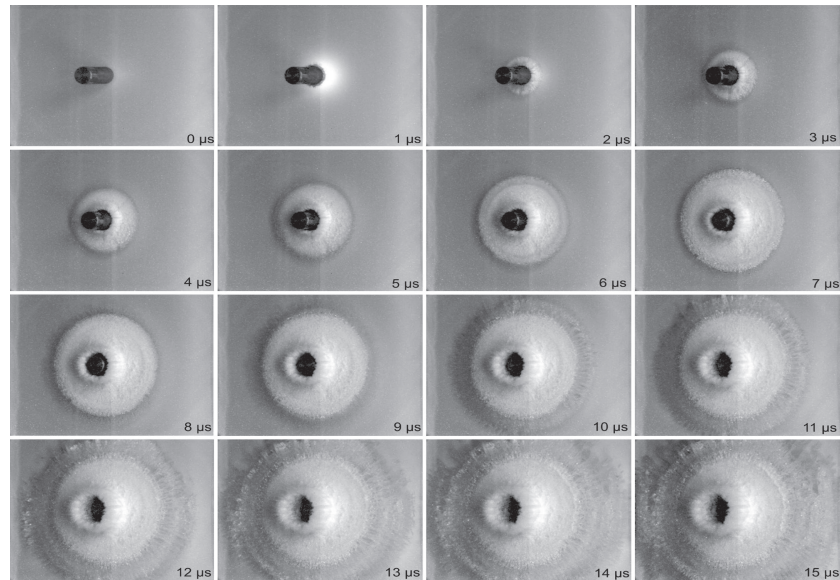
Figure 17. Selection of high-speed photographs from impact on SL glass at 1115 m/s; Test #17751 .
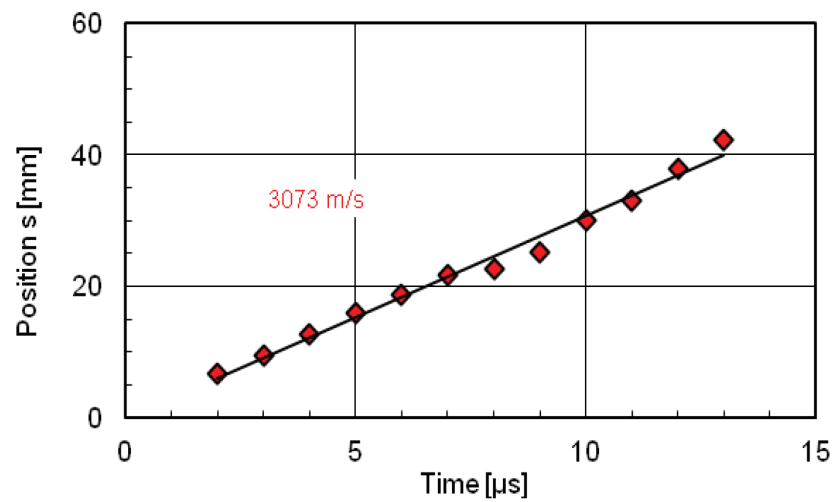
Figure 18. Position-time history of damage propagation in SL glass at 1115 m/s; Test #17751 .
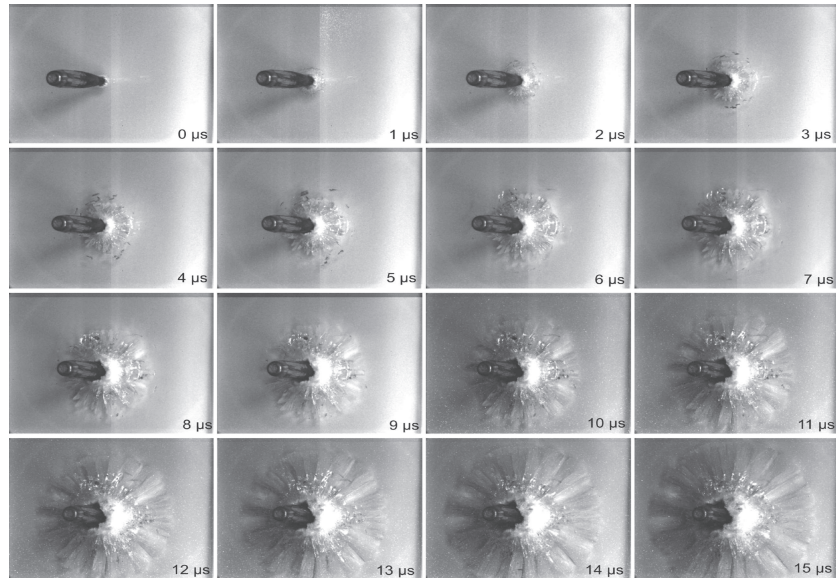
Figure 19. Selection of high-speed photographs from impact on fused silica glass
at 824 m/s; Test #17750 .
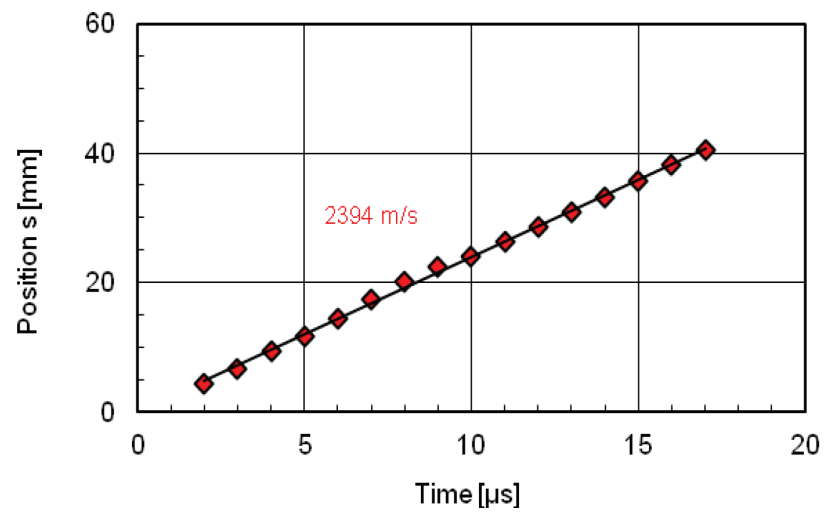
Figure 20. Position-time history of damage propagation in fused silica glass at
824 m/s; Test #17750 .

4.2.5   Fragmentation Analysis with Glass

The glass fragments from these experiments were collected and separated into size classes by a chain of sieves in the same way as the ceramic fragments. The mesh sizes used were 2 mm, 1 mm, 0.5 mm, 200 μm, 100 μm, 63 μm, and 25 μm. The total mass of each size fraction was determined. Figure 21 presents the values of the total fragment mass in the different size classes with the four different configurations. The corresponding cumulative mass plot is shown in figure 22.

A very high total mass of fragments of size > 2 mm can be recognized with the Borofloat glass. This result can be attributed to the size of the sample (150 mm x 150 mm), and therefore, the higher total mass (643 g) compared to the fused silica (290 g) and the SL glass samples (250 g). The highest fragment mass was found with fused silica in the size classes from 63 m to 1 mm. The cumulative mass plot also reflects the highest degree of fragmentation with fused silica in the tests with the steel cylinder. The least degree of fragmentation was observed with fused silica impacted by the AP projectile. In this case, the projectile also penetrated the aluminum backing nearly complete and a lower amount of energy was dissipated in the interaction with the glass.
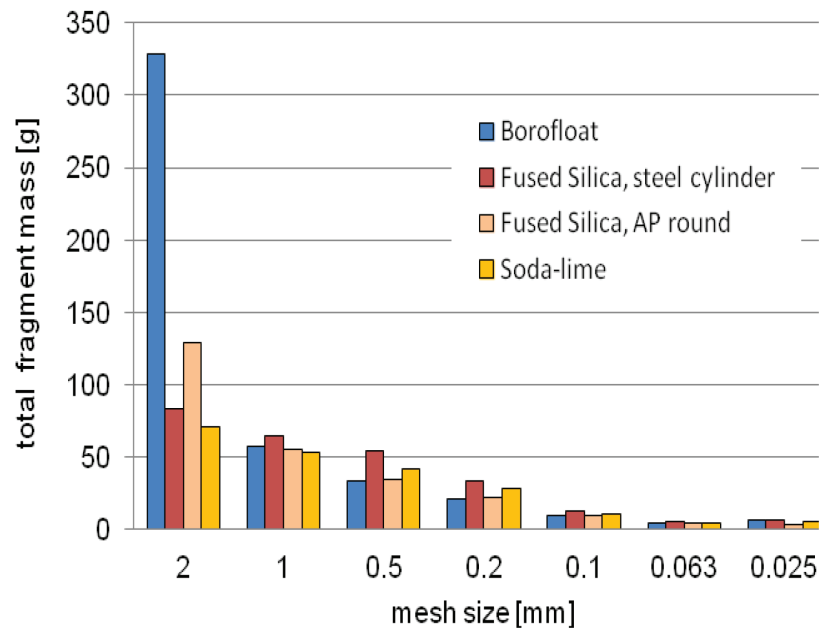
Figure 21. Fragment mass distribution from sieve analysis for tests with various glasses after Strassburger et al. (*7*).
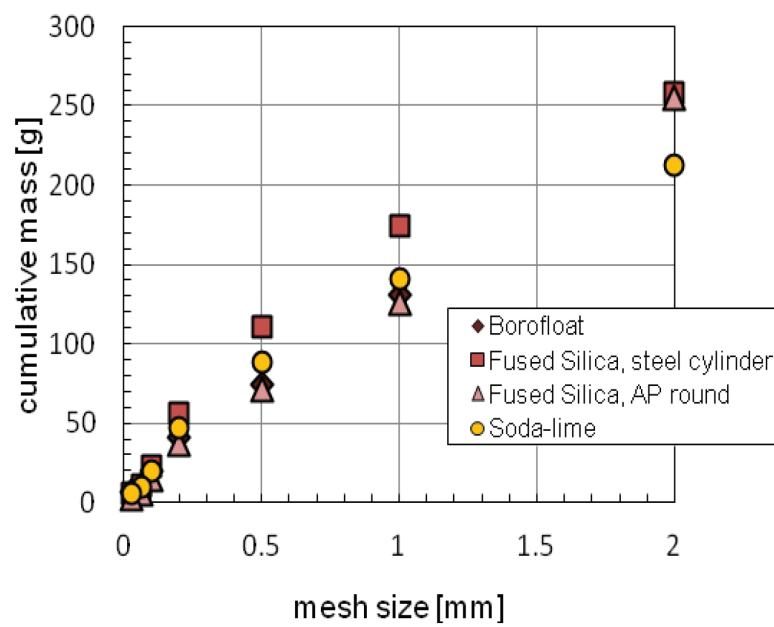
Figure 22. Cumulative mass plot for tests in various glasses.

4.2.6   Density Measurements with Glass Fragments

The compressibility of glass has been studied for several years and permanent densification up to 20% under high pressure has been reported (8, 30). Figure 23 shows the results of densification measurements with silica glass at 25 °C from three different researchers.
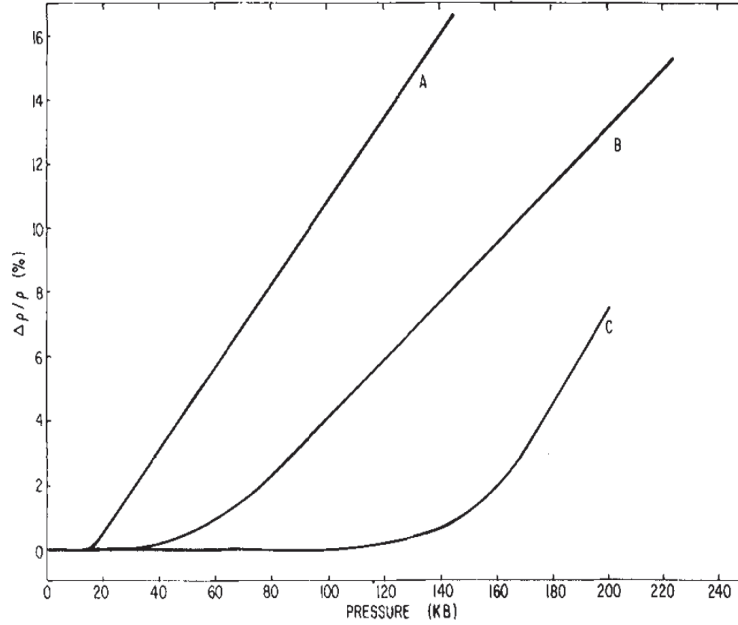
Figure 23. Densification of silica glass at 25 °C as a function of pressure from
Mackenzie (8); curve A from Roy and Cohen (9), curve B from
Christiansen et al. (10), and curve C from Bridgman (11).

The elastic shock induced at the impact surface between a projectile and a target is determined by the acoustic impedances of the projectile z_P and target material z_T and is given as follows (31):

$$P = \frac{z_P z_T}{z_P + z_T} V_P = \frac{\rho_P c_P \rho_T c_T}{\rho_P c_P + \rho_T c_T} V_P \tag{1}$$

where ρ_P, ρ_T is the density, and c_P and c_T are the longitudinal sound wave velocity of the projectile and target material, respectively.

If a steel projectile impacts a fused silica target, we have $\rho_P = 7.85$ g/cm^3, $\rho_T = 2.2$ g/cm^3, $c_P = 5100$ m/s, and $c_T = 6021$ m/s, then a shock pressure of ~11 GPa (~110 Kbar) is generated during impact of a steel projectile traveling at about $V_P = 1$ km/s onto a fused silica target. As per the data in figure 23 (curves A, B), a 4%–10% densification could possibly be expected.

26

Therefore, floatation-sink tests were performed with fused silica fragments of size 1–2 mm and 0.1–0.2 mm from impact tests #17749 (steel cylinder, 1107 m/s) and #17750 (7.62-mm AP projectile, 824 m/s). Aqueous sodium polytungstate (NaPW) was used as heavy liquid for the float-sink analysis. The density of the heavy liquid was varied within the range 2.19–2.4 g/ml. The density was measured by means of precision areometers. Table 9 summarizes the test data.

Table 9. Data from floatation-sink tests with fused silica fragments from impacted samples.

Test	Impact Test No.	Particle Size (mm)	Mass sample (g)	Volume NaPW-soln: (ml)	Addition dist. H_2O (ml)	Addition NaPW (ml)	Density NaPW-soln: (g/ml)	Observation:
1.	17749	1.000	4.99	50	15	x	2.40	silica swims
1.	17749	1.000	5.08	300	25	x	2.35	silica swims
1.	17749	1.000	5.26	325	15	x	2.29	silica swims
1.	17749	1.000	5.01	335	15	x	2.24	silica swims
1.	17749	1.000	5.09	350	15	x	2.19	silica swims
2.	17750	1.000	5.06	350	15	x	2.19	silica sinks
3.	17749	0.100	5.35	350	15	x	2.19	silica sinks
4.	17750	0.100	3.24	350	15	x	2.19	silica sinks
5.	17749	0.100	2.25	255	x	20	2.25	silica swims
6.	17750	0.100	2.43	255	x	20	2.25	silica swims

With the analyzed fragments, a densification could not be measured. On one hand, the collected fragments could not be allocated to their original position in the fused silica sample. Therefore, it was not possible to determine whether the analyzed fragments originated from the impact zone and had been subject to high pressure. On the other hand, due to the small diameter of the projectile, the duration of the pressure pulse could only have been short, because of the release waves from the edge of the projectile.

4.2.7 Micro/Nanocrystallinity in Glass

In discussions with Professor Adrian Wright from Reading University, UK, an expert in the structure of glass, he has said that the theory of glass structure is still evolving. The IRO is important, but poorly understood, and the current consensus is that there is chemical nanoheterogeneity, which may lead to nanoislands of crystallinity. Thus, the nature of IRO in glass is still evolving and controversial. Work by Saito et al. (*32*) using light scattering studies on silica glass concluded that medium (intermediate)-range order structures, microcrystallites, exist in silica glass. Using the polarization ratio, a measure of anisotropy, suggests that the depolarized scattering is only attributed to the density fluctuations with microscopic anisotropic scattering elements. Anisotropy of such scattering elements could be explained by the existence of microcrystallites.

4.2.8 Thermal Shock Behavior of Glasses

Bradt and Martens (*33*) in a recent article have reviewed the thermal shock resistance of various glasses, including borosilicate and SL glasses. They show that thermal stresses that develop during temperature changes are the primary cause of fracture initiation and failure. Using a simple formula for the generation of linear elastic thermal stresses σ_{ts},

$$\sigma_{ts} = \alpha E \Delta T \quad , \tag{2}$$

where, α is the coefficient of thermal expansion, E is Young's modulus, and ΔT is the local temperature differential. Rewriting equation 2 gives the temperature difference required to cause failure at a stress σ_f,

$$\Delta T = \frac{\sigma_f}{\alpha E} \quad , \tag{3}$$

hence, using this equation one can approximate the ΔT for glass fracture. Assuming the properties for a typical SL glass and a borosilicate glass (table 10), the ΔT for fracture can be approximated.

Other more complex equations can be used, but reflect very similar general trends. The general conclusion, therefore, is that the linear thermal expansion of glasses is a major factor in initiating crack formation and ultimate failure.

Table 10. ΔT required to fail SL and
borosilicate glasses.

	Soda lime	Borosilicate
σ_f	30 MPa	30 MPa
E	68 GPa	62 GPa
α	9 x $10^{-6o}C^{-1}$	3 x $10^{-6o}C^{-1}$
ΔT for α_f	55^oC	183^oC

4.2.9   Diamond Anvil Cell (DAC) Experiments to Study Density Changes in Glass with Pressure

The Army has a longstanding interest in understanding the properties of transparent protection materials, which form the basis of windshields, optics, and viewports. The silicate glass family of materials makes up the traditional choices for these applications. These materials fall into a much broader category of materials called amorphous glasses. The silicate glasses have several subcategories determined by the secondary component, namely, the Borofloat and SL varieties studied in this project. The major interest from the Army perspective in these glasses has to do with the differences in ballistic properties while being compositionally similar. The term "amorphous materials" when applied to glass is slightly misleading. These systems are thought to have several different arrangements from a rigid short-range silicon-oxygen bond length, to intermediate-range ring structures, and finally, to an overall amorphous packing of these smaller structures on the mesoscale. This structural hierarchy is still theoretical as the amorphous nature makes study and analysis difficult with existing techniques. Furthermore as silicate glasses have identical distances for the basic silicon-oxygen bond, it is apparent that the differences in the glass performance are due to the intermediate-range packing and ring structures. Understanding this difference is one of the goals of this research.

The current state of the art in understanding the IRO of silicate glasses is work involving complementary techniques of modeling and experiments. For the purposes of understanding how these materials change under ballistic impact, static data allow for comparisons to shock Hugoniot data. There has been previous work involving static pressure experiments on fused silica (*34, 35*), and also more recently on the similar germanium glass (*36*). The techniques employed in these studies were neutron diffraction and x-ray diffraction combined with structure factor analysis on the experimental side combined with MD simulations on the theoretical side. Even with these detailed studies, the mechanism for densification is still elusive, without adding the additional complexity of the effects of the secondary components.

The DAC provides a convenient method of studying glass samples under pressure. The experimental technique involves compression of the sample, the hydrostatic pressure medium, and the metal gasket between opposed diamond anvils. The hydrostatic pressure media use for these experiments is argon gas and the gaskets were composed of either rhenium or steel. The standard ruby fluorescence pressure scale was used (*37*). Samples were loaded in the DAC and then monitored for changes in sample area with pressure. This area was then converted to volume measurements using the method from previous work investigating the effect of helium on compression of SiO_2 glass (*12*). The pressure media is assumed to be hydrostatic in this technique. The equation used is reproduced below:

$$\frac{V}{V_0} = \frac{A}{A_0}\sqrt{A/A_0} \quad , \tag{4}$$

where V and V_0 refer to final and initial volumes, and A and A_0 refer to final and initial areas. The samples were initially prepared using a polishing technique to achieve the required thickness of < 20 microns. The samples were then extracted yielding a glass chip that was approximately 30–50 microns in diameter. This was so that the sample could be loaded in a gasket with 100-micron hole. It was noted that the irregular surface of the chips made interpretation of the edges for the area calculation difficult. In addition, it was thought that the corners could provide stress points in the sample and introduce unintended strain into the measurement. To correct this issue, the samples were machined using a FIB technique to achieve a cylinder 40 microns in diameter and 20 microns thick. The results for fused silica are shown in figure 24.

This change in volume can be converted into a change in density and plotted upon previous measurements for fused silica (*13*). Figure 25 provides a compilation of previous studies on the density changes with pressure for previous methods. The diamonds plots represent densified glass; glass that has been pressurized to 10 GPa and then released to ambient pressure.
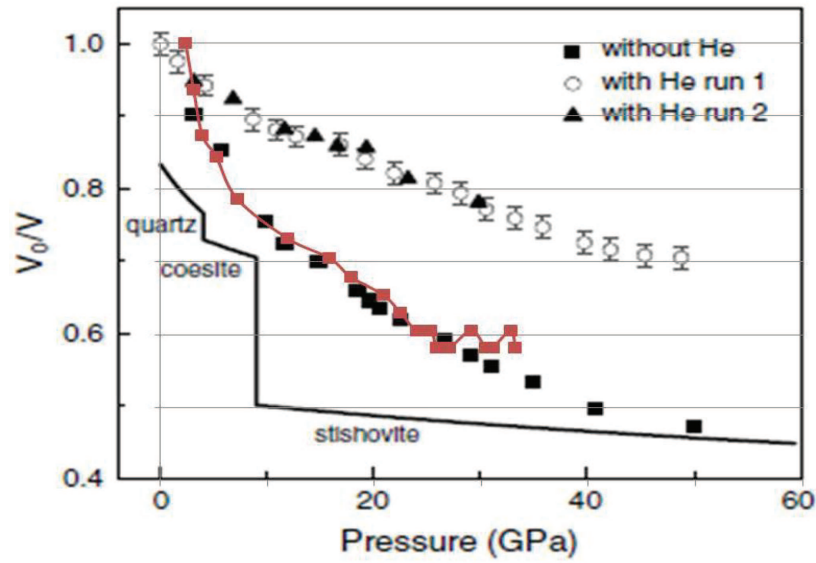
Figure 24. DAC results for fused silica compared to previous DAC results published in (*12*) (our results are in red). Phase lines for the different quartz structures are shown. At approximately 27 GPa, the sample is thought to be bridged by the diamonds. This accounts for the deviation seen at 27–30 GPa.
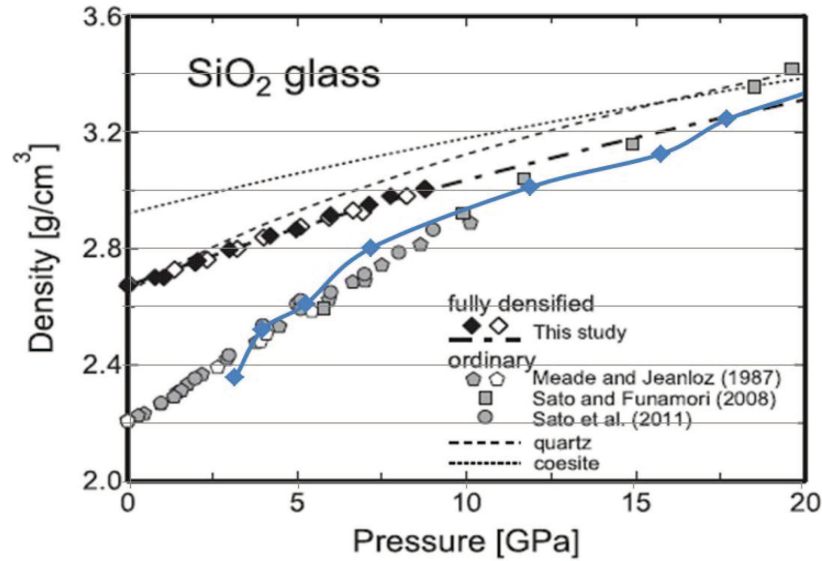
Figure 25. Plot of density changes with pressure for fused silica. Original figure from Wakabayashi et al. (*13*).

31

Shown in figure 26 is an example of the comparison between the sample at 4 and 33 GPa for fused silica. The gray circle on the 4 GPa side corresponds to the sample diameter at 33 GPa and is shown for comparison purposes. As the pressure is increased, the sample hole closes due to the plastic flow of the gasket material.

In addition to the DAC experiments, neutron diffraction was investigated on the nanoscale-ordered materials diffractometer (NOMAD) beamline at the spallation neutron source (SNS) at Oak Ridge National Laboratory. This technique results in a total scattering cross section, which is integrated over the entire sample. The scattering can be converted into a momentum transfer and provide a "first sharp diffraction peak" (FSDP), seen in figure 27. The simplest way to interpret Q is to realize that the lower the Q the larger the interaction. If one thinks about the network structure of glasses, the scattering can be broken up into several regions, namely, the SRO, IRO, and long-range order. Glasses have rigid SRO in the form of a silicon dioxide tetrahedron and disorder with regard to the random nature of the long-range order. IRO can have order in the form of rings, cages, and chains. In order to extract the interaction distances, it is important to use a high energy source; due to the nature of the Fourier transform, the higher the energy the better the resolution on the low Q region.
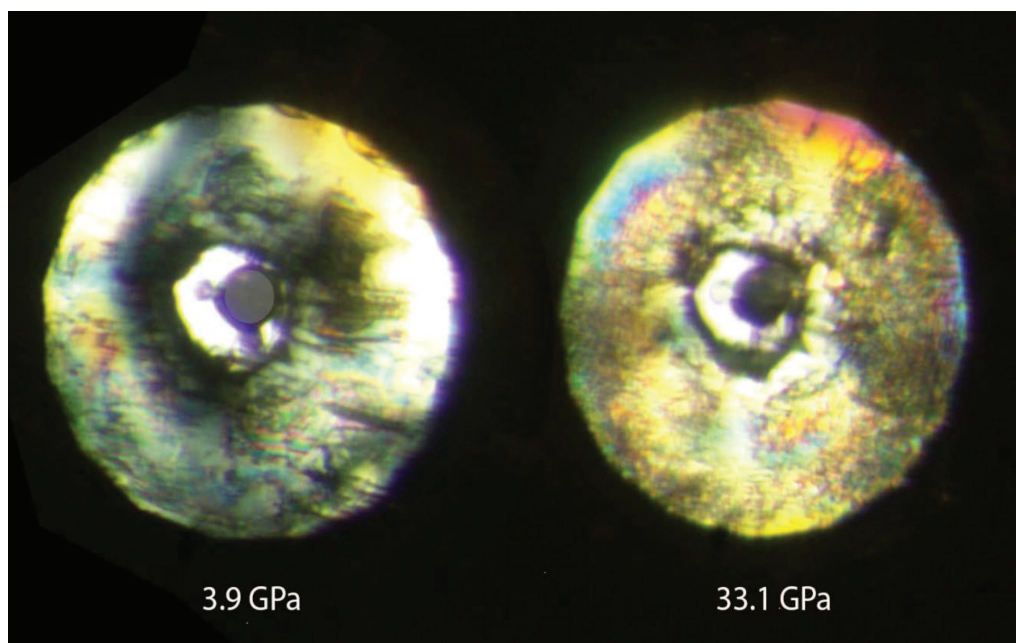
Figure 26. Comparison of sample upon compression in the DAC. The 3.9-GPa sample has a gray sphere to indicate the area of the sample at 33.1 GPa to assist the eye in comparison.
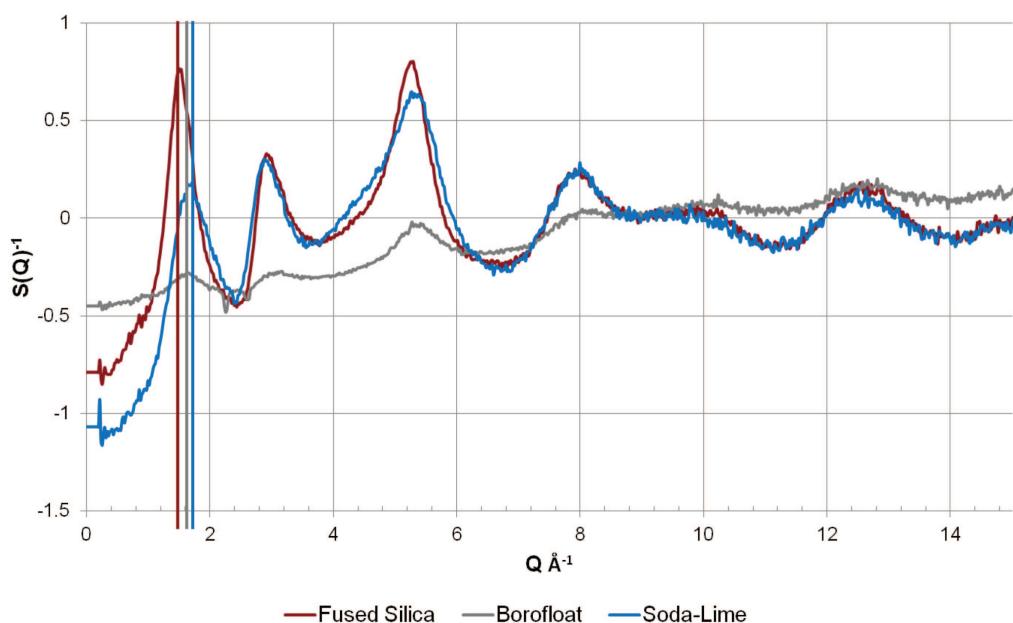
Figure 27. Neutron diffraction spectra of fused silica, Borofloat, and SL glasses. Intensities are not corrected for the boron neutron absorption cross section. The location of the first sharp diffraction peak is indicated; shifts to higher Q correspond to decreases in intermolecular interaction distances.

To further study the effects of composition on pressure and ballistic response, samples of glass were prepared with known concentrations of secondary molecules. These samples were subjected to initial study with the laser Raman system to discern if there were noticeable differences in the spectra shown in figure 28. The spectra were obtained using a 532-nm diode laser (average power 300 mW) and a custom Raman spectrometer. Preliminary analysis of the results seems to indicate a change in the 300–400 wavenumber regions with decreasing intensity as the composition changes with each sample. The spectra were normalized to a higher wavenumber region ($< 2500 \text{ cm}^{-1}$). The samples for use in the DAC are being prepared using the FIB so similar density pressure analysis can be attempted.
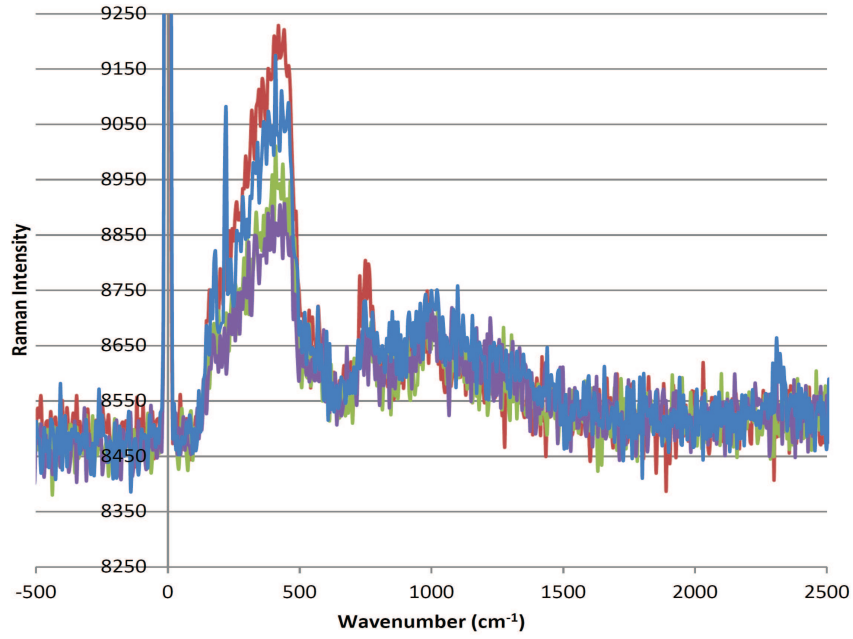
Figure 28. Raman comparison of four prepared glass samples by Dr. Parimal Patel. Peak at zero is the laser line, partially blocked by a notch filter that extends to approximately 150 cm^{-1}.

4.2.10 Nanoindentation Studies of Fused Silica

Nanoindentation experiments were conducted at ARL on fused silica specimens using an MTS Nanoindenter XP operated in continuous stiffness measurement (CSM) mode. A spherical indenter with a radius of 3 μm was used to indent to depths approaching 2 μm at a constant strain rate of 0.05/s. The hardness values, H, were calculated from the maximum loads, P_{max}, and the contact area, A, at the maximum indentation depth where $H = \frac{P_{\max}}{A}$. The elastic modulus values were calculated using the Oliver and Pharr method (*38*) from the measured unloading stiffness, S (which is equivalent to the slope of the initial unloading curve), as follows:

$$S = \frac{2}{\sqrt{\pi}} E_{eff} \sqrt{A} \tag{5}$$

where E_{eff} is a function of the Poisson's ratio and elastic modulus for the indenter (ν_i, E_i) and material of interest (ν, E) defined as

34

$$\frac{1}{E}_{eff} = \frac{1 - \nu^2}{E} + \frac{1 - \nu_i^2}{E_i} \tag{6}$$

Following the indentation experiments, the residual indents were examined with a NanoSEM 600 SEM operated in low-vacuum mode (which is used to accommodate non-conductive specimens.)

Figure 29 shows the typical load-displacement curves for maximum displacements ranging from 500 to 2000 nm. Figure 30a plots the measured hardness as a function of indentation depth and indicates there is some indentation size effect over the range considered. The standard deviation is largest for the smallest indentation depths (500 nm). The elastic moduli decrease with increasing maximum indentation depth (figure 30b); however, the error in measurement does not follow a trend with depth. The SEM examination gives insight into the indentation size effect. We are unable to resolve a residual impression for the specimens indented to a depth limit of 500 nm, which indicates the response is mostly elastic at small depths. Figures 31–33 show SEM micrographs for specimens indented to depths of 1000, 1500, and 2000 nm, respectively. There is a noticeable residual indent in figure 31; however, there is evidence of fracture. At greater indentation depths, radial cracks (figures 32a and 33) and classic cone cracks (figure 32b) are visible. Further investigation is required, but the lower hardness and modulus values measured at greater indentation depths could result from indentation cracks. In some brittle material systems, "pop-ins" or discrete jumps in displacement during indentation are found in the load-displacement curves. However, no pop-ins are observed in this series of nanoindentation tests.
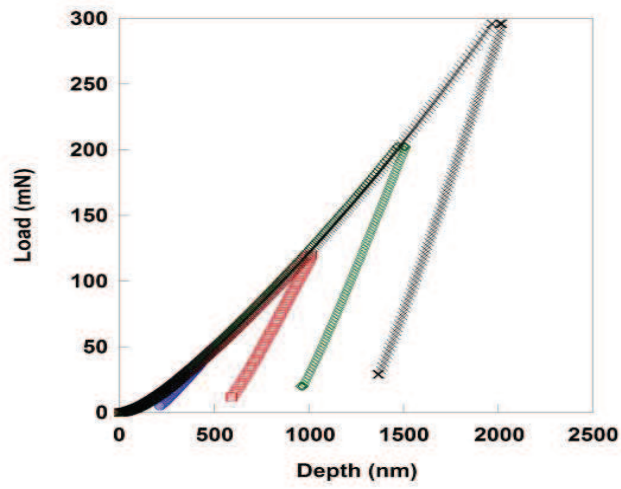
Figure 29. Load vs. displacement in fused silica.

(a)

(b)
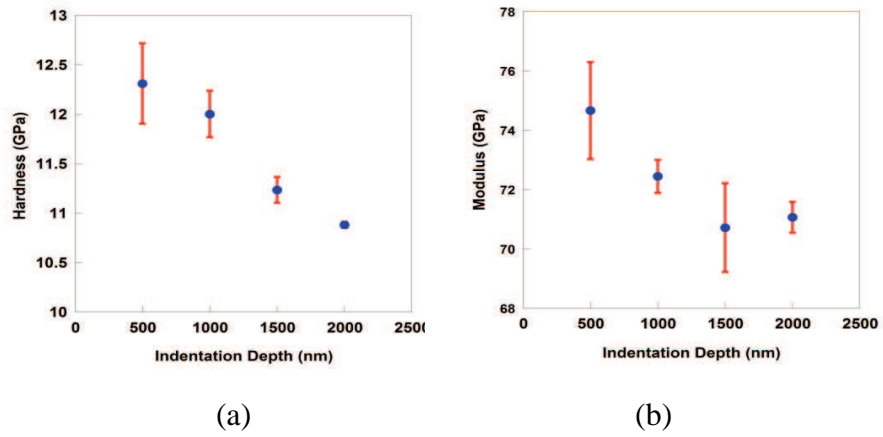
Figure 30. (a) Hardness and (b) modulus variations in fused silica.

36
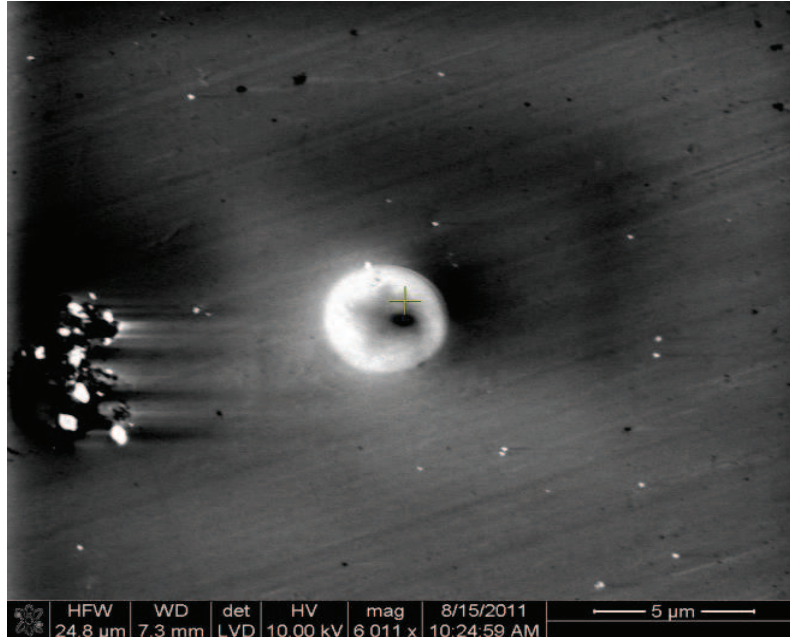
Figure 31. SEM micrographs of fused silica indented to 1000 nm.

(a)   (b)
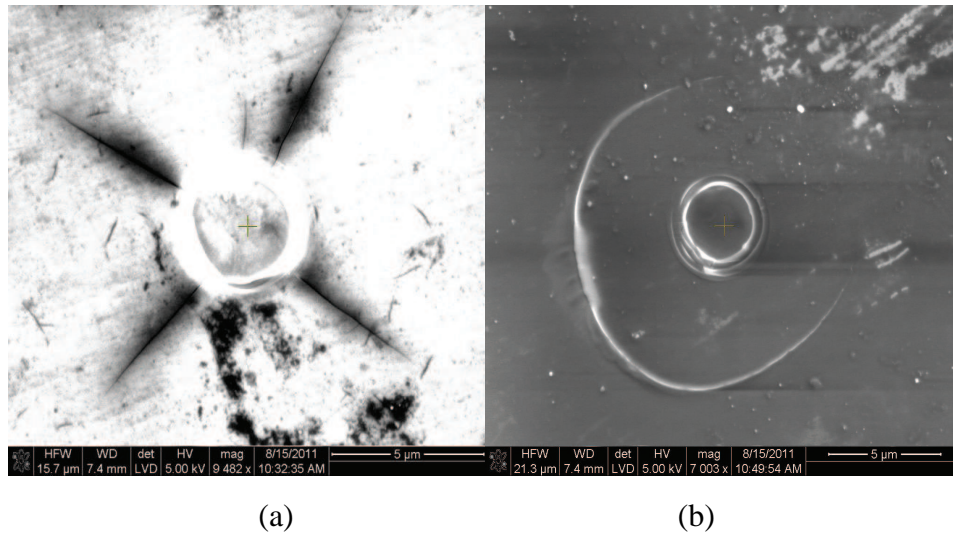
Figure 32. SEM micrographs of fused silica indented to 1500 nm (a) radial cracks
            and (b) cone cracks.
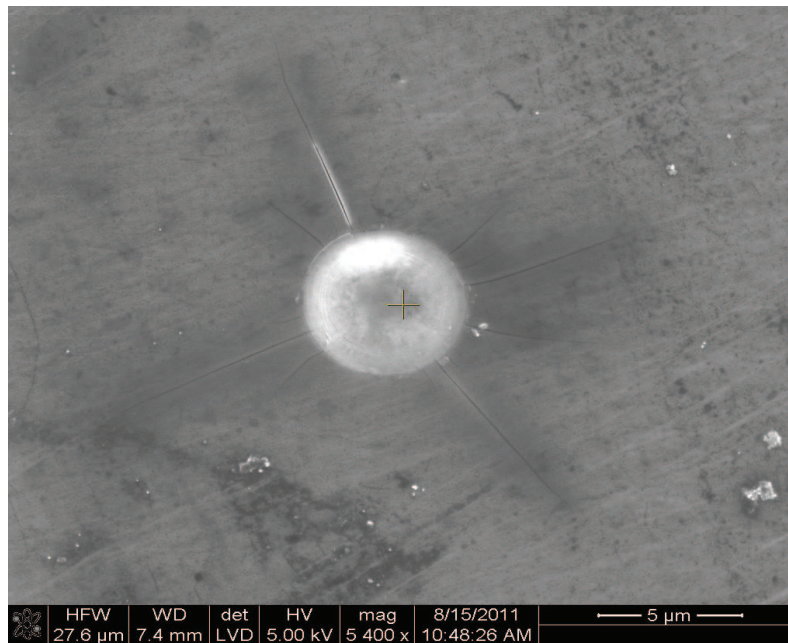
Figure 33. SEM micrographs of fused silica indented to 2000 nm.

5. Pairwise Functional-free Silica Potential From First-principles Molecular Dynamics Simulation

We have developed a new short-range pairwise numerical potential for silica, as described in Izvekov and Rice (*14*). Here we present the key features of the model. The potential is derived from a single AIMD simulation of molten silica using the force-matching (FM) method, with the forces being represented numerically by piecewise functions (splines) (*39*). The AIMD simulation is performed using the Born-Oppenheimer method with GGA (BLYP) and XC functional. The new effective potential shown in figure 34 includes a soft repulsive shoulder to describe the interactions of oxygen ions. The new potential, despite being short-ranged and derived from single-phase data, exhibits a good transferability to silica crystalline polymorphs and amorphous silica. The importance of the $O - O$ soft repulsive shoulder interaction on glass densification under cold and shock compressions is assessed from MD simulations of silica glass under room and shock Hugoniot conditions, respectively, and shown in figure 35. Results from these simulations indicate that the appearance of oxygen complexes (primarily pairs) occurs at 8–10 GPa, and under cold compression conditions becomes notable at 40 GPa, essentially coinciding with the transition to a Si sixfold coordination state. An analysis of changes in system structure in compressed and shocked states reveals that the O ions interacting through the soft repulsive shoulder potential in denser states of silica glass may create a mechanical multi-stability under elevated pressures, and thus contribute to the observed anomalous densification.

At pressures $P < 8$–10 GPa, the densification by the FM model occurs predominantly due to structure deformation and topological reorganization rather than a weakening of the $O - O$ repulsion due to the soft repulsive shoulder of the FM potential. The observed disagreement of the FM cold and Hugoniot density-pressure curves at low ($P = 0$–10 GPa) pressures with the experiment data (figure 35) can be explained by the deficiency of the FM model, which is pairwise and central, regarding angle-bending terms. The extension of the pairwise FM model with angle-bending forces, which are three-body forces, is necessary to improve performance of the FM model at low pressures in which densification is driven by mostly structural and topological changes. This work is in progress.
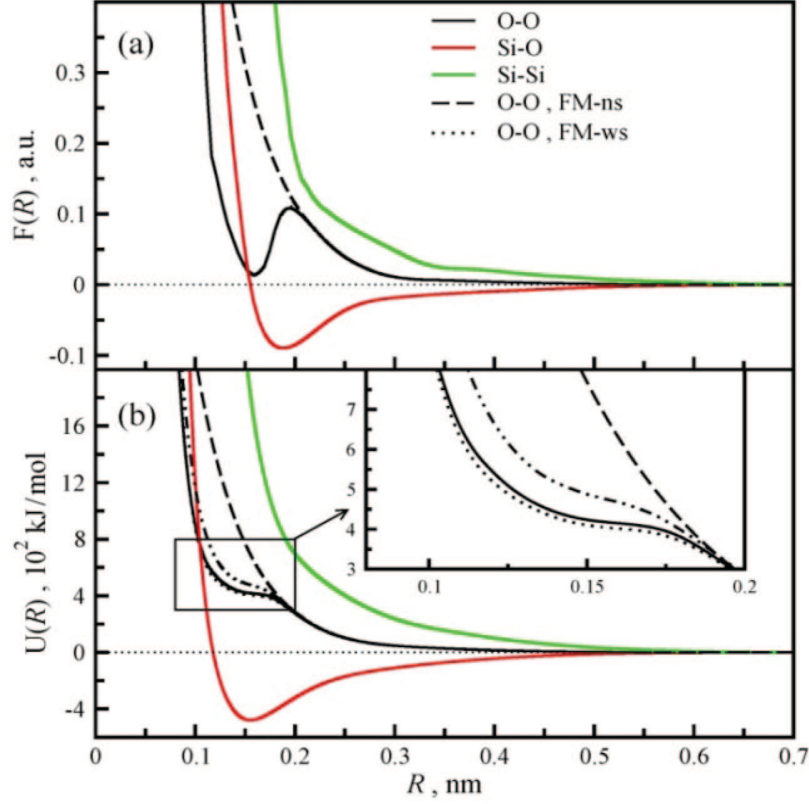
Figure 34. Effective atom-atom forces [panel (a)] and corresponding potentials [panel (b)] in liquid SiO_2 generated through the FM method as functions of interatomic separation: $O - O$ (black), $Si - O$ (red), and $Si - Si$ (green). The dashed line corresponds to the model without the soft repulsive shoulder (FM-ns model). In panel (b), the dotted line corresponds to the FM model with a weaker repulsive shoulder (FM-ws model) and the dot-dot-dashed lines indicate the variation of the $O - O$ repulsion in the FM procedure with a length of ab initio reference trajectories as discussed in (*14*).

40
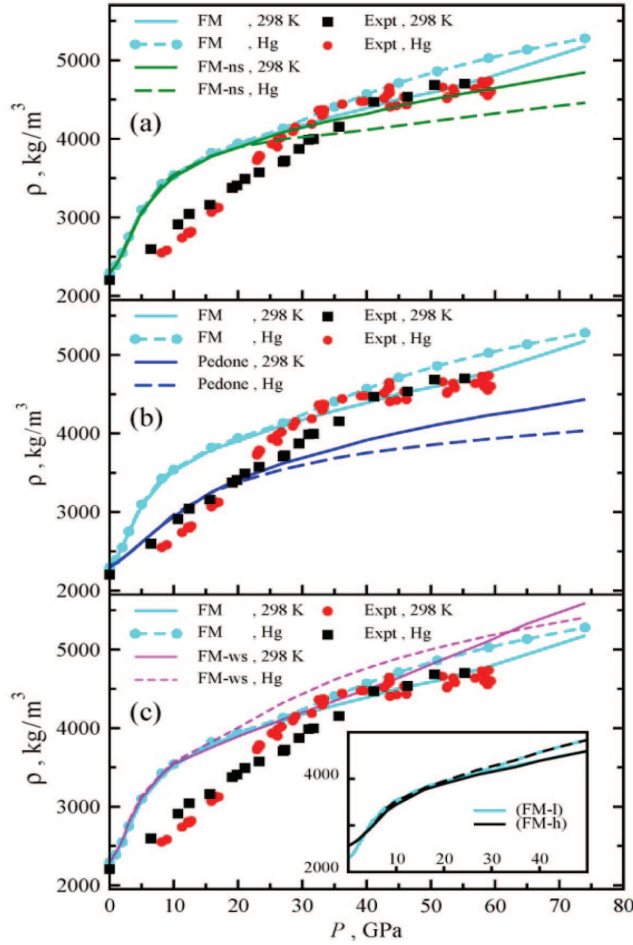
Figure 35. Density vs. pressure at $T = 298$ K (solid lines) and along the Hugoniot locus (dashed lines) from simulations of glass sample structure using the FM (cyan), FM-ns (green) [panel (a)], Pedone (blue) [panel (b)], and FM-ws (magenta) [panel (c)] models. Experimental EOS obtained by cold compression (black squares) and by shock compression (red circles) are from (*15*) and (*16*), respectively. Insert to panel (c) compares the 298 K (solid) and Hugoniot (dashed) EOS from simulations of the ambient density (FM-l) and densified (FM-h) glass samples using the FM models.

41

5.1   Molecular Dynamics Modeling of Glass Nanoindentation

MD methods have been used to study nanoindentation for a number of material systems, i.e., metals (*40*), ceramics (*41*), glasses (*42*), and energetic materials (*43*). Length scales for MD simulations can be made comparable to those in the experiments of Nomura et al. (*42*), although the time scales and strain rates differ significantly. The advantage of MD simulations over nanoindentation experiments is the capability to provide atomistic detail of numerous properties, including stress distribution and structural information.

We have previously reported on MD simulations of nanoindentation performed on a large-scale fused silica system (*44*). Here we extend the analysis, including a calculation of the hardness, and compare to experimental results. As described in Gazonas et al. (*44*), all the simulations were performed using the Large-scale Atomic/Molecular Massively Parallel Simulator (LAMMPS) (*45*), with the pairwise potential recently developed using FM techniques described in section 5. The simulation cell is 29.9 x 29.9 x 17.8 nm, containing 1,160,952 atoms (386,984 $a - SiO_2$ molecules). Once the system is equilibrated, following the annealing schedule described in Pedone et al. (*46*), a spherical indenter with a radius of 9 nm is introduced in the z-direction. The indenter interacts with atoms in the simulation cell via a force of magnitude,

$$F = -K(r - R)^2 \quad , \tag{7}$$

where K is a force constant, R is the radius of the indenter, and r is the distance from the atom to the center of the indenter. Periodic boundary conditions are implemented in the x- and y-directions; the indented surface remains free, and approximately 33,000 atoms on the opposite surface are held fixed to ensure that the system remains stationary during indentation. The simulation is performed in the microcanonical ensemble (NVE), with a timestep of 2.0 fs. It has recently been determined that this timestep is too large for simulations using the FM potential. The dynamics of the system are not properly captured when using a large integration timestep, and the differences between our results and those from experiment are due partly to this large timestep, as is discussed.

Figure 36 shows the complete loading and unloading curve, as well as the cross sections of the corresponding atomic configurations at the maximum load (figure 36b), and after complete unloading (figure 36c). The hardness, H, is defined as,
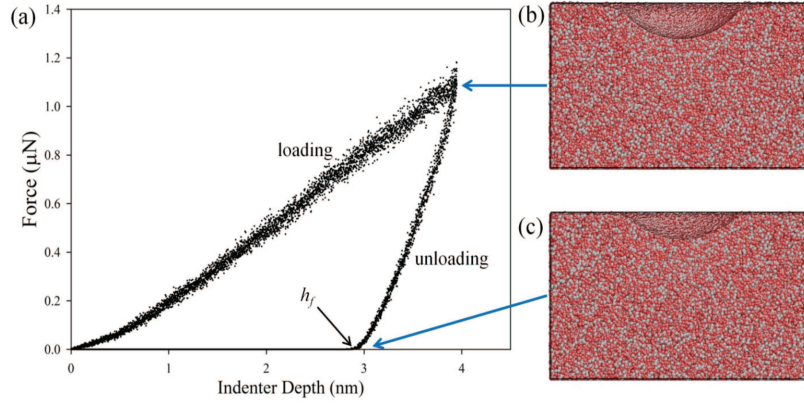
Figure 36. (a) Force vs. indenter depth for a complete loading and unloading cycle. Atomic configuration (b) at the point of maximum loading, and (c) after complete unloading.

$$H = \frac{P_{max}}{A} \quad , \tag{8}$$

where P_{max} is the maximum applied load and A is the contact area. The maximum load is determined from the loading curve in figure 36a by fitting the latter portion of the data to a line and determining the load corresponding to the maximum depth. The value we calculate is 1.10 μN. To calculate the contact area, we use a method similar to that described in Chen and Ke (*47*). First, the atoms in contact with the indenter are identified by calculating the distance between each atom and the center of the indenting sphere. Those atoms appear in red in figure 37, along with their projection onto the xy-plane. The area of a circle in the xy-plane that contains all the projections is defined as the contact area. We calculate an area of 14900 Å^3, resulting in a hardness value of 7.38 GPa. This differs from the value we previously reported (*44*) due to the more refined method of calculating the contact area. Furthermore, it is not in agreement with the experimental value of 10 GPa reported in Miyake et al. (*48*), nor with the depth-dependent hardness values determined from our own nanoindentation experiments (see figure 30a). As mentioned above, the disagreement could be attributable to the too large timestep, but the effect of sample size should also be explored to ensure the size of the sample is not adversely affecting the hardness calculation.
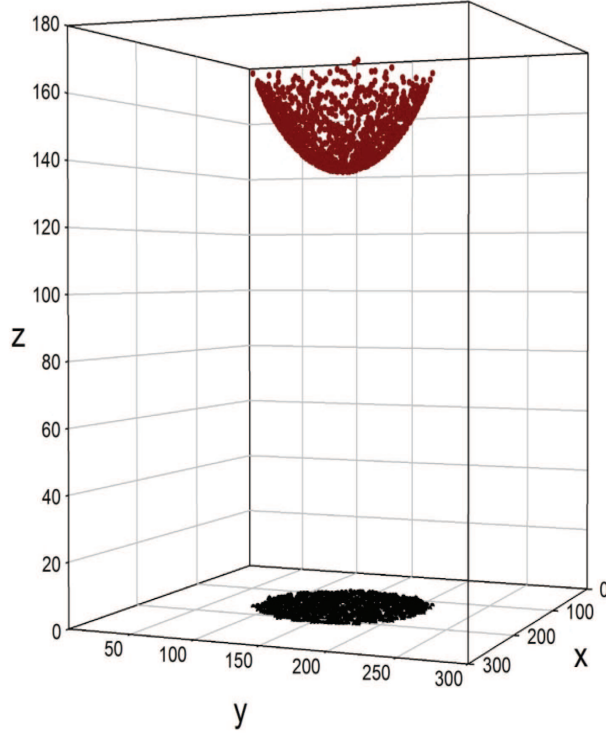
Figure 37. The atoms that are in contact with the indenter are shown in red, and
their projection onto the xy-plane is shown in black.

Nanoindentation experiments have shown that the unloading curve can be approximated by the power law relation (*38*),

$$P = \alpha(h - h_f)^m \quad , \tag{9}$$

where α and m are fitting constants, and the final depth, h_f, is the permanent depth of penetration after the indenter is fully unloaded (see figure 36). We have fit the unloading curve in figure 36a to this equation, with h_f included as a fitting parameter, resulting in $\alpha = 0.9720\ \mu N/nm^m$, $m = 1.445$, and $h_f = 2.889$ nm. The value of h_f is in agreement with our data, and the value of m for a spherical indenter is expected to be 1.5 (*49*), close to the value we obtain.

The value of α differs significantly from the experimental value of $50.0\ \mu N/nm^m$ for fused silica (*38*), although that was obtained with a Berkovich indenter. The discrepancy in α is not

44

surprising as the loading depths reached in nanoindentation experiments are much larger than in our simulation, and the strain rates are significantly lower than can be achieved in MD simulations. However the shape of the curve, indicated by the value of m, is consistent with experimental values, despite the timestep being too large. In addition to repeating the above simulation with a smaller timestep, we plan to perform nanoindentation on larger systems to study size effects on the mechanical response of fused silica. We will also perform nanoindentation simulations using a flat punch indenter (for which $m = 1$ in equation 9) to directly compare with the dimensional analysis results presented in section 6. Finally, the force match potential will be extended to include three-body forces as well as additional atom types in order to model borosilicate glasses.

6. Dimensional Analysis of Hertzian Cone Crack Development in Brittle Elastic Solids

In this section, we outline the methodology for the derivation of similarity relationships for elastic solids exhibiting stable crack growth induced by rigid indenters; as will be shown in a subsequent section, such relationships are invaluable for verification of computational models that involve crack propagation. The application of dimensional analysis to the development of stable cone cracks appears to have been first addressed by Roesler (*17*) and Benbow (*18*), and later more fully analyzed by Barenblatt (*50*). The universal dimensionless relationship:

$$D = \left(\frac{P}{K}\right)^{\frac{2}{3}} \quad , \tag{10}$$

relates the width D of the base of a cone crack induced by a flat punch (cylindrical indenter) to the load P, and cohesive modulus K of the medium (figure 38). Cone crack development in glass (figure 39) confirms the universal scaling law (equation 10) illustrated in the log-log plot of figure 40. In addition to the relevant physical parameter illustrated in figure 38, Poisson's ratio, ν, and the modulus of cohesion K play an important role in describing the mechanics of the indentation problem. According to similarity methods described by Sedov (*51*) and others, since there are five relevant physical variables, and three fundamental dimensions of M, L, and T, this results in two possible dimensionless products, which can be formed from the physical variables.
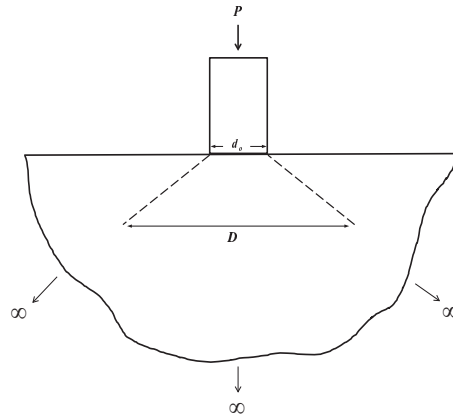
Figure 38. Dimensional analysis for the axisymmetric Hertzian cone crack
problem .
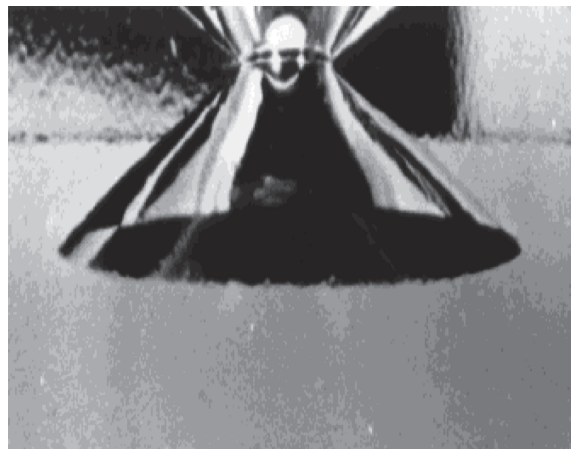
Figure 39. Hertzian cone crack in SL glass induced by a flat punch (cylindrical
indenter) after (*17*) .
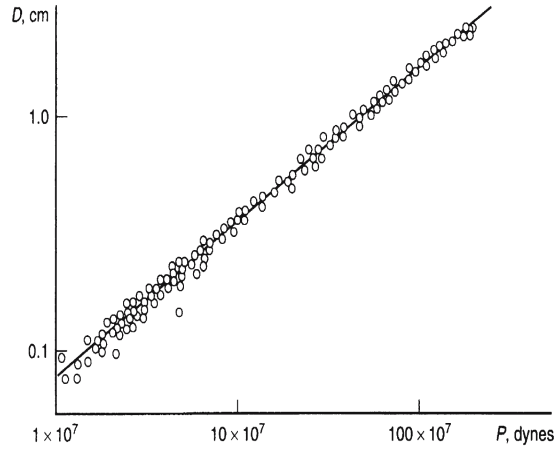
Figure 40. Hertzian cone crack data for fused silica, and experimental confirmation of scaling law from Benbow (*18*).

The two dimensionless groups can be derived for this problem by first writing the relevant physical parameters in the following multiplicative form:

$$(D)^{k_1}(d_0)^{k_2}(P)^{k_3}(K)^{k_4}(\nu)^{k_5} = 1 \quad , \tag{11}$$

and the expressing equation 11 in terms of the fundamental dimensions:

$$(L)^{k_1}(L)^{k_2}(MLT^{-2})^{k_3}(ML^{-1/2}T^{-2})^{k_4}(1)^{k_5} = 1 \quad . \tag{12}$$

The fundamental dimension terms in equation 12 can be factored as follows:

$$(M)^{k_3+k_4}(L)^{k_1+k_2+k_3-k_4/2}(T)^{-2k_3-2k_4} = 1 \quad , \tag{13}$$

resulting in the following system of equations:

47

$$k_3 + k_4 = 0 \quad ,$$
$$k_1 + k_2 + k_3 - k_4/2 = 0 \quad ,$$
$$-2k_3 - 2k_4 = 0 \quad , \tag{14}$$

that are solvable using the constants that appear in table 11.

Table 11. Constants appearing in
dimensional analysis .

	k_1	k_2	k_3	k_4	k_5
π_1	1	0	$-2/3$	$2/3$	1
π_2	0	1	$-2/3$	$2/3$	1

The dimensionless groups, also known as π-groups from the Buckingham π theorem (*52*) can be written as

$$\pi_1 = D P^{-2/3} K^{2/3} \nu \quad ,$$
$$\pi_2 = d_0 P^{-2/3} K^{2/3} \nu \quad . \tag{15}$$

Since the π-groups in equation 15 are dimensionless, they can be equated and solved for the width D of the base of the cone crack,

$$D = \left(\frac{P}{K}\right)^{2/3} \nu f(d_0 (\frac{K}{P})^{2/3}, \nu) \quad . \tag{16}$$

Thus, a log-log plot of D versus P, for $D >> d_0$, will have a slope of $2/3$, as it appears that the contribution from the third function in equation 16 is negligible (see figure 40). The fracture scaling law can also be used to validate finite element, peridynamic, material point, MD, and other computational methods currently in use for simulating fracture resulting from indentation experiments.

For fractures that develop under two-dimensional (2-D) states of stress such as the problem of the symmetric wedging of a thick plate (*19*), the wedging force can be approximated by two equal

and opposite concentrated tractions P per unit length of plate thickness as illustrated in figure 41. Using the dimensional analysis methods outlined earlier in this section, a dimensionless relation can be derived, for 2-D stress and deformation fields, which only depends on crack length l, load P, and cohesive modulus K (*19*):

$$ l = \left(\frac{P}{K} \right)^2 \quad . \tag{17} $$
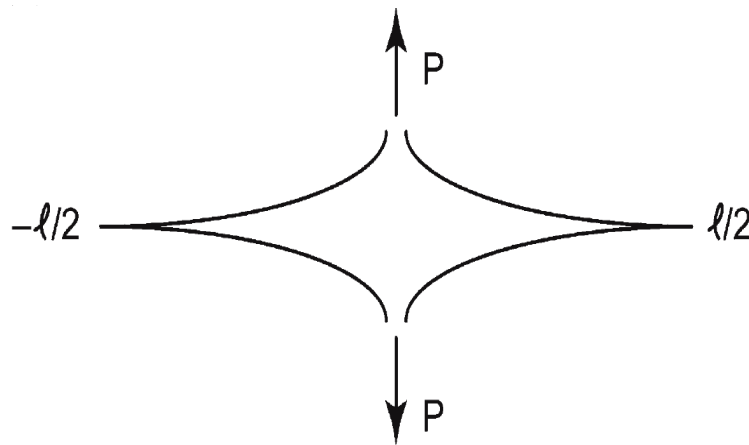
Figure 41. Idealized 2-D problem of wedge-induced crack propagation in a thick
plate after Barenblatt (*19*).

This result is used to validate our peridynamic code simulations of fracture in section 10.1.

7. The Mechanics of Indentation

In this section, we outline the exact solution to the axisymmetric indentation problem into an elastic halfspace, otherwise known as the Boussinesq problem, that is relevant to the dimensional analysis described in section 6. The exact elastic solutions provide a means to quantitatively validate computational simulations, prior to the development of permanent densification and fracture of the glasses under consideration in this research. Boussinesq (*53*) and Love (*54*) were among the first to consider such a problem, but Sneddon solved the problem for the flat-ended punch (*55, 56*) in cylindrical polar coordinates using Hankel transforms that resulted in the

49

solution of dual integral equations (*57*). The solutions to the field equations are listed below as they appear in Sneddon's (*25*) textbook,

$$u_r = -\frac{2\mu\epsilon\left(J_0^1 - \frac{(\lambda+\mu)}{\mu}\zeta J_1^1\right)}{\pi(\lambda+2\mu)} \quad ,$$

$$u_z = \frac{2\epsilon\left(\frac{(\lambda+\mu)}{\lambda+2\mu}\zeta J_1^0 + J_0^0\right)}{\pi} \quad ,$$

$$\sigma_z = -\frac{4\mu\epsilon\left(\zeta J_2^0 + J_1^0\right)(\lambda+\mu)}{\pi a(\lambda+2\mu)} \quad ,$$

$$\tau_{rz} = -\frac{4\zeta J_2^1 \mu\epsilon(\lambda+\mu)}{\pi a(\lambda+2\mu)} \quad ,$$

$$\sigma_\theta = -\frac{4\zeta J_1^0 \lambda\mu\epsilon}{\pi a(\lambda+2\mu)} - \frac{4\mu^2\epsilon\left(J_0^1 - \frac{(\lambda+\mu)}{\mu}\zeta J_1^1\right)}{\pi a\rho(\lambda+2\mu)} \quad ,$$

$$\sigma_r + \sigma_\theta = -\frac{4\mu\epsilon\left(J_1^0(2\lambda+\mu) - \zeta J_2^0(\lambda+\mu)\right)}{\pi a(\lambda+2\mu)} \quad . \tag{18}$$

In these equations, the dimensionless radial coordinate $\rho = r/a$ is the physical radial distance r normalized by the indenter radius a, and the dimensionless depth coordinate $\zeta = z/a$ is the physical depth z normalized by the indenter radius a. ϵ is the indentation depth, and the Lamé parameters are given by λ and μ. The radial stress σ_r is not given in Sneddon's text but can be derived readily by subtraction of σ_θ from $\sigma_r + \sigma_\theta$ from equations 18 resulting in

$$\sigma_r = \frac{4\mu\epsilon(J_0^1\mu - (\lambda+\mu)(\rho(J_1^0 - \zeta J_2^0) + \zeta J_1^1))}{\pi a\rho(\lambda+2\mu)} \quad , \tag{19}$$

where Bessel functions J_n^m are defined as

$$J_n^m = \int_0^\infty p^{n-1}e^{-\zeta p}\sin(p)J_m(p\rho)\,dp \quad , \tag{20}$$

or as the imaginary part of the integral

50

$$J_n^m = \int_0^\infty p^{n-1} e^{-p(\zeta - i)} J_m(p\rho)\, dp \quad . \tag{21}$$

We derive an explicit representation for equation 21,

$$J_n^m = \Im\left(2^{-m}\rho^m(\zeta - i)^{-m-n}\Gamma(m+n)\, _2\tilde{F}_1\left(\frac{m+n}{2}, \frac{1}{2}(m+n+1); m+1; -\frac{\rho^2}{(\zeta - i)^2}\right)\right), \tag{22}$$

where $(\rho, \zeta) > 0, \Re(m+n) > 0$, $\Im$ is the imaginary part of the term in brackets, $m, n \in \mathbb{Z}$, and $_2\tilde{F}_1$ is the regularized hypergeometric function $_2F_1(a,b;c;z)/\Gamma(c)$.

All solutions listed in equation 18 are exact and expressible in closed-form except for u_z, which requires the evaluation of J_0^0. The solution for u_z, which involves J_0^0 is written in terms of $\Gamma(m+n) = (m+n-1)!$, which is an undefined quantity for $m = 0, n = 0$ as this violates the condition $\Re(m+n) > 0$ in equation 22 and probably explains why the full plane solution for u_z is not provided in any publications we are aware of (25), (55), (56), (58)*. Sneddon's solutions can be rewritten more succinctly using the substitution, $\lambda = \frac{2\mu\nu}{1-2\nu}$, and by normalizing the stress components by the mean pressure $p_m = \frac{8\mu\epsilon(\lambda+\mu)}{\pi a(\lambda+2\mu)}$, and the displacement components by the indentation depth ϵ, resulting in

$$\frac{u_r}{\epsilon} = -\frac{(-\zeta J_1^1 + (1-2\nu)J_0^1)}{\pi(1-\nu)} \quad ,$$

$$\frac{u_z}{\epsilon} = \frac{(2(1-\nu)J_0^0 + \zeta J_1^0)}{\pi(1-\nu)} \quad ,$$

$$\frac{\tau_{rz}}{p_m} = -\frac{\zeta J_2^1}{2} \quad ,$$

$$\frac{\sigma_z}{p_m} = -\frac{1}{2}\left(\zeta J_2^0 + J_1^0\right) \quad ,$$

$$\frac{\sigma_\theta}{p_m} = -\frac{1}{2\rho}[\zeta(2\nu\rho J_1^0 - J_1^1) + (1-2\nu)J_0^1] \quad ,$$

$$\frac{\sigma_r}{p_m} = -\frac{1}{2\rho}[J_1^0\rho - \zeta(\rho J_2^0 - J_1^1) - (1-2\nu)J_0^1] \quad . \tag{23}$$

Note that the analytical solutions in equation 23 for elastic displacements and stresses in the

---

*The first author became aware of an explicit expression for J_0^0 in appendix 2 of Barquins and Maugis (59) taken from Dahan (60), prior to the completion of this final report.

halfspace are functions of Poisson's ratio ν, which substantiates the choice of ν alone to describe the elastic properties of the halfspace in the dimensional analysis described in section 6.

7.1 Principal Stresses in a Halfspace Under Axisymmetric Indentation

The principal stresses $\sigma_1 > \sigma_2 > \sigma_3$ in a halfspace subjected to indentation by an axisymmetric cylindrical indenter (figures 42– 44) can be determined by finding the eigenvalues of the following matrix:

$$\begin{pmatrix} \sigma_r & 0 & \tau_{rz} \\ 0 & \sigma_\theta & 0 \\ \tau_{rz} & 0 & \sigma_z \end{pmatrix} \quad , \tag{24}$$

which are

$$\sigma_1 = \frac{1}{2}\left(\sigma_r + \sigma_z + \sqrt{\sigma_r^2 - 2\sigma_r\sigma_z + 4\tau_{rz}^2 + \sigma_z^2}\right) \quad , \tag{25}$$
$$\sigma_2 = \sigma_\theta \quad ,$$
$$\sigma_3 = \frac{1}{2}\left(\sigma_r + \sigma_z - \sqrt{\sigma_r^2 - 2\sigma_r\sigma_z + 4\tau_{rz}^2 + \sigma_z^2}\right) \quad .$$

We also plot the normalized vertical displacement $\frac{u_z}{\epsilon}$ of the halfspace (figure 45) using both the exact solution from Sneddon's text (*25*) as well as an approximate solution derived by using both a series expansion approximation of the Bessel function $J_0(p\rho)$ near the origin and the asymptotic expansion of $J_0(p\rho)$ for large ρ that appears in equation 18 or equation 23 in the term involving

$$J_0^0 = \int_0^\infty e^{-\zeta p}\text{sinc}(p)\,J_0(p\rho)\,dp \quad . \tag{26}$$

We note that Sneddon's text (*25*) and other references on this topic provide the solution only for the halfspace surface displacement field, because of the difficulty in evaluation of J_0^0; the topic of determining the displacement field $\frac{u_z}{\epsilon}$ throughout the entire halfspace will be the subject of an upcoming publication. Finally, we use the exact indentation solution for the surface displacement of a halfspace found in Sneddon's text (*25*) (also plotted in figure 45) to validate our axisymmetric peridynamic code in section 10.3.
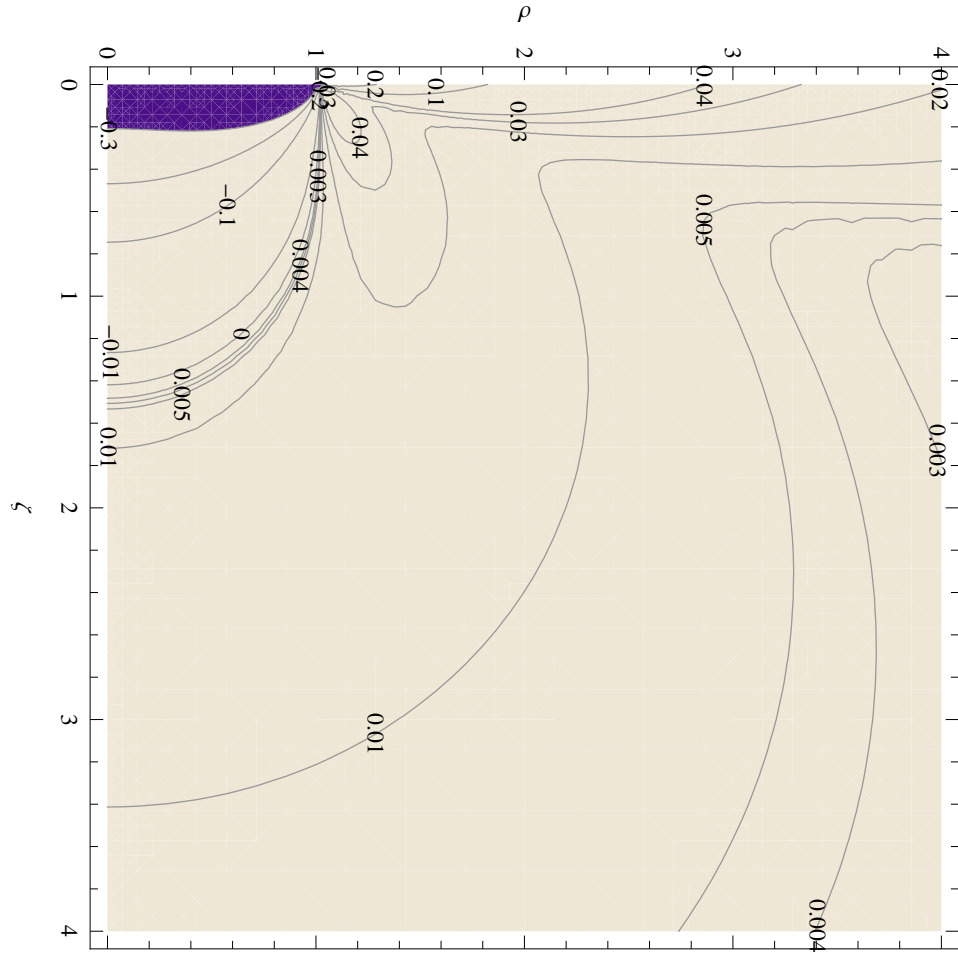
Figure 42. $\frac{\sigma_1}{p_m}$ contours in the halfspace for $\nu = \frac{\lambda}{2(\lambda+\mu)} = 0.1679$, where $\lambda = 15.833$ GPa, $\mu = 31.3$ GPa using the Lamé parameters for fused silica derived from Scheidler (*20*).
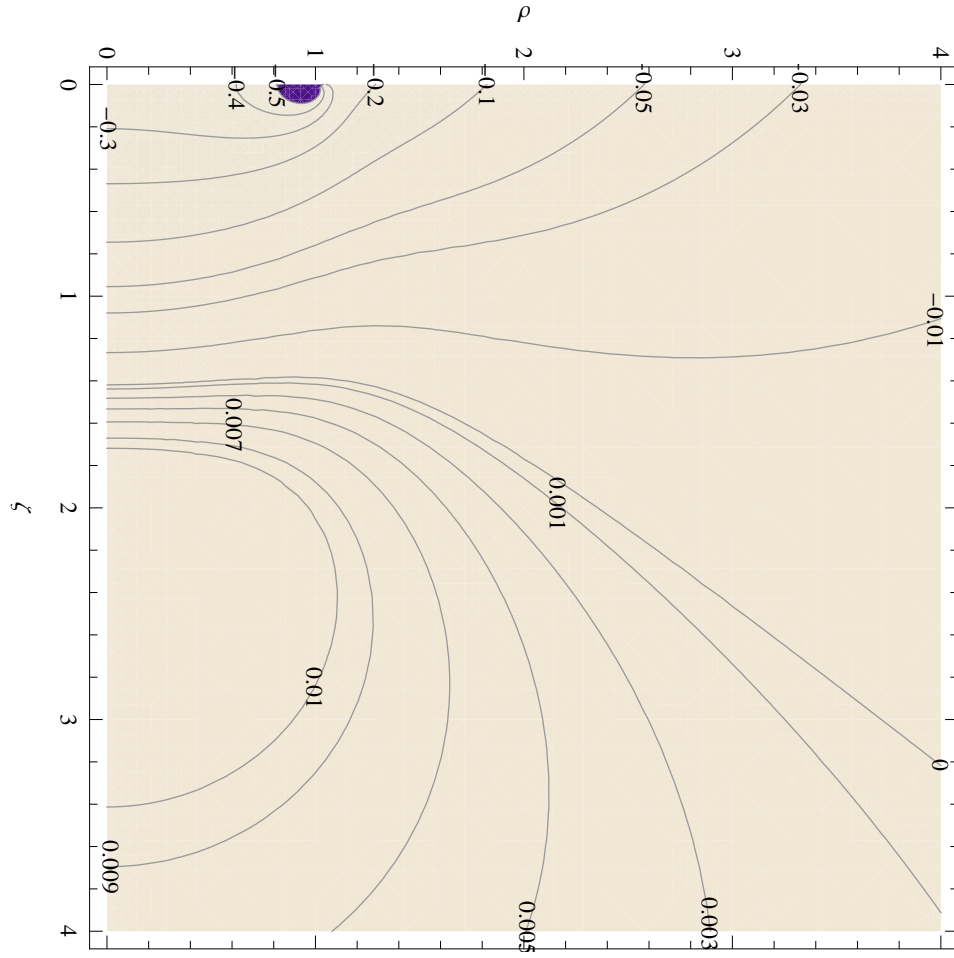
Figure 43. $\frac{\sigma_2}{p_m}$ contours in the halfspace for $\nu = \frac{\lambda}{2(\lambda+\mu)} = 0.1679$, where $\lambda = 15.833$ GPa, $\mu = 31.3$ GPa using the Lamé parameters for fused silica derived from Scheidler (20) .
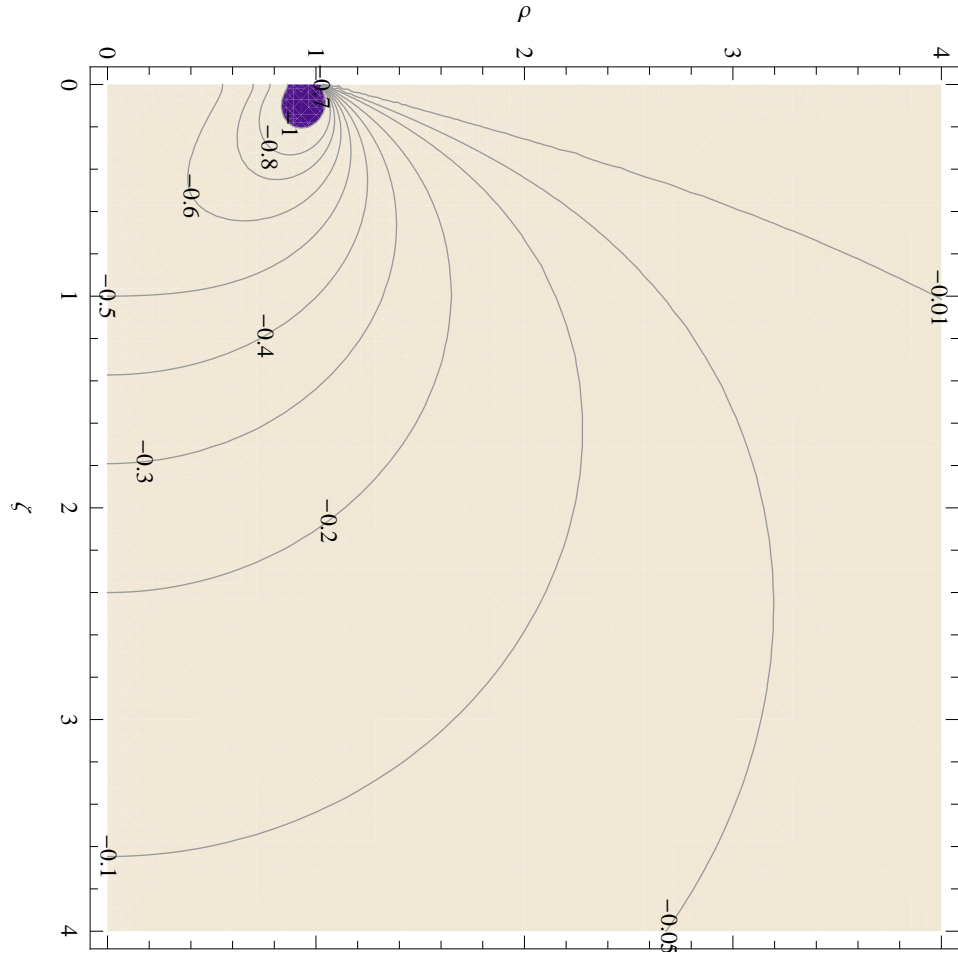
Figure 44. $\frac{\sigma_3}{p_m}$ contours in the halfspace for $\nu = \frac{\lambda}{2(\lambda+\mu)} = 0.1679$, where $\lambda = 15.833$ GPa, $\mu = 31.3$ GPa using the Lamé parameters for fused silica derived from Scheidler (20) .
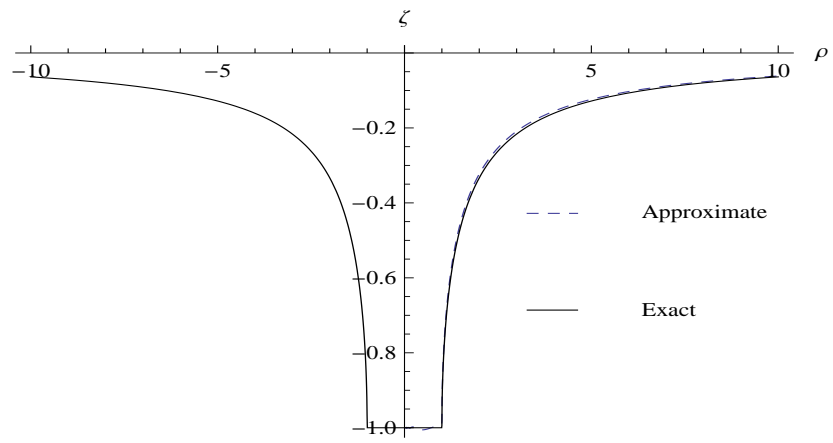
Figure 45. Deformed surface $\frac{u_z}{\epsilon}$ of the halfspace for $\nu = \frac{\lambda}{2(\lambda+\mu)} = 0.1679$, where $\lambda = 15.833, \mu = 31.3$ using the Lamé parameters for fused silica derived from Scheidler (20) .

8. Quantum Mechanics Modeling of Densification and Bulk Modulus of Silica Versus Pressure

A detailed understanding of the densification process and structural changes in amorphous solids under pressure is appealing for both experimental and simulation work. One of the interesting questions is about the nature of the structural transformation between low and high density amorphous phases. To model the structure under pressure from first principles, we used models with different densities, number of atoms, and different ring statistics. We used two different methods to generate the random connected networks (1) a Monte-Carlo bond switching model (72- and 114-atom models) and (2) MD simulated annealing of melted silica. The ring statistics could be described by plots of ring size distribution, as seen in figure 46. The faster the quenching of the melt is, the wider is the distribution of the ring sizes. Here is an example of slow quenching with ring distributions from 4 to 8 member rings, which corresponds to the quartz-like structure of the 114-atom model. Two other models with 72 and 192 atoms have wider distribution of the ring sizes from 3 to 12 member rings; for reference, quartz has only 6 member rings. Three to four member rings have a low concentration, but play an important role because they correspond to the most reactive sites. The angles between the $Si - O - Si$ atom, and the $O - Si - O$ atom distributions also convey important information about structural changes under certain pressure (figure 47).
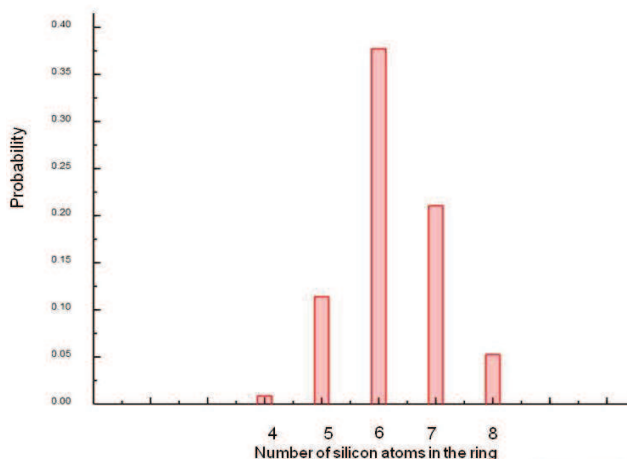
Figure 46. Ring distribution for the 114-atom model.
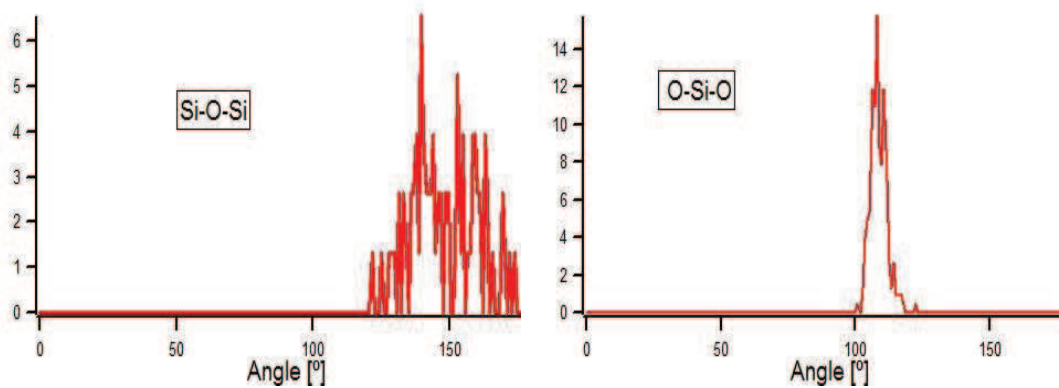
Figure 47. Two types of angle distribution in the 114-atom model.

By relaxing the internal coordinates under compressive or tensile pressures at normal conditions, we found that the $Si - O - Si$ angle ranges between 130° and 180°, while the tetrahedral units are preserved. This result is in good agreement with previous theoretical and experimental results of Mauri et al. (*61*). Clear signs of structural transformations in silica under the pressure may be seen from the calculated mass density (figure 48). We did the calculations of density after optimizing the shape and volume of the unit cell without projections in real space. The analysis used the Projector Augmented Wave (PAW) method implemented in the Vienna ab initio simulation package (VASP) code described in Kresse and Hafner (*62*).

In all three models, one may see two slopes of density, which might be related with different types of structural changes. One occurs up to 20–30 GPa, and another region is from 30–50 GPa. Some signatures of the two phases may be seen from the x-ray absorption experiments of Sato and Funamori (*15*) (figure 49).

To understand what is so special with these two stages of structural transformation in silica, we did angle distribution analysis under pressures similar to that depicted in figure 47. It turned out that in the first region there is not much change in $O - Si - O$ distribution, but discernible changes in $Si - O - Si$ distribution indicating that up to 20–30 GPa there is a squeezing of space between tetrahedra and not much distortion of tetrahedrons. Each O atom has two nearest neighbors; each Si atom has four nearest neighbors. At pressures higher than 30 GPa, silica becomes very dense, and both the $Si - O - Si$ and $O - Si - O$ angles change, revealing transformation in both the tetrahedra and the space between them.

58
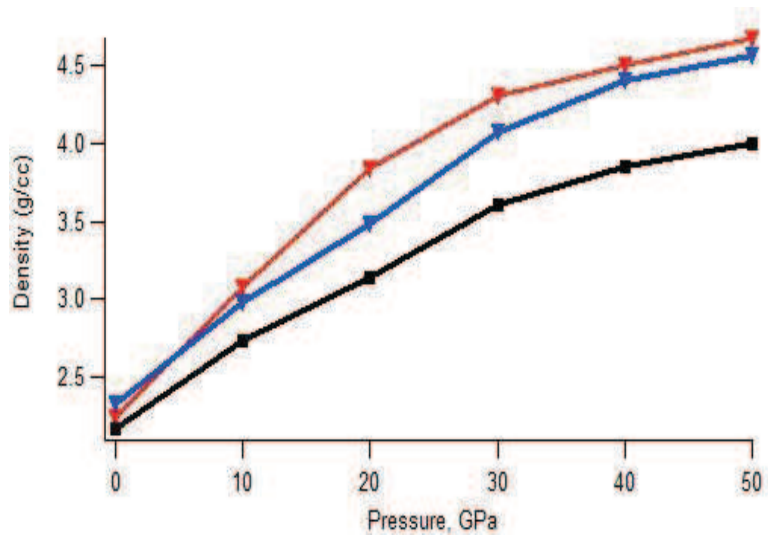
Figure 48. Density of fused silica as a function of pressure for 72-atom (▼),
114-atom (▼), and 192-atom (■)models.
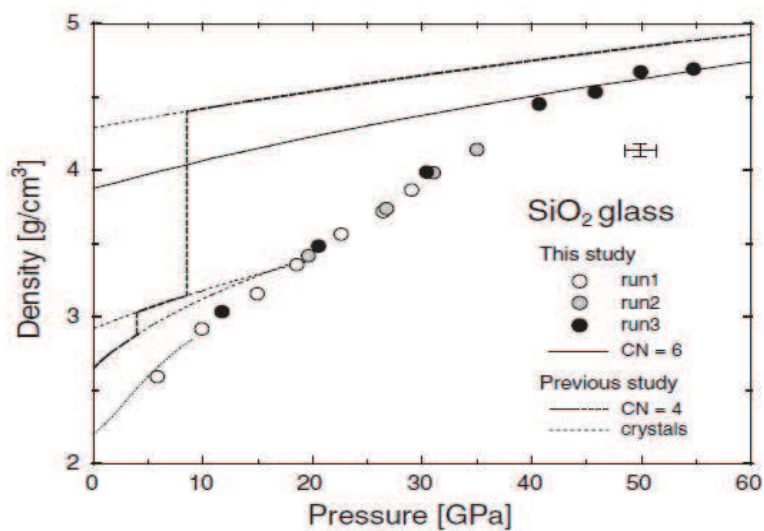
Figure 49. Experimental density of fused silica after Sato and Funamori (*15*).

At 40–50 GPa, severe distortion of the tetrahedrons resulting in formation of sixfold-coordinated Si atoms (figure 50). The density functional theory (DFT) observation of the sixfold-coordinated atoms confirms the assumption suggested in Sato and Funamori (*15*).

A manifestation of the two phases of silica densification might exhibit the unusual behavior of the elastic constants, particularly the bulk modulus. We calculated the bulk modulus from the stress-strain relationship for 114-atom model. The bulk modulus of fused silica generally increases with pressure, but unusual behavior of the pressure dependence up to 20 GPa may be related to the densification of the space between the tetrahedra (figure 51). A second region after 20 GPa with significant increase of bulk modulus corresponds to the densely packed tetrahedra.
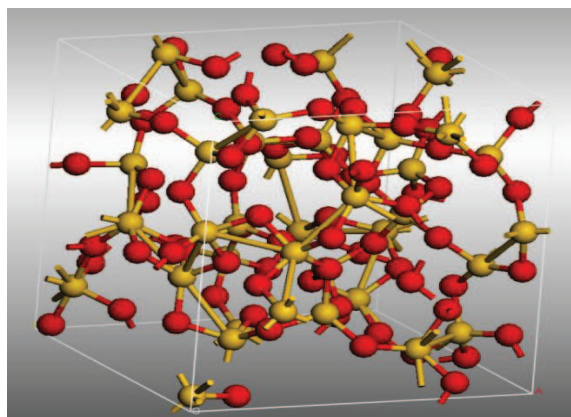
Figure 50. Fused silica structure under 50 GPa with sixfold-coordinated Si atoms.
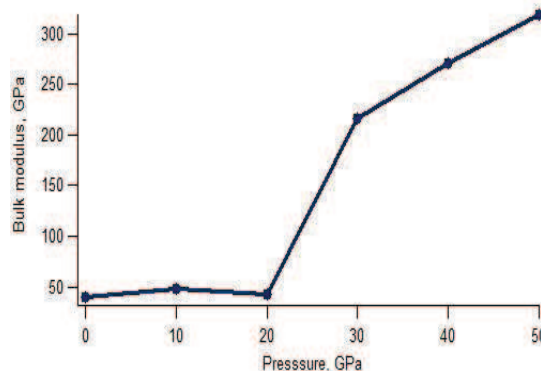
Figure 51. Bulk modulus of fused silica as a function of pressure.

8.1 Force Matching Pair Potentials for Borosilicate Glasses

To generate pair potentials for borosilicate glasses, we used the FM method as applied by Izvekov and Rice (*14*). The method is based on DFT calculations of trajectories in the Born-Oppenheimer approximation at 5000 K. The pair potentials for $S - B$ and $B - O$ generated using the method are shown in the figure 52.

Pair $Si - Si$, $Si - O$, and $O - O$ potentials are similar to those used for pure silica MD calculations. The numerical pair potentials include to a certain extent many body interactions since they were generated based on force matching of DFT calculations.

(a)   (b)
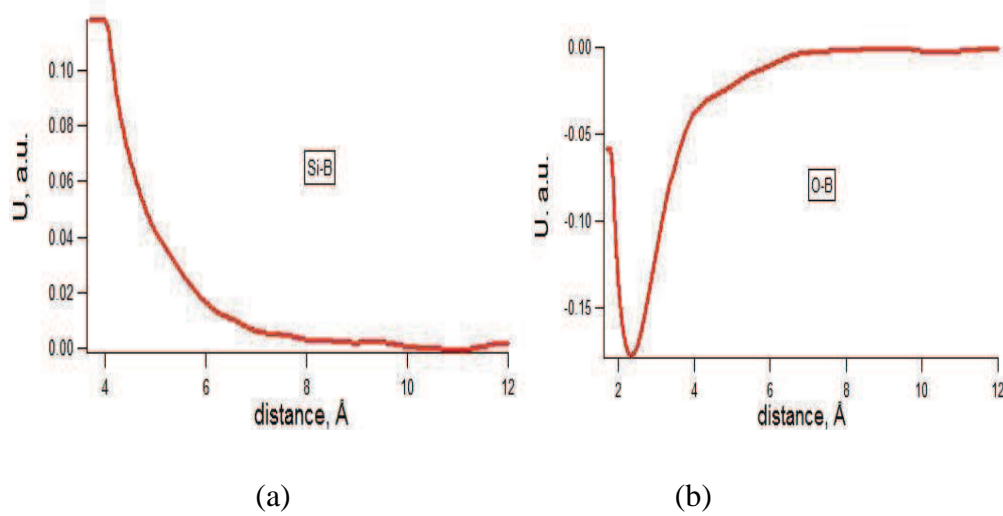
Figure 52. Pair potentials for (a) $Si - B$ and (b) $O - B$.

8.2 Simulation of Vibration Spectra of Amorphous SiO_2

Given the large variety of structural building blocks of amorphous SiO_2, there is s need for a fundamental description of the random lattice vibrations, particularly those that are IR and Raman active. In this section, IR and Raman spectra were computed using DFT for both crystalline and amorphous SiO_2. In an insulating crystal, the frequency and the intensity of the Raman peaks are determined by the zone-center phonon frequencies and the Raman tensor. The phonon frequencies are determined by the dynamical matrix, dielectric constant, and Born effective charges. The Born effective charge tensor of an ion is the partial derivative of the macroscopic polarization with respect to a periodic displacement of all the periodic images of that ion at zero macroscopic electric field. Calculations are done with the CASTEP code (*63*) using

norm-conserving pseudopotentials and plane waves with 600 eV cutoff. The calculated IR spectrum reproduces the main peaks observed in α-quartz as shown in figures 53 and 54.
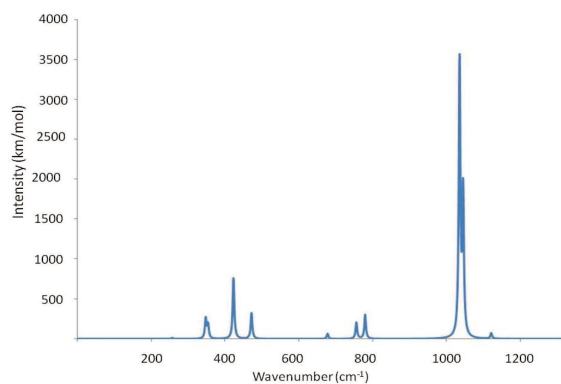
Figure 53. Calculated IR spectrum.
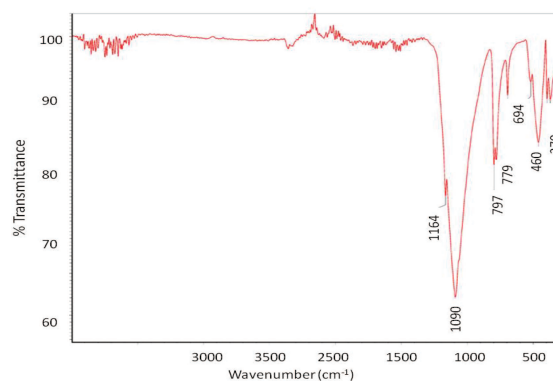
Figure 54. IR spectrum was registered on Nicolet 6700 FT-IR spectrometer.

The atomistic and charge relaxed model and scaled arrows indicating the main vibration modes are shown figure 55.
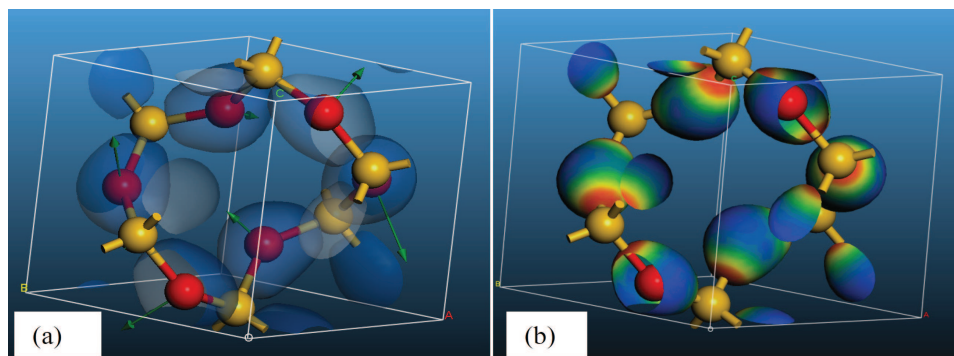
Figure 55. (a) Relaxed atomic structure and charge total distribution isosurface at value 0.36 together with arrows indicating vibration modes, and (b) distribution of local self consistent potential.

The Raman spectrum calculated in linear response approximation is shown in figure 56. The calculated spectrum reproduces two experimental frequencies at 466 and 205 cm^{-1}. The calculation of vibration spectra of amorphous SiO_2 depends on the atomic and topological model of silica, ring size, and density. The 72-atom model obtained using the bond switching algorithm (64) with random angles and no broken bonds was used for computing the vibration spectra. The structure has a distribution of 4–8 rings (figure 57) and mass density of 2.145 g/cm^3.

The calculated IR spectrum of the silica model is shown in figure 58. The main vibration modes corresponding to the peaks of the intensity are shown by scaled arrows in figure 59a.

It is evident that there is more charge within random rings than in quartz and the main vibration modes are associated with atoms located in larger rings. Peaks around 474 and 1188 cm^{-1} are seen in simulated curve of figure 53. The IR band at 800 cm^{-1} can be assigned to $Si - O - Si$ symmetric stretching vibrations, whereas the IR band at 474 cm^{-1} is due to $O - Si - O$ bending vibrations. The calculated Raman spectrum of silica is shown in figure 60.

In the experimental Raman spectra of silica shown in figure 61, three regions are typically specified (65). The broadband around 490 cm^{-1} (D1 band), peak around 600 cm^{-1} (D2 band) (attributed to symmetric breathing mode of 3–4 member rings), and peak around 800 cm^{-1} (assigned to the $Si - O$ stretching).

The calculated Raman spectra from figure 60 reproduce the three main regions of the spectrum in figure 61 and the methodology of calculation will be used for identifying signatures of non-standard coordination of silica atoms at high pressures.
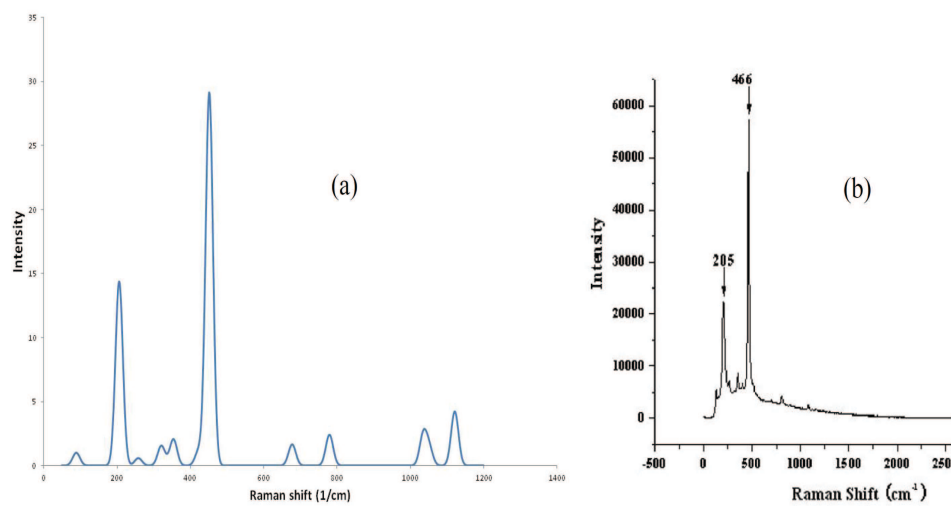
Figure 56. Raman intensity of quartz (a) calculated and (b) experimental (*21*).
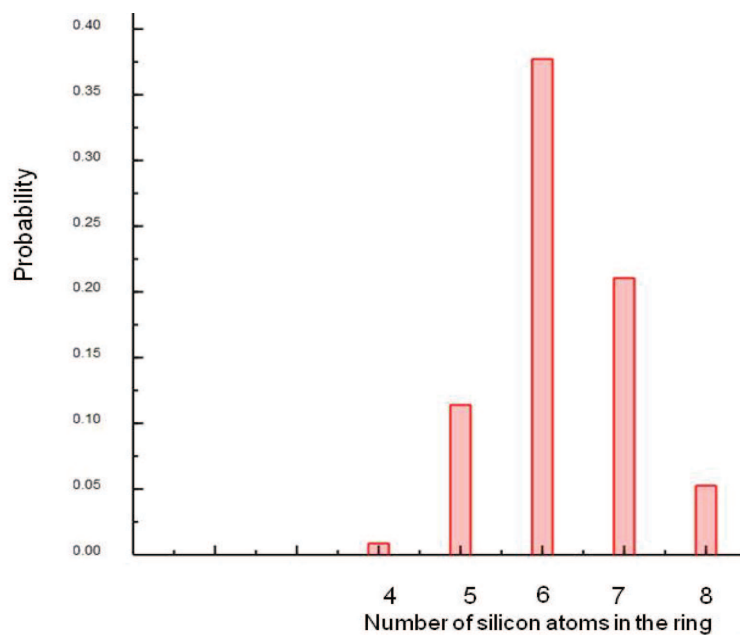
Figure 57. Distribution of rings in 72-atom model.   The six member rings have
the highest concentration in the model.
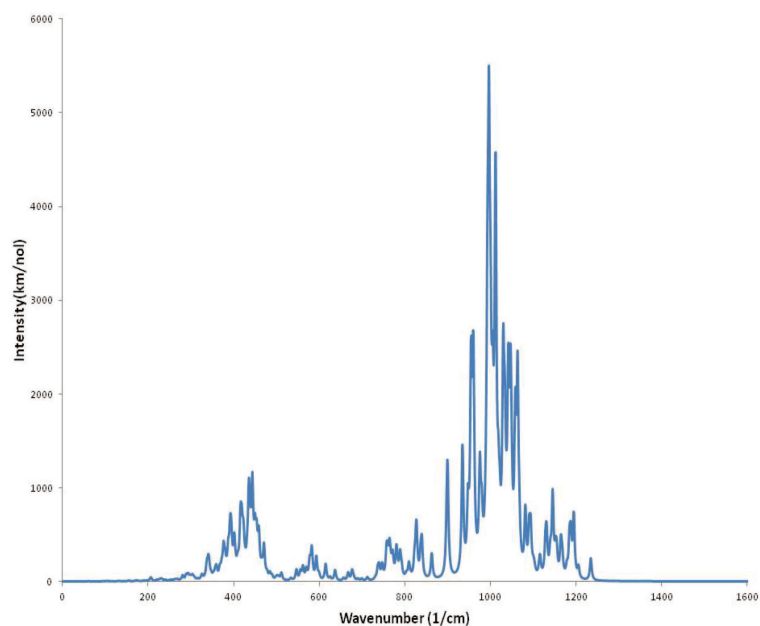
Figure 58. IR spectrum of the 72-atom silica model.

(a)   (b)
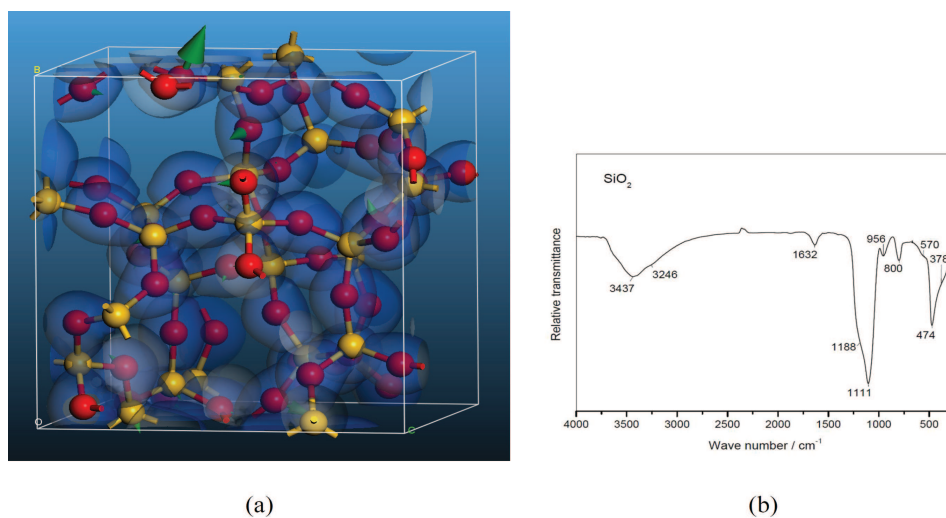
Figure 59. (a) The main vibration modes in silica are shown by scaled arrows.
The semi-transparent clouds represent isosurface of total charge
distribution at a value of 0.35 and (b) experimental Fourier transform
infrared (FTIR) spectrum of precipitated amorphous SiO_2 (22).
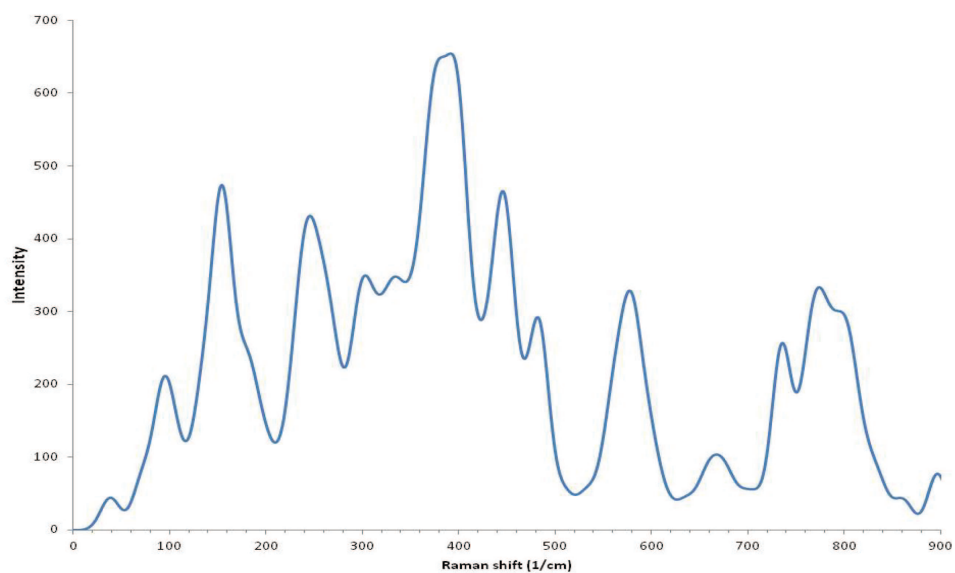
Figure 60. Raman spectra of 72-atom model of silica using 10 cm^{-1} smearing, 10 K temperature, and Ar laser wavelength.
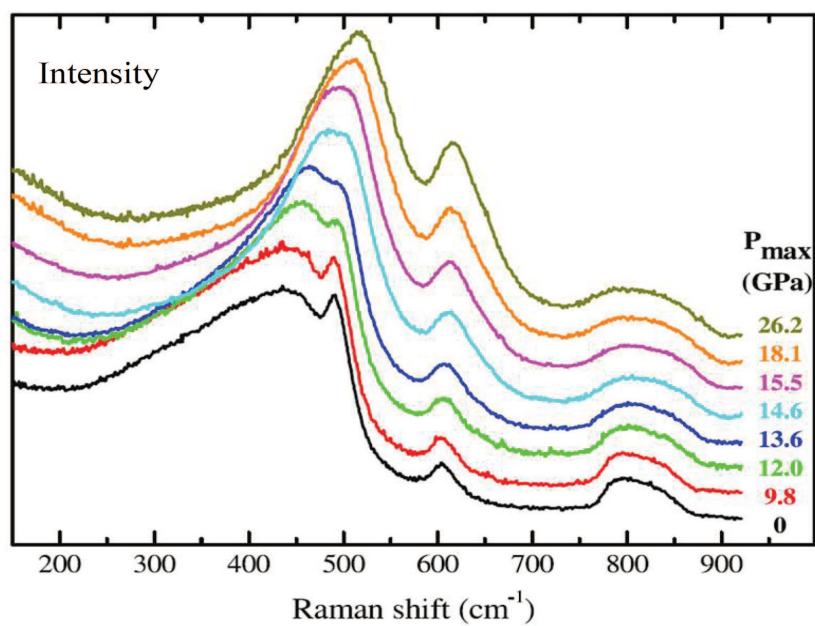
Figure 61. Experimental Raman spectra of silica at ambient conditions (lowest curve).

9.   Continuum Equation-of-state Model Development

Established processes to develop constitutive models for use in large-scale analysis and design simulations are heavily influenced by the vast body of work on metals. Typically, a model is split into an EOS, relating pressure, density, energy, and temperature, and a strength model, which relates the deviatoric part of the stress tensor to the time history of the strain rate, temperature, and state variables. This is the context of the glass EOS in Gazonas et al. (*66*), where a polyamorphic model was used, in conjunction with high and low pressure EOS models, to represent the permanent volume change in glass at high pressures (in excess of 10 GPa).

The model assumptions are evaluated by comparing simulation results with velocity profiles obtained from gas gun experiments by Alexander et al. (*23*). The experimental results are shown for three different impact velocities in figure 62a. The initial velocity ramp from 0 to 0.2 km/s results from the decreasing modulus with pressure, which is not captured by the current model. At velocities of approximately 0.6 km/s, there is a kink associated with the polyamorphic transformation. The high velocity curve (208 m/s impact velocity) rises abruptly after the transformation point, and caps at a velocity consistent with the initial velocity and shock impedance of the flyer. The transformation is nearly over driven at this high velocity, in that there is very little shift between the two vertical sections of the curve. The lower curve (137 m/s) shows a gradual rise associated with the kinetics of the transformation. It reaches the peak velocity by the end of the plot. The profile from the intermediate velocity experiment retains some curvature due to the transformation kinetics, but the steady velocity is attained quickly.

Results from using the initial model, with separate elastic-plastic and polyamorphic transformations, in gas gun simulations yields velocity profiles displaying a three-wave structure (figure 62b) rather than the two waves seen in the experiments. The model kinetics were assumed to be fast in these simulations to accentuate the steps. The first rise in the profile ends with the HEL associated with the elastic-plastic transition. The second rise ends with the volume change from the polyamorphic transformation, and the third rise terminates with the maximum particle velocity. From this comparison, it is evident that the elastic-plastic and polyamorphic transformations must occur concurrently, or an extra step will appear in the velocity profile. Physically, this implies that the atoms move to accommodate shear strain as they are rearranging to accommodate the volume change.
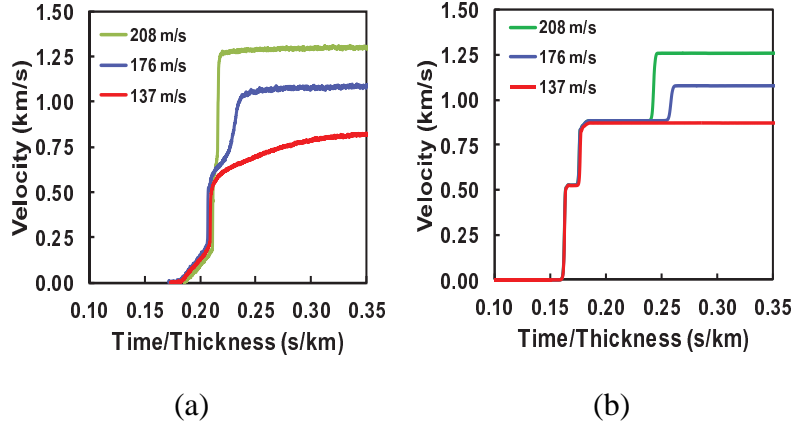
Figure 62. Velocity profiles from: (a) gas gun experiments on borosilicate glass from Alexander et al. (*23*) and (b) simulations using independent functions for the elastic-plastic transition and the polyamorphic transformation.

The modeling goal is to couple inelastic deviatoric deformation and volume change. There is no experimental data to guide the functional form for the coupling, so a simple quadratic flow potential model is assumed:

$$\phi = 0 = \sqrt{\alpha \sigma_e^2 + p^2} - \bar{p}(\lambda). \tag{27}$$

Here, σ_e is the effective stress, p is the pressure, and $\bar{p}$ is a function of the volume fraction of the low pressure polyamorph, λ. α is a parameter regulating the relative influence of the deviatoric stress compared to the pressure.

Following concepts used in metal plasticity, the direction of inelastic flow is assumed to be normal to the flow potential:

$$\mathbf{d}_{inelas} = \Lambda \frac{\partial \phi}{\partial \boldsymbol{\sigma}}, \tag{28}$$

where $\mathbf{d}_{inelas}$ is the inelastic part of the rate of deformation tensor, $\mathbf{d}$, which is decomposed,

68

additively, into elastic and inelastic parts $\mathbf{d} = \mathbf{d}_{elas} + \mathbf{d}_{inelas}$. The elastic part is also a function of the stress tensor through the elastic moduli. Together these provide a coupled set of equations for Λ in equation 28, which is determined by an iterative procedure.

The volume fraction of the low density polyamorph is assumed to evolve through a kinetic relation

$$\dot{\lambda} = \beta(\lambda - \lambda_\infty)^3 e^{(\nu \frac{T - T_{ref}}{T_{ref}})} \tag{29}$$

where β and ν are parameters and λ_∞ represents the equilibrium fraction of the low density polyamorph. The equilibrium phase fraction

$$\lambda_\infty = \left(\frac{\bar{p}_f - \bar{p}}{\bar{p}_f - \bar{p}_t} \right)^2 \tag{30}$$

is a function of the applied loading, $\bar{p}$, the threshold pressure at which the transformation begins, $\bar{p}_t$, and the pressure at which the glass is fully transformed to the high density polyamorph, $\bar{p}_f$.

These equations were implemented into a finite element code and the gas gun simulations run. Figure 63a shows the results with the kinetic parameter set high ($\beta = 100$) to give the equilibrium response. From these calculations it is evident that a two-wave structure is produced, indicating that the inelastic deformation and polyamorph transformation are occurring simultaneously. Figure 63b shows the results with a kinetic parameter ($\beta = 3$) set to reproduce the basic features observed in the experimental data plotted in figure 62a.

The simulation results demonstrate some general model features necessary to reproduce experimental observations from high-pressure gas gun experiments. The model must couple the deviatoric stress and the pressure for the polyamorphic transformation, and a kinetic model is necessary to introduce time-dependent rises in the response. Other features may also be necessary, but these two have a major impact and provide a well-defined starting point for model improvement. The particular functional relations assumed for this model are conjecture guided by experience in modeling metals. Hence, appropriate data are needed to guide model development. While it will be possible to tune a kinetic parameter based on data from current experimental methods, existing experimental techniques will provide little information on the

(a)   (b)
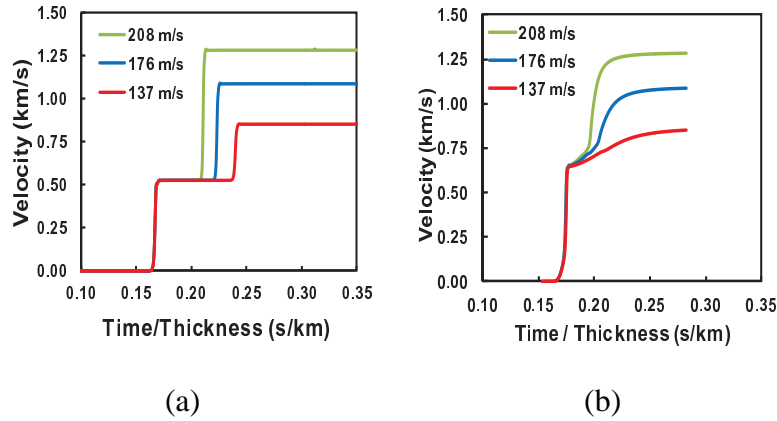
Figure 63. Gas gun simulation results for a model with concurrent elastic-plastic transition and polyamorphic transformation and with (a) a high kinetic parameter for rapid transformation and (b) the kinetic parameter adjusted to resemble experiments.

functional form for the kinetic relation or the flow function dependence on deviatoric stress and pressure. The alternative, and the approach pursued in the program, is to determine the functional relationships and parameters through multiscale modeling approaches.

9.1   Summary of Continuum Equation-of-state Model Development

The EOS development included the non-monotonic change in bulk modulus with pressure and a polyamorphic transformation from a lower density amorphous state to a higher density configuration. The EOS form near the reference density was guided by previously published pressure-density data. Figure 64 depicts the model dependence of the pressure and bulk modulus on density along with the data of Zha et al. (*24*). The agreement is reasonable up to 10 GPa, which is near the pressure where the polyamorphic transformation begins. The EOS for the high density polyamorph was assumed to follow a Murnaghan form and the model constants were determined by fitting Hugoniot data from Sugiura et al. (*67*) and Alexander (*23*). This fit is complicated by a lack of data. In particular, the reference density for the high density phase is not easily obtained, since it must be measured after release from high pressures.

The remaining component of the EOS model is the temperature-dependent kinetic relation connecting the low and high density polyamorphs. Here, it is assumed that the transformation rate is proportional to the cube of the difference between the current phase fraction and the equilibrium phase fraction. The model is assessed by comparing interface velocity predictions

70
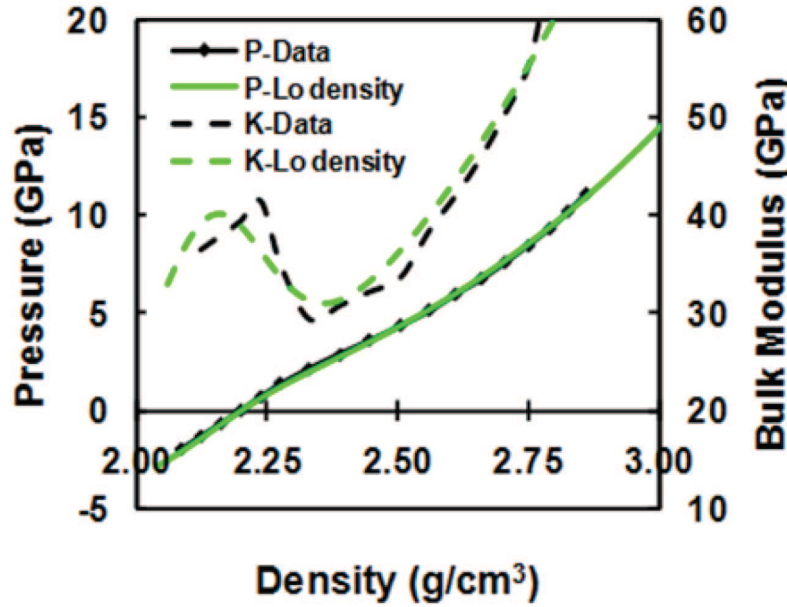
Figure 64. Model fit of pressure and bulk modulus with data from Zha et al. (*24*).

from gas gun simulations with available data in figure 62a. The curvature of the velocity data is due entirely to the kinetic relation, and it is capturing much of the inflection and curvature. The timing of the rises in the curves is off, which suggests that the underlying response may be too stiff in the elastic range and that the volume change associated with the transformation may be too large. These can be adjusted when more data are available.

10.   A Perfectly Matched Layer for Peridynamics in Two Dimensions

In this section, we develop a peridynamic method for modeling nanoindentation experiments in fused silica and other chemically substituted glasses. Originally introduced in Silling (*68*), peridynamics is a non-local formulation of elastodynamics, which can more easily incorporate discontinuities such as cracks and damage. Derivatives of field variables in the classical continuum model are replaced by integrals over a small neighborhood of microelastic kernels, which replaces the standard constitutive relation. In its discretized form, an elastic solid is treated as a collection of particles or nodes, each connected to its neighbors by breakable bonds. Bond breakage can be defined to occur when a bond is stretched past some predetermined limit.

The end result is a method capable of predicting crack growth in brittle elastic materials (*69–74*). The original formulation was limited to materials with a fixed Poisson's ratio of 0.25; however, state-based peridynamics was introduced allowing for more flexible constitutive relations (*75*). As becomes clear later, state-based peridynamics allows for an auxiliary field formulation, which is necessary to implement a perfectly matched layer (PML). While most peridynamics work has focused on simulating problems with free or fixed boundary conditions, there are applications in which the simulation of an infinite medium may be useful, such as crack propagation in a halfspace or nanoindentation problems. Absorbing boundary conditions are one way of simulating an infinite medium as any impinging waves are suppressed so they do not reflect back into the simulation. A PML is such an absorbing boundary, and was originally introduced for electromagnetic simulations (*76, 77*). PMLs differ from traditional absorbing boundary conditions in that they are an absorbing layer with a finite width, placed between the computation region of interest and the truncation of the grid or mesh. They can also be thought of as an anisotropic absorbing material, which is why the flexibility of a state-based peridynamics is necessary. A PML was applied to one-dimensional (1-D) peridynamics (*78*), which used the results of Du et al. (*79*) to formulate an auxiliary field equation. This approach required a matrix representation of the auxiliary field, which may be memory prohibitive in higher dimensions.

10.1 Two-dimensional (2-D), State-based Peridynamics

The continuum equation of motion in an elastic solid can be stated as

$$\rho\frac{\partial^2}{\partial t^2}\mathbf{u} = \nabla \cdot \overline{\boldsymbol{\sigma}} + \mathbf{b} = \nabla \cdot (\overline{\mathbf{c}} : \overline{\boldsymbol{\epsilon}}) + \mathbf{b}, \tag{31}$$

where $\rho(\mathbf{x})$ is the density; $\mathbf{u}(\mathbf{x}, t)$ is the displacement; $\overline{\boldsymbol{\sigma}}(\mathbf{x}, t)$ is the stress tensor; $\overline{\boldsymbol{\epsilon}}(\mathbf{x}, t)$ is the strain tensor; $\overline{\mathbf{c}}$ is the stiffness matrix for plane strain, defined by Young's modulus E, Poisson's ratio ν, or Lamé parameters λ and μ; and $\mathbf{b}(\mathbf{x})$ is a body force (*80*). (Throughout, boldface type denotes a vector and a boldface variable with an overbar denotes a tensor.) Equation 31 is a local formulation because the divergence of the stress (and gradient of the displacement implied in its definition) represents a local operation on a variable. In other words, the action of $\nabla \cdot \overline{\boldsymbol{\sigma}}$ only depends on $\overline{\boldsymbol{\sigma}}$ at a single spatial point. In problems involving discontinuities, such as cracks, the divergence at such discontinuities is not well defined, leading to numerical implementation problems. Peridynamics proposes replacing $\nabla \cdot \overline{\boldsymbol{\sigma}}$ with a nonlocal operation that nonetheless also represents a force. Here, we use the state-based peridynamics (*75*), rather than the original bond-based version (*68*). A PML application requires an auxiliary field formulation, as it is essentially an anisotropic absorbing material, if a non-physical one. Consequently, a state-based peridynamic formulation is necessary to implement the required constitutive relations in the

72

absorber. The state-based peridynamics uses a family of bonds to determine a given force rather than a single bond independently. This more general approach allows for inelastic behavior and more general elastic behavior, and is governed by

$$\rho\frac{\partial^2}{\partial t^2}\mathbf{u} = \int_{\mathcal{H}_{\mathbf{x}}}\left(\overline{\mathbf{T}}[\mathbf{x},t]\langle\mathbf{x}'-\mathbf{x}\rangle - \overline{\mathbf{T}}[\mathbf{x}',t]\langle\mathbf{x}-\mathbf{x}'\rangle\right)dV' + \mathbf{b},\tag{32}$$

where $\mathcal{H}_{\mathbf{x}}$ is the horizon region, defined as a circle centered at $\mathbf{x}$ with radius δ, and $\overline{\mathbf{T}}[\mathbf{x},t]\langle\mathbf{x}'-\mathbf{x}\rangle$ is a peridynamic vector state, with parameters in the square brackets indicating variables that act as arguments to any functions that define the vector state and variables in the angle brackets acting as arguments to the vector state itself. In the state-based formulation, the deformation gradient, given by

$$\overline{\mathbf{F}} = \overline{\mathbf{I}} + \mathbf{u}\nabla,\tag{33}$$

can be approximated as a vector state as

$$\overline{\mathbf{F}}[\mathbf{x},t] = \left[\int_{\mathcal{H}_{\mathbf{x}}}C(|\boldsymbol{\xi}|)\left(\mathbf{Y}[\mathbf{x},t]\langle\boldsymbol{\xi}\rangle\otimes\boldsymbol{\xi}\right)dV_{\mathbf{x}'}\right]\overline{\mathbf{K}}^{-1},\tag{34}$$

where $C(|\boldsymbol{\xi}|) = \exp(-|\boldsymbol{\xi}|^2/\delta^2)$ is a shape function, taken as a Gaussian distribution here and with the horizon $\mathcal{H}_{\mathbf{x}}$ extended so that the shape function decays to an arbitrary, small value, taken here as 10^{-6}, $\overline{\mathbf{K}}$ is a shape tensor given by

$$\overline{\mathbf{K}}[\mathbf{x},t] = \int_{\mathcal{H}_{\mathbf{x}}}C(|\boldsymbol{\xi}|)\left(\boldsymbol{\xi}\otimes\boldsymbol{\xi}\right)dV_{\mathbf{x}'},\overline{\mathbf{K}}^{-1} = \begin{bmatrix} k_{xx}^{\text{inv}} & k_{xy}^{\text{inv}} \\ k_{yx}^{\text{inv}} & k_{yy}^{\text{inv}} \end{bmatrix},\tag{35}$$

and $\mathbf{Y}$ is a deformation vector state given by

$$\mathbf{Y}[\mathbf{x},t]\langle\boldsymbol{\xi}\rangle = \boldsymbol{\eta} + \boldsymbol{\xi},\tag{36}$$

with $\boldsymbol{\eta} = \mathbf{u}[\mathbf{x}',t] - \mathbf{u}[\mathbf{x},t]$ and $\boldsymbol{\xi} = \mathbf{x}' - \mathbf{x}$ (81).

The deformation gradient can now be substituted into Hooke's law and strain-displacement relations, giving a stress term $\overline{\boldsymbol{\sigma}}$ in terms of $\mathbf{u}$ in plane strain

$$\rho\frac{\partial^2}{\partial t^2}\mathbf{u} = \nabla\cdot\overline{\boldsymbol{\sigma}} = \nabla\cdot\left(\overline{\mathbf{c}}:\overline{\boldsymbol{\epsilon}}\right),\tag{37}$$

where

$$\overline{\boldsymbol{\epsilon}}[\mathbf{x}, t] = \frac{1}{2} \left(\nabla \mathbf{u} + \mathbf{u} \nabla \right) \approx \frac{1}{2} \left(\overline{\mathbf{F}}[\mathbf{x}, t] + \overline{\mathbf{F}}[\mathbf{x}, t]^{\mathrm{T}} - 2\overline{\mathbf{I}} \right). \tag{38}$$

Ultimately, the peridynamic vector state $\mathbf{T}$ for plane strain elasticity is given by

$$\overline{\mathbf{T}}[\mathbf{x}, t]\langle \boldsymbol{\xi} \rangle = C(|\boldsymbol{\xi}|)\overline{\boldsymbol{\sigma}}[\mathbf{x}, t]\overline{\mathbf{K}}^{-1}\boldsymbol{\xi}. \tag{39}$$

10.2 Auxiliary Field Formulation and PML Application

The first step in formulating a PML is to construct an analytic continuation to the complex plane, such as $\hat{x} = x + ig(x)$, where $g(x)$ is a given function describing the deformation (*82*). This mapping has the effect of transforming traveling waves of the form e^{ikx}, where $k = \omega/c$ is the wave number, into evanescent waves of the form $e^{ikx}e^{-kg(x)}$, thus attenuating such waves in the PML region. Applying a PML involves substituting for spatial derivatives using

$$\frac{\partial}{\partial x} \rightarrow \frac{1}{1 + i\frac{\phi(x)}{\omega}} \frac{\partial}{\partial x}. \tag{40}$$

The function $\phi(x)$ defines the extent of the PML region, i.e., when $\phi(x) = 0$ the original wave equation is obtained, and when $\phi(x) > 0$, traveling waves decay exponentially. Typically, $\phi(x)$ transitions from 0 to a constant value using a smooth function to prevent numerical reflections at the boundary between the absorbing and computational regions. Before applying a PML directly to the peridynamic equation, equation 31 is treated so that the PML application to peridynamics is clear. It is convenient to convert equation 31 to the Laplace domain, assuming e^{-st} time dependence, and express the wave equation as two coupled first-order partial differential equations, the first in $\tilde{\mathbf{u}}$ and the second in $s\tilde{\overline{\psi}} = \tilde{\overline{\sigma}}$

$$\begin{aligned} \rho s \tilde{\mathbf{u}} &= \nabla \cdot \tilde{\overline{\psi}} \\ s \tilde{\overline{\psi}} &= \overline{\mathbf{c}} : \tilde{\overline{\epsilon}}, \end{aligned} \tag{41}$$

where the Laplace transform of a variable is indicated by $\mathcal{L}\{f\} = \tilde{f}$. Expanding equation 41 into components gives five coupled equations

74

$$\rho s \tilde{u}_x = \frac{\partial}{\partial x} \tilde{\psi}_x + \frac{\partial}{\partial y} \tilde{\psi}_\tau$$

$$\rho s \tilde{u}_y = \frac{\partial}{\partial x} \tilde{\psi}_\tau + \frac{\partial}{\partial y} \tilde{\psi}_y$$

$$s \tilde{\psi}_x = (\lambda + 2\mu) \frac{\partial}{\partial x} \tilde{u}_x + \lambda \frac{\partial}{\partial y} \tilde{u}_y \tag{42}$$

$$s \tilde{\psi}_y = \lambda \frac{\partial}{\partial x} \tilde{u}_x + (\lambda + 2\mu) \frac{\partial}{\partial y} \tilde{u}_y$$

$$s \tilde{\psi}_\tau = \mu \left(\frac{\partial}{\partial y} \tilde{u}_x + \frac{\partial}{\partial x} \tilde{u}_y \right).$$

We can expand the state-based formulation into components and match terms to equation 42. Following this approach yields a viable method for performing PML substitutions. First, the state-based peridynamic equations listed above in equations 32–39 can be written explicitly as

$$\rho s \tilde{u}_x[\mathbf{x}, s] = \int_{\mathcal{H}_\mathbf{x}} C(|\boldsymbol{\xi}|) \left[\left(\tilde{\psi}_x[\mathbf{x}, s] k_{xx}^{\text{inv}} + \tilde{\psi}_\tau[\mathbf{x}, s] k_{yx}^{\text{inv}} \right) \xi_x + \left(\tilde{\psi}_x[\mathbf{x}', s] k_{xx}^{\text{inv}'} + \tilde{\psi}_\tau[\mathbf{x}', s] k_{yx}^{\text{inv}'} \right) \xi_x \right] dV_{\mathbf{x}'}$$

$$+ \int_{\mathcal{H}_\mathbf{x}} C(|\boldsymbol{\xi}|) \left[\left(\tilde{\psi}_x[\mathbf{x}, s] k_{xy}^{\text{inv}} + \tilde{\psi}_\tau[\mathbf{x}, s] k_{yy}^{\text{inv}} \right) \xi_y + \left(\tilde{\psi}_x[\mathbf{x}', s] k_{xy}^{\text{inv}'} + \tilde{\psi}_\tau[\mathbf{x}', s] k_{yy}^{\text{inv}'} \right) \xi_y \right] dV_{\mathbf{x}'},$$

$$\rho s \tilde{u}_y[\mathbf{x}, s] = \int_{\mathcal{H}_\mathbf{x}} C(|\boldsymbol{\xi}|) \left[\left(\tilde{\psi}_\tau[\mathbf{x}, s] k_{xx}^{\text{inv}} + \tilde{\psi}_y[\mathbf{x}, s] k_{yx}^{\text{inv}} \right) \xi_x + \left(\tilde{\psi}_\tau[\mathbf{x}', s] k_{xx}^{\text{inv}'} + \tilde{\psi}_y[\mathbf{x}', s] k_{yx}^{\text{inv}'} \right) \xi_x \right] dV_{\mathbf{x}'}$$

$$+ \int_{\mathcal{H}_\mathbf{x}} C(|\boldsymbol{\xi}|) \left[\left(\tilde{\psi}_\tau[\mathbf{x}, s] k_{xy}^{\text{inv}} + \tilde{\psi}_y[\mathbf{x}, s] k_{yy}^{\text{inv}} \right) \xi_y + \left(\tilde{\psi}_\tau[\mathbf{x}', s] k_{xy}^{\text{inv}'} + \tilde{\psi}_y[\mathbf{x}', s] k_{yy}^{\text{inv}'} \right) \xi_y \right] dV_{\mathbf{x}'},$$

$$s \tilde{\psi}_x[\mathbf{x}, s] = (\lambda + 2\mu) \left[\int_{\mathcal{H}_\mathbf{x}} C(|\boldsymbol{\xi}|) \left(\tilde{Y}_x[\mathbf{x}, s] \xi_x k_{xx}^{\text{inv}} + \tilde{Y}_x[\mathbf{x}, s] \xi_y k_{yx}^{\text{inv}} \right) dV_{\mathbf{x}'} - 1 \right]$$

$$+ \lambda \left[\int_{\mathcal{H}_\mathbf{x}} C(|\boldsymbol{\xi}|) \left(\tilde{Y}_y[\mathbf{x}, s] \xi_x k_{xy}^{\text{inv}} + \tilde{Y}_y[\mathbf{x}, s] \xi_y k_{yy}^{\text{inv}} \right) dV_{\mathbf{x}'} - 1 \right], \tag{43}$$

$$s \tilde{\psi}_y[\mathbf{x}, s] = \lambda \left[\int_{\mathcal{H}_\mathbf{x}} C(|\boldsymbol{\xi}|) \left(\tilde{Y}_x[\mathbf{x}, s] \xi_x k_{xx}^{\text{inv}} + \tilde{Y}_x[\mathbf{x}, s] \xi_y k_{yx}^{\text{inv}} \right) dV_{\mathbf{x}'} - 1 \right]$$

$$+ (\lambda + 2\mu) \left[\int_{\mathcal{H}_\mathbf{x}} C(|\boldsymbol{\xi}|) \left(\tilde{Y}_y[\mathbf{x}, s] \xi_x k_{xy}^{\text{inv}} + \tilde{Y}_y[\mathbf{x}, s] \xi_y k_{yy}^{\text{inv}} \right) dV_{\mathbf{x}'} - 1 \right],$$

$$s \tilde{\psi}_\tau[\mathbf{x}, s] = \mu \int_{\mathcal{H}_\mathbf{x}} C(|\boldsymbol{\xi}|) \left(\tilde{Y}_x[\mathbf{x}, s] \xi_x k_{xy}^{\text{inv}} + \tilde{Y}_x[\mathbf{x}, s] \xi_y k_{yy}^{\text{inv}} \right) dV_{\mathbf{x}'}$$

$$+ \mu \int_{\mathcal{H}_\mathbf{x}} C(|\boldsymbol{\xi}|) \left(\tilde{Y}_y[\mathbf{x}, s] \xi_x k_{xx}^{\text{inv}} + \tilde{Y}_y[\mathbf{x}, s] \xi_y k_{yx}^{\text{inv}} \right) dV_{\mathbf{x}'},$$

etc. Though no derivatives appear in equations 43, the correspondence of each term to those in equation 42 is apparent and the PML substitutions can be made. For example, the first equation

in 43 can be rewritten as

$$
\begin{aligned}
\rho\left(s+\phi_x\right)\left(s+\phi_y\right)\tilde{u}_x = {} & \left(s+\phi_y\right)\int_{\mathcal{H}_\mathbf{x}} C(|\boldsymbol{\xi}|)\left(\tilde{\psi}_x[\mathbf{x},s]k_{xx}^{\mathrm{inv}}+\tilde{\psi}_{xy}[\mathbf{x},s]k_{yx}^{\mathrm{inv}}\right)\xi_x dV_{\mathbf{x}'} \\
& + \left(s+\phi_y\right)\int_{\mathcal{H}_\mathbf{x}} C(|\boldsymbol{\xi}|)\left(\tilde{\psi}_x[\mathbf{x}',s]k_{xx}^{\mathrm{inv}'}+\tilde{\psi}_{xy}[\mathbf{x}',s]k_{yx}^{\mathrm{inv}'}\right)\xi_x dV_{\mathbf{x}'} \\
& + \left(s+\phi_x\right)\int_{\mathcal{H}_\mathbf{x}} C(|\boldsymbol{\xi}|)\left(\tilde{\psi}_x[\mathbf{x},s]k_{xy}^{\mathrm{inv}}+\tilde{\psi}_\tau[\mathbf{x},s]k_{yy}^{\mathrm{inv}}\right)\xi_y dV_{\mathbf{x}'} \\
& + \left(s+\phi_x\right)\int_{\mathcal{H}_\mathbf{x}} C(|\boldsymbol{\xi}|)\left(\tilde{\psi}_x[\mathbf{x}',s]k_{xy}^{\mathrm{inv}'}+\tilde{\psi}_\tau[\mathbf{x}',s]k_{yy}^{\mathrm{inv}'}\right)\xi_y dV_{\mathbf{x}'},
\end{aligned}
\tag{44}
$$

with the remaining equations following similarly. The final step involves simply converting back to the time domain and implementing a forward Euler discretization scheme in time, and the standard one-point integration method (*74*) in space.

10.3 Results

The previous method was numerically implemented using a forward Euler method for the temporal discretization, and standard one-point integration with point-matching in space. The PML was tested on three types of problems: a wave propagation problem to demonstrate the effectiveness of the PML, two crack propagation problems (one state-based and one bond-based), and an axisymmetric indentation problem.

10.3.1 Wave Propagation

The PML was first tested on a wave propagation problem with PML boundary layers and a Gaussian distribution as an initial condition. Specifically, the x-directed displacement was set to

$$
u_x(\mathbf{x}, t=0) = e^{-200|\mathbf{x}-\mathbf{p}_{\mathrm{mid}}|^2},
\tag{45}
$$

where $\mathbf{p}_{\mathrm{mid}}$ is the mid-point of the region, which in this example was defined as $0 \leq x, y \leq 1$ and discretized with $\Delta x = \Delta y = 0.01$ m. Young's modulus for the region was set to 1 Pa, Poisson's ratio was $1/4$, and the density was 1 kg/m^3. The PML region was defined as the 0.3-m border around the 1 m-by-1 m region and used a Gaussian ramp with a width of 0.2 m, finally reaching a maximum of 50 s^{-1} for the remaining 0.1 m. For the Gaussian kernel, a horizon size of $\delta = 1.1\Delta x$ was used, and for the Heaviside kernel, a horizon of $\delta = 3.1\Delta x$ was used.

The simulation was run with both the Heaviside and Gaussian kernels, with the total strain energy shown in figure 65. The Gaussian kernel (dotted line) shows the largest drop in energy, reaching a minimum of 5.6×10^{-7}, and the Heaviside kernel (dashed line) decreases to $1. \times 10^{-4}$.
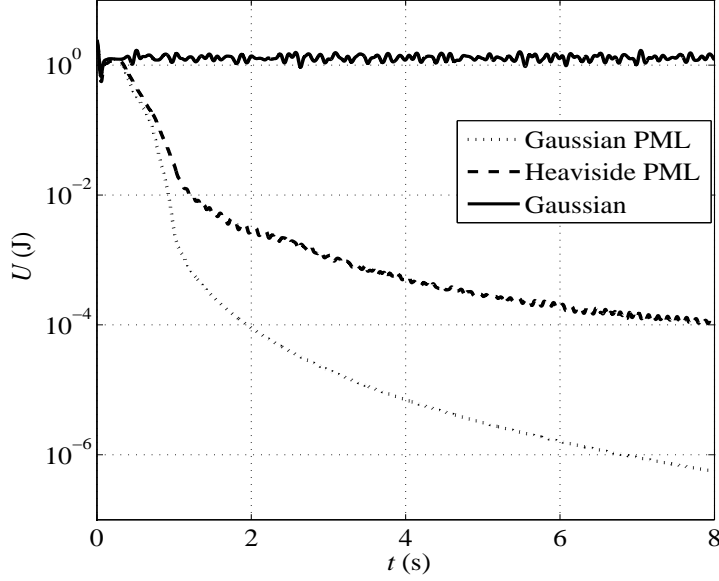
Figure 65. Total strain energy in a simulation terminated by a PML.

A bounded simulation is shown for reference as the solid line, which used a fixed displacement boundary condition and the Gaussian kernel. Figure 66 shows a waterfall plot of the x-directed displacement along the $y = 0.5$ line for the Gaussian kernel with the PML function ϕ_x shown in gray on the far end of the plot (corresponding to $t = 1$ s). Figure 67 shows the absolute value of the x-directed displacement at the edge of the PML region, in simulations terminated by a PML and with a fixed boundary condition. The wave is absorbed at the boundary with minimal reflections: as can be seen, the plots align for a time, and where they deviate (indicating a reflection from the hard boundary), the PML simulation remains in decay.

For verification, the method was compared with an exact analytical solution. Consider a cylindrically symmetric wave propagating in an infinite elastic medium with the same constitutive parameters as the above example, and with an initial condition given by

$$u_0(r) = b\left(\frac{r}{a}\right)\left[1 + \left(\frac{r}{a}\right)^2\right]^{-\frac{3}{2}} \tag{46}$$
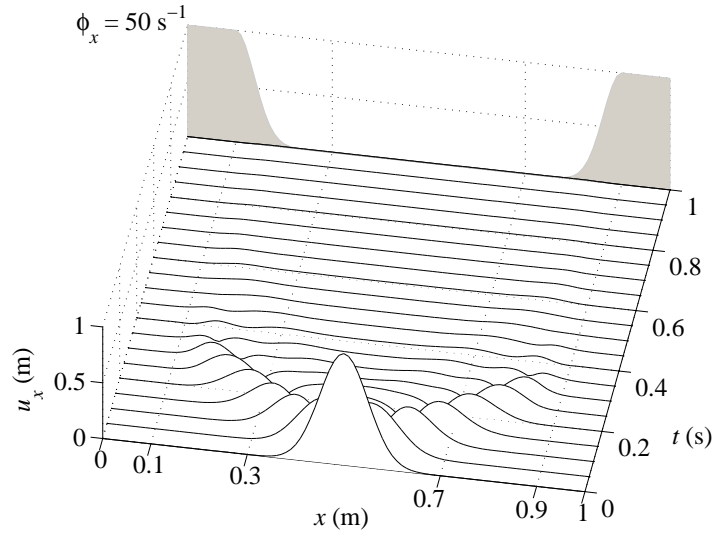
Figure 66. x-directed displacement at $y = 0.5$ m, terminated by a PML.
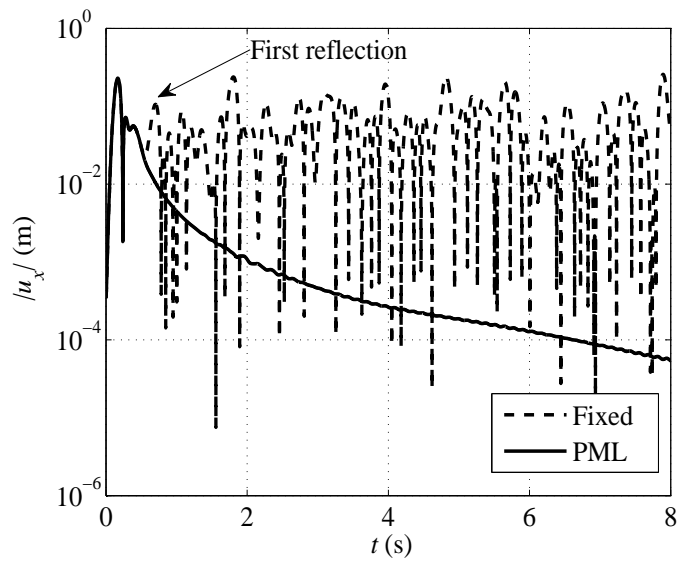
Figure 67. x-directed displacement at $x = 0.3$, $y = 0.5$ m. The solid line shows results terminated by a PML, and the dashed line used a fixed boundary condition.

where here we take $b = 1$ and $a = 0.1$. The exact solution is given by Eringen and Suhubi (*83*)

$$u(r, t) = \frac{br}{\sqrt{2}aR^6}\sqrt{R^2 + \alpha}\left(2\alpha - R^2\right),$$

$$\alpha = 1 + \frac{r^2 - c^2t^2}{a^2}, \tag{47}$$

$$R^2 = \sqrt{\alpha^2 + \frac{4c^2t^2}{a^2}},$$

where c is the longitudinal wave speed. This problem was simulated in a 2-D region, 2 m-by-2 m and $\Delta x = \Delta y = 0.01$ m, terminated by a PML with the same dimensions and magnitude as the above problem. The Gaussian kernel was used with a horizon size of $\delta = 0.75\Delta x$, with an actual cutoff of 0.028 m. The results are shown in figure 68, with the exact solution shown as the solid line and the peridynamic solution shown as the dashed line. The peridynamic solution shows good agreement with the exact solution and minimal reflections from the PML boundary.
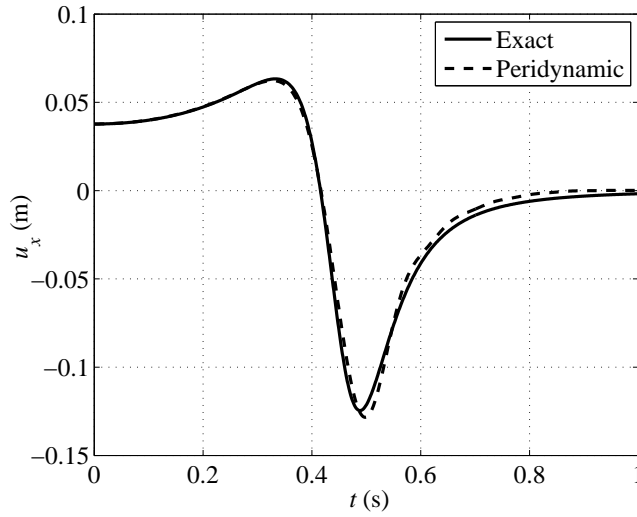
Figure 68. x-directed displacement at $x = 0.5$, $y = 0$ m. The solid line shows the exact solution and the dashed line results terminated by a PML.

10.3.2 Crack Propagation

Crack propagation in a half-space can be useful for modeling physical phenomenon such as indentation experiments. As an example, we model such a problem as a body force applied to a finite region with small pre-cracks in a region terminated on three sides with PMLs. One addition to the algorithm for this problem was a drag term, used to reduce noise. For crack problems with

79

a sudden force application, noise and oscillations can cause hot spots and undesirable cracking. To remedy this, a drag term can be added to smooth oscillations, by adjusting the nodal velocity as

$$\mathbf{v}^*[\mathbf{x}_i, l] = (1 - D)\,\mathbf{v}[\mathbf{x}_i, l] + \frac{D}{N_b}\sum_{j=1}^{N_b}\mathbf{v}[\mathbf{x}_j, l], \tag{48}$$

where D is the drag coefficient and N_b is the remaining number of bonds in the family of node n (84).

An absorbing boundary ensures that no reflections from the boundaries interfere with the crack propagation, possibly causing it to deviate. Figure 69 gives a schematic of the problem, the extent of the computation region is designated by the solid line, the PML ramp begins at the dashed line and the PML plateaus at the dotted line. The computational region was 70 mm wide and 35.25 mm high, the PML region began at 15 mm from each edge (except the top) and peaked at 5 mm to a value of 5×10^6 s^{-1}. The node spacing was 0.496 mm and the time step size was 1 ns. For material values, the density was 2235 kg/m^3, Young's modulus was 65 GPa, Poisson's ratio was 0.2, and the fracture criteria used a fracture energy of 204 J/m^2. The failure criteria used in this simulation was bond-based, i.e., a bond failed if it was stretched past a given limit, determined by the fracture energy (71). The maximum relative bond stretch was then 2.971×10^{-3}. The load was applied across a 10-mm region, centered at the top surface, with pre-cracks on each edge with a length of two nodes or 0.993 mm. The simulation was run for a total of 10 μs, and the cracks were measured manually from the edge of the pre-cracks to the extent of the damaged area.
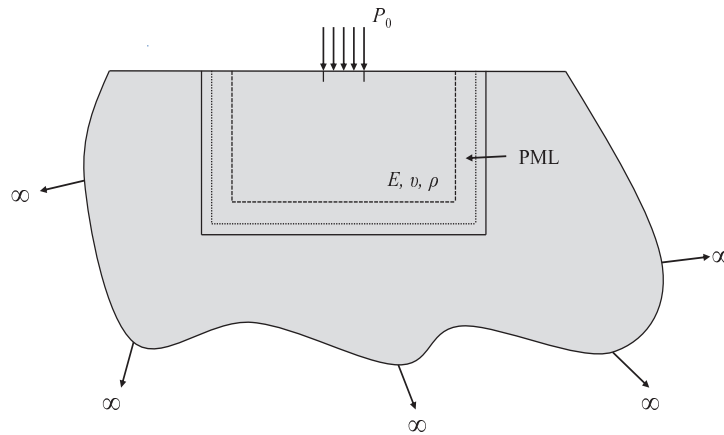
Figure 69. Schematic diagram of the problem for crack propagation in a half-space.

Figure 70 shows a result that had an applied load of 250×10^9 N, yielding a 2.11-mm crack. Figure 71 shows a close up of the damaged area from figure 70. As can be seen, the crack extends three nodes down and three nodes across. Finally, the applied load was varied between 140×10^9 N and 500×10^9 N, with the crack length versus applied load shown in figure 72 as the dots. A curve, shown as the solid line in figure 72, was fit using the form motivated by the universal scaling law presented in section 6:

$$\ell = Ap^s, \tag{49}$$

where ℓ is the crack length in meters and p is the applied load in newtons. A linear fit was computed in log-log space using least squares giving a power law of $s = 1.96$ and $A = 4.3 \times 10^{-8}$ m/N^s. This fit matches well with the predicted, dimensional analysis law shown in equation 17. Though the loading is different here, because the problem is 2-D the dimensional analysis still applies giving the correct power law form. In other words, for all 2-D problems with stable crack growth in infinite regions, we should expect a load-crack length relation similar to that of equation 49 with a power of $s = 2$, while in 3-D, we expect a power of $s = 2/3$.
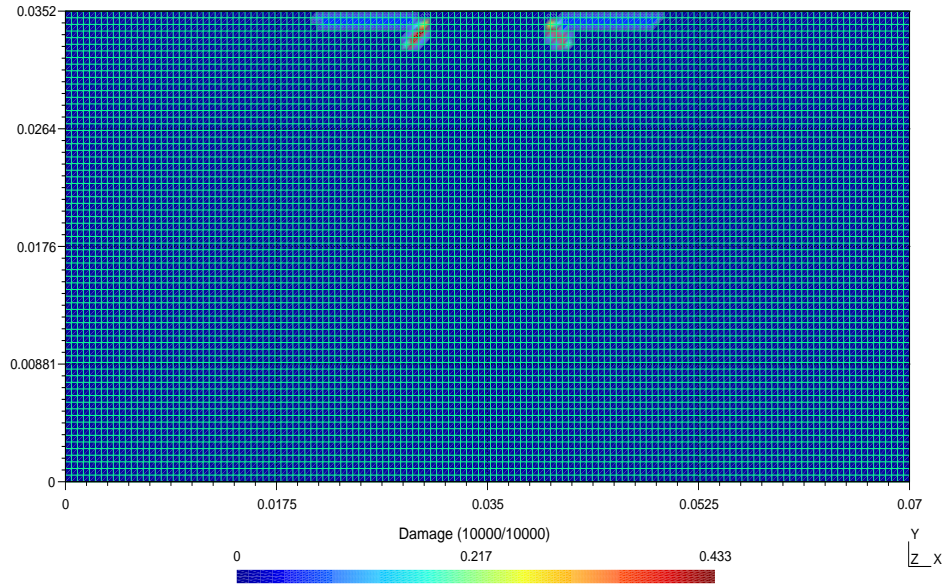
Figure 70. Damage map resulting from a 250×10^9 N applied load after 10 μs.
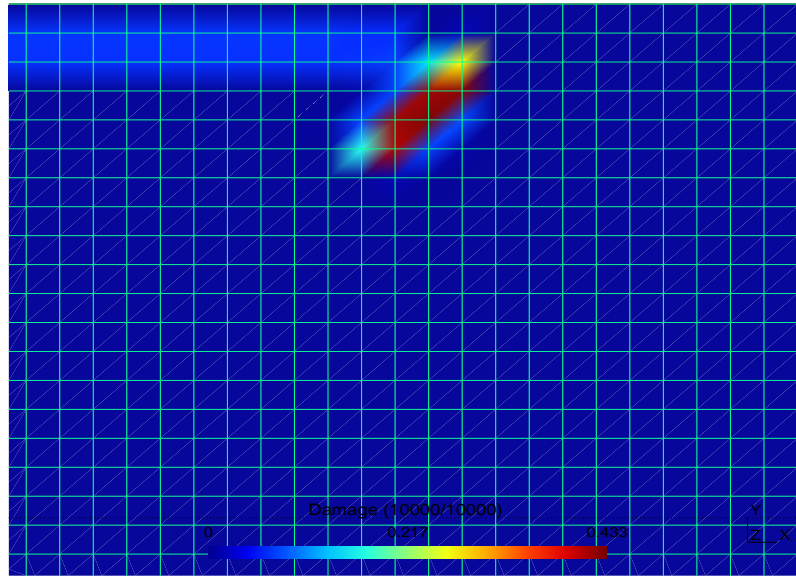
Figure 71. Close up of damage map from figure 70.
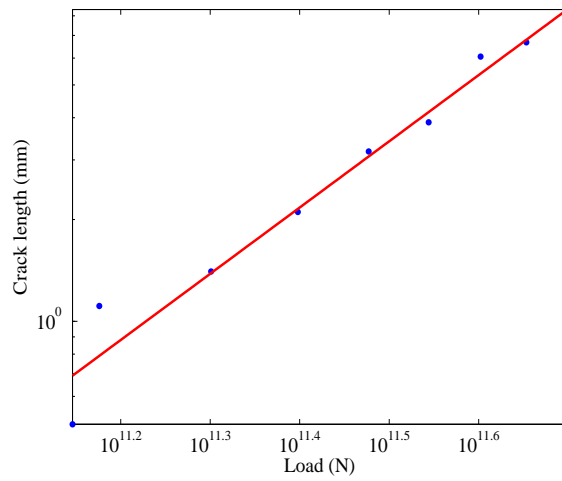
Figure 72. Crack length versus applied force for indentation into an elastic half-space using state-based peridynamics. Blue dots represent data points from the peridynamic simulation and the solid line is a curve fit.

10.3.3 Bond-based Verification of a Center Crack

A center crack opening problem was simulated with a bond-based, non-PML terminated peridynamics method. The problem, illustrated schematically in figure 41, involves applying equal but oppositely directed point loads in an infinite region. The stable crack length is related to the applied load as shown in equation 17. Here, rather than applying the load at a single node (which may cause instability or large oscillations), the load was spread over three nodes on each side at the center of a square region. Bond-based peridynamics was used with a node spacing of 0.5 mm, a time step size of 1 ns, Young's modulus of 65 GPa, density 2235 kg/m^3, and horizon size of 1.5 mm with a Heaviside shape function. The load was applied slowly with a Gaussian ramp, spread over 500 time steps. The region was not terminated with a PML, though the region size (100 mm-by-100 mm) was large enough to avoid issues associated with crack-boundary interactions. The criterion for bond damage was a critical relative stretch of 0.00185. A small pre-crack was added between the two point loads and the bonds surrounding the loads were set to a no-fail condition. This setup was run for varying loads, between 4×10^{11} and 9×10^{11} N and the crack half length was measured between the center of the region and the crack tip, with a crack tip being a region with a broken bond ratio of more than 30%. The results are shown in figure 73 on a log-log scale. As in the above example (see equation 49), a linear curve fit in log-log space (shown in figure 73 as the solid red line) was computed using least squares to determine the exponent of the power law, and found to be 1.94, very near 2, the value determined by dimensional analysis in equation 41.
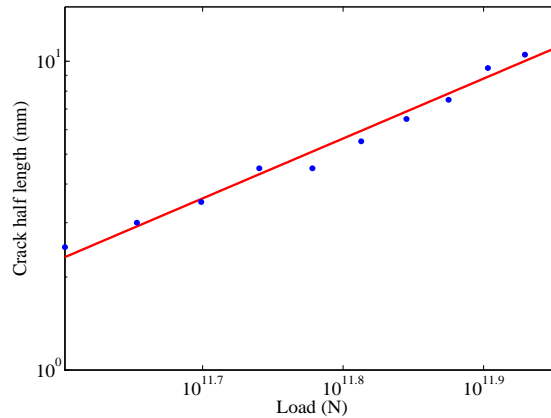
Figure 73. Crack half length versus load for a center crack problem using bond-based peridynamics.

10.3.4 Verification of an Axisymmetric Indentation Problem

Finally, the state-based, PML formulation of peridynamics was implemented in an axisymmetric setting, the details of which will be published in the future. Sneddon (*25*) derives an exact analytical solution for a flat, rigid, cylindrical indentor being pressed into an infinite elastic halfspace. Given the elastic properties of the medium, the depth of indentation, and the indentor radius, the displacement and stress can be computed for the entire region. To simulate this problem, an infinite region was represented using a PML in a finite region with a radius of 50 mm and a depth of 50 mm. The flat extent of the PML was 5 mm and the ramp region was 15 mm. The remaining parameters were identical to those in the above examples, though no bond breaking was used in this example. The indentor had a radius of 5 mm, and was pressed to a depth of 10 μm. Sneddon's exact solution (*25*) for the z-directed displacement at the surface of the halfspace is given by

$$u_z\left(r, z=0\right) = \begin{cases} \frac{2\epsilon}{\pi}\sin^{-1}\left(\frac{a}{r}\right), & r > a \\ \epsilon, & r \leq a \end{cases}, \tag{50}$$

where ϵ is the indentation depth and a is the radius of the indentor. The results of the simulation are plotted in figure 74 with the peridynamic solution shown in blue and the exact solution in red. In addition, the magnitude of the PML is indicated as the graded gray region on the right of the figure, labeled as "PML." As can be seen, the peridynamic solution is forced to zero in this region, and is not expected to match the exact solution. The main discrepancy is due to the discontinuous load applied, which leads to ringing in the peridynamic solution. Remedies for this issue will be researched in the future.
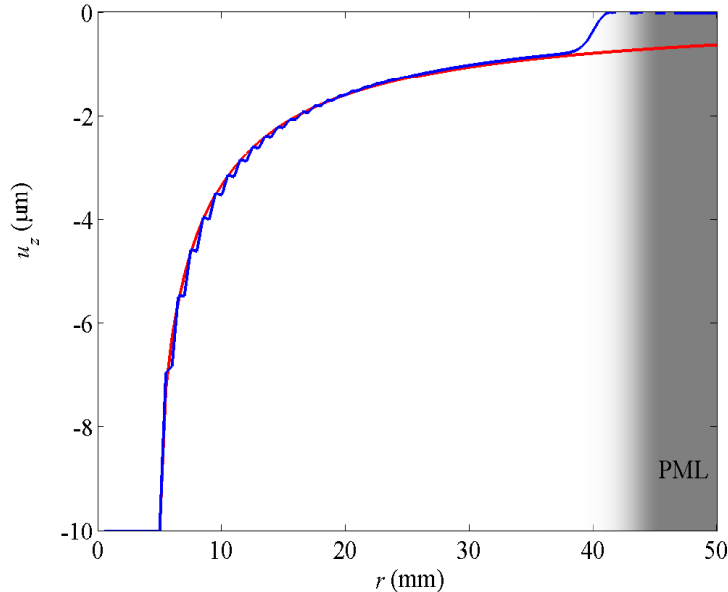
Figure 74. Peridynamic solution (blue) of an indentation problem compared with Sneddon's exact solution (*25*) (equation 50) (red).

11.   Glass Technology Short Course

A one-day short course on the "Fundamentals of Glass Science," was taught by Professor Arun K. Varshneya, Alfred University, at ARL on October 29, 2010. Course attendees received copies of Varshneya's *Fundamentals of Inorganic Glasses* (*26*). The course covered topics on (1) basic compositions and families of commercial glasses that include vitreous silicates, SL silicates, borosilicates, lead silicates, and aluminosilicates; (2) fundamentals of the glassy state; (3) phase separation and liquid-liquid immiscibility; (4) glass structures (oxide and non-oxide glasses); (5) review of some glass properties (e.g., elastic properties, hardness, viscosity, thermal expansion, durability); and (6) annealing and strengthening.

The course was well received, and a question-and-answer period ensued with questions like, "What is the difference between a glass and an amorphous material?" Answer: "Amorphous materials make a continuous or discontinuous volume transition to a crystal or vapor on heating, whereas, glasses continuously change to a liquid on heating." See also, p. 17 and 18 in Varshneya (*26*), and figure 75.
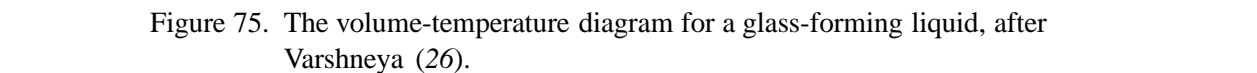
85

Figure 75. The volume-temperature diagram for a glass-forming liquid, after Varshneya (*26*).

12.   A Short-term Conceptual Project

A short-term conceptual project to determine an effective experimental and theoretical approach to model and characterize the role of glassy materials in resisting ballistic impact was conducted by Richard Lehman, Professor and Chair of the Department of Materials Science and Engineering, Rutgers University, Piscataway, NJ. A short synopsis of the report was briefed at ARL on November 17, 2011, and appears below.

A number of features of the glassy state are thought to participate in the ballistic response of glass:

- Structural relaxation/viscoelasticity/strain energy equivalence theory (SEET)

- Short- and longer-range atomic structural characteristics

- Free volume (compaction, bulking)

- Cation and anion coordination

- Bond energies

- Other nanoscale order characteristics that are difficult to determine experimentally for silicate glasses.

A number of expert personnel were contacted with the following panel discussion outcomes:

- Structural relaxation: The ability of glass to convert to a liquid with little structural adjustment compared to crystalline materials may enable glass to respond more favorably to shaped-charge assault within the microsecond time periods of the impact. Viscoelastic issues will be addressed.

- Modeling: Structural models based on statistical thermodynamics, ring structures, molecular dynamics, and, anisotropic finite element methods (FEMs) will be considered. Experimental pair distribution functions based on x-ray data will be discussed.

- Molecular defects: Glass is rich in molecular defects such as oxygen hole centers, E, bridging oxygen, non-bridging oxygen, and various ring defect structure. These defects may play an important role in the shaped-charge behavior.

- Heterogeneous structure: Most glasses are not the uniform isotropic material at the mesoscale that many scientists assume. Phase separation, cation clustering, and small-scale density fluctuations (as evidenced by various types of optical scattering) may be important in allowing glass to accommodate high strain rates.

- Free-volume: Glasses contain a large amount of free volume compared to their crystalline counterparts.

Summary and conclusions of the study include the following:

- MDs can be expanded into the mesoscale region:
    - Large atom arrays ($>10^9$) and non-cubic shapes, e.g., high aspect ratio cylinders.
    - Use surrogates to boost scale.
    - Time scale (microseconds) cannot be collapsed and is a major limit on modeling time.

- FEMs can be down-scaled to the mesoscale size region:
    - Requires specialized nonlinear methods.
    - Structural elements modeled as nonlinear elements.
    - Xi Chen at Columbia Univ. has relevant experience.

- Medium-ranged structural data obtained with scanning tunneling electron microscopy (STEM):
  - Initial material characterization.
  - Input to modeling effort.
  - Aid in interpretation of stress wave work.

- Stress wave characterization:
  - Coherent acoustic phonon spectroscopy is a promising dynamic approach.
  - The time scale is very short.
  - Experiments can be adjusted to span a range of experimental time periods.

---

13. Effect of Glass Composition on the Performance of Glass: Understand the Role of Boron Concentration on the Dynamic Properties in the Borosilicate System

---

Glass is currently used for transparent armor systems and of interest for opaque armor applications. The glasses that have been studied in previous investigations have been commercial glasses such as SL silica glass, borosilicate glass, and fused silica. Attempts to procure new glass composition have been limited to bulk glasses for compositions that have a commercial market. This is primarily due to the large capacity nature of glass production. Typical melts range from small volume of less than 1 ton a day to very large at greater than 100 tons a day. These are all greater than the needs required for small-scale evaluations for ballistic and dynamic properties. Thus, a facility at ARL-WMRD to produce small boules of glass to conduct composition-structure-property relationship studies was installed in fiscal year 2013.

Figure 76 is a photograph of a bottom loading furnace located at ARL-WMRD. It has been used for producing SL silica glass boules as shown on figure 77. These glasses were produced to understand the temperature profile and capability of the furnace. The fiscal year 2013 effort will investigate the role of boron concentration on the properties of glass. The approach is using glass frits to cast round disks of borosilicate glasses. The target compositions are the commercial Borofloat composition, the Borofloat composition with an additional 5 wt.% and the Borofloat composition with a reduced 5 wt.% of boron. Chemical analysis, quasi-static property characterization, dynamic properties characterization, and ballistic performance will be measured and reported.

Figure 76. Bottom loading furnace installed at ARL.

Figure 77. Typical glass boule produced in a silica crucible.

14. Conclusions

This third-year final report on multiscale modeling of noncrystalline ceramics (glass) has focused on establishing the framework for development of a multiscale computational methodology for optimizing or enhancing the performance of silicate-based glass materials not yet synthesized. A more immediate research objective is to understand why certain chemically substituted silica-based materials exhibit enhanced performance in the defeat of SCJs and other ballistic threats. Conclusions consistent with the milestones shown in the five-year roadmap shown in figure 3 are as follows:

1. Fused silica and various chemically substituted silicate-based specimens were delivered to ARL under the auspices of an ongoing cooperative agreement; these specimens have been ballistically tested, and serve to validate future computational models of fused silica.

2. The structural characteristics of silicate-based glasses include SRO consisting of atom to atom bond lengths that are less than 0.5 nm and bond angles characterized by RDFs and SAXS measurements. IRO in silica-based glasses consists of the polymerization of the silica atomic tetrahedra (one Si atom surrounded by four O atoms into ring structures of joined tetrahedra of a variety of sizes ranging from four to eight groups of tetrahedra). Chemical substitution of Na, K, Mg, Ca, B, and other atoms can have a profound effect on IRO and ballistic performance. Initial free volume and its variation with pressure control densification behavior, but this is difficult to measure or quantify, especially at elevated pressure. A glass brittleness parameter discussed by Ito (*4*) appears dependent on the deformation and fracture behavior, which depends on flow and densification before crack initiation and on the bond strength of the network and seems to decrease with a decrease in density.

3. A series of experiments on Borofloat, Starphire, and fused silica were conducted at the Ernst-Mach Institute in Germany, which showed that fracture and fragmentation (figure 21) of these glasses have profoundly different macroscopic response (figure 12) and fracture kinetics (table 8) useful for computational model validation. Solid cylinder impact onto fused silica targets results in a greater mass of finer fragments than the AP round, whereas the AP round results in a larger mass of greater than 2-mm-size fragments (figure 21).

4. A series of nanoindentation experiments (indenter radius = 3 μm) into fused silica were conducted at ARL, which showed that both hardness and modulus decreased with increasing

indentation depth (figure 30). Also, both radial and cone cracks were observed in indents, which exceeded 1500 nm (figures 32 and 33). The nanoindentation experiments will be used to validate MD and peridynamics models of fused silica and other chemically substituted glasses.

5. High-pressure DAC experiments were conducted at ARL to pressures of ~33 GPa and provide a means to measure density changes with pressure in glasses. Our DAC results on fused silica compared well with prior published results (*12*) and provide a means for validation of AIMD-based predictions of Hugoniots for more complex chemically substituted glasses. Preliminary measurements of neutron diffraction spectra of fused silica, Borofloat, and SL glasses provide an independent means to assess changes in glass network structure with pressure. Preliminary analysis of Raman spectroscopic measurements on several glasses with various (known) concentrations of secondary molecules reveal changes in the 300–400 wavenumber region with decreasing intensity as the composition changes within each sample (figure 28).

6. MD simulations of nanoindentation (indenter radius = 9 nm) into fused silica were conducted using LAMMPS (*85*) using a pairwise interatomic potential developed using novel FM techniques described in Izvekov and Rice (*14*) and Izvekov et al. (*86*). However, computed hardness values of 7.38 GPa underestimated experimental values determined from our own indentation experiments, using albeit larger indenters (indenter radius = 3 μm) (see figure 30).

7. The pairwise interatomic potential that was developed using a FM technique was also used to determine a shock Hugoniot for fused silica to 60 GPa; it was initially shown to be in excellent agreement with experimental values (see figure 19 on page 26 or our prior year's memorandum report (*44*). Closer examination of the structure of our silica computational model indicated that it contained regions of microcrystallinity that apparently had contributed to our excellent prediction of the shock Hugoniot for fused silica (*44*). Recomputation of the shock Hugoniot with a model free of microcrystallites resulted in a Hugoniot which overestimated the silica density relative to experimental values in the 0–20 GPa pressure range (figure 35). The extension of the pairwise FM model to include angle bending forces, which are three-body forces, is underway to improve the performance of the model at low pressures where silica densification is driven by structural and topological changes. At this time, however, we cannot rule out entirely the importance of micro/nanocrystallinity in our modeling of glass, since work by Saito et al. (*32*) using light scattering studies concluded that IRO structures, i.e., micro/nanocrystallites, exist in silica glass (see also our discussion in section 4.2.7).

8. First-principles quantum mechanical methods using VASP (*62*) are used to model densification and bulk modulus variations with pressure in fused silica. Ring size distributions (figure 46) and angle distributions for $Si - O - Si$ and $O - Si - O$ (figure 47) are calculated, and future work will consider the pressure variation of these distributions and whether they can be validated with experimental measurements conducted on fused silica under extreme pressure using diamond anvil cells. FM potentials were also determined for a borosilicate glass system (figure 52) in preparation for the fiscal year 2013 investigation of the role of boron concentration on the properties of glass using our new glass processing facility (see section 13).

9. The CASTEP code (*63*) was used to compute initial IR and Raman spectra for both crystalline and amorphous SiO_2. It was found that the calculated IR spectrum (figure 53) reproduce the main peaks observed in experiments on α-quartz (figure 54). In addition, calculated Raman spectra (figure 60) reproduced the three main regions observed in experiments on amorphous silica (figure 61).

10. Since inelastic deformation and a polyamorphic transformation apparently occurs simultaneously in some glasses, a model was developed to account for this coupled behavior, which captures the kinetics of the polyamorphic transformation that occur in plate impact experiments on borosilicate (compare for example the plate impact experiments of Alexander et al. (*23*) in figure 62a with simulation results in figure 63b.

11. We have conducted a dimensional analysis for stable crack growth in brittle elastic solids subjected to both indentation and wedge loadings and found that for Hertzian cone cracks $D = (P/K)^{2/3}$, where D is the width of the base of the cone crack, P is the indentation load, and K is the cohesive modulus; this relation is modified for 2-D stress and deformation fields $l = (P/K)^2$, where l is the crack length. This last similarity relation was used to successfully validate indentation and wedge-induced crack problems using the peridynamics computational code that was developed under this program. Fully 3-D deformation and stress fields for a rigid cylindrical indenter on an elastic halfspace were presented, which are useful for validating similar elastic field predictions by computational means prior to densification and failure of the medium.

12. A 2-D peridynamic model was developed to model nanoindentation and dynamic crack propagation in fused silica as an extension of the recent 1-D model of Wildman and Gazonas (*78*); a PML was added to permit infinite computational domains that are encountered in solution to certain boundary value problems (*87*). Peridynamic simulations of 2-D cracking induced by indentation and wedge loadings were validated using the universal

similarity relation $l = (P/K)^2$ derived in section 6. A 3-D axisymmetric peridynamics computational code was developed and verified against a closed-form solution (*25*) for vertical displacements in an elastic halfspace induced by a flat, cylindrical indenter illustrated in figure 74.

13. Preliminary material characteristic and property metrics: At this point, it is worthwhile to try articulating a set of material characteristics and properties that may have significant influence on performance of silicate-based glasses in various ballistic events and that may be controlled by systematic chemical substitutions. Among these are the following: linear thermal expansion, flash thermal conductivity, inelastic deformation (plasticity), actual density and calculated free volume, macro-defects (inclusions) and pores (bubbles), percentage of micro/nanocrystalinity and nanochemical inhomogeneities, elastic recovery, and controlled Hertzian indentation. The quasi-static and dynamic stress-strain measurements are so susceptible to almost unavoidable surface flaws that there use is still problematic.

14. The current glass DSI program has successfully transitioned into a core mission program within WMRD for fiscal year 2013 and beyond. An important focus of the mission program concerns in-house production of small samples of glass to conduct controlled composition-structure-property relationship studies (see section 13). Chemical analysis, quasi-static property characterization, dynamic properties characterization, and ballistic performance will be measured and reported on a variety of chemically substituted glasses; data and measurements from this effort will provide a means to validate a parallel computational effort using DFT and MD methods for the "design" of ballistically enhanced glass formulations, which have not yet been synthesized!

---

15. Appendix - metrics

15.1 Presentations

Weingarten, N. S.; Izvekov, S.; Rice, B. M. Mechanism of densification in silica glass under pressure as revealed by a bottom-up pairwise effective interaction model, 22nd International Workshop on Computational Mechanics of Materials, Baltimore, Maryland, September 2012.

Jenkins, T. Validation of amorphous glass properties using diamond anvil Cell experiments,- talk presented at 22nd International Workshop on Computational Mechanics of Materials, Baltimore MD, September 24 - 26, 2012.

Wildman, R. A.; Gazonas, G. A. Peridynamic simulations of infinite regions using a perfectly matched layer, SEM XII Congress & Exposition on Experimental and Applied Mechanics, May, 2012, Costa Mesa, CA.

Gazonas, G. A. Multiscale modeling of noncrystalline ceramics (glass), Materials Under Extreme Dynamic Environments (MEDE) review. ARL, APG, MD, 6 December 2012.

Gazonas, G. A.; McCauley, J. W.; Batyrev, I. G.; Becker, R. C.; Patel, P.; Rice, B. M.; Weingarten, N. S. Multiscale modeling of noncrystalline ceramics (glass), ARL DSI Annual Review for Mr. Miller. ARL, ALC, MD, 13 September 2011.

Gazonas, G. A.; McCauley, J. W.; Batyrev, I. G.; Becker, R. C.; Patel, P.; Rice, B. M.; Weingarten, N. S. Multiscale modeling of noncrystalline ceramics (glass), ARL DSI Annual Review for Mr. Miller. ARL, APG, MD, 8 March 2011.

Cadel, D.; Schuster, B.; Gazonas, G. A. Grain orientation effects on fracture in aluminum oxynitride (AlON) and fused silica ($a - SiO_2$), Summer Student Symposium Presentation, ARL, APG, August 2011.

Gazonas, G. A. Multiscale modeling of noncrystalline ceramics (glass), Materials Under Extreme Dynamic Environments (MEDE) review. ARL, APG, MD, 7 March 2011.

Gazonas, G. A. Glass multiscale modeling DSI overview, Jim Chang visit on multidisciplinary scale modeling, ARL, APG, MD, 18 May 2010.

Strassburger, E.; Patel, P.; McCauley, J. W.; Templeton, D. W. Experimental methods for characterization and evaluation of transparent armor materials, In 34th International Conference and Exposition on Advanced Ceramics and Composites, Daytona Beach, FL, 2010.

[†]Gazonas, G. A.; McCauley, J. W.; Patel, P. Multiscale modeling of non-crystalline ceramics (glass), Presentation at the 37th International Conference and Exposition on Ceramics and Composites, Dayton Beach, FL, 27 January - 1 February 2013.

[†]Gazonas, G. A.; McCauley, J. W.; Patel, P.; Batyrev, I.; Becker, R.; Izvekov, S.; Jenkins, T.; Rice, B.; Schuster, B.; Weingarten, N.; Kilcewski, S.; Wildman, R. Multiscale modeling of non-crystalline solids, International Congress on Glass, Prague, 1-5 July 2013

[†]Paper accepted yet withdrawn for apparent budgetary considerations

15.2 Publications

Wildman, R. A.; Gazonas, G. A. *A perfectly matched layer for peridynamics in one dimension*; ARL-TR-5626; U.S. Army Research Laboratory: Aberdeen Proving Ground, MD, August, 2011.

Wildman, R. A.; Gazonas, G. A. A perfectly matched layer for peridynamics in two dimensions. *J. Mech. Mater. and Struct.* **2013**, 7 (8-9), 765-781.

Izvekov, S.; Rice, B. M. Mechanism of densification in silica glass under pressure as revealed by bottom-up pairwise effective interaction model; *J. Chem. Phys.* **2012**, 136 (13), 134508.

‡Grujicic, M.; Bell, W. C.; Pandurangan, B.; Cheeseman, B.A.; Patel, P.; Gazonas, G.A. Inclusion of material non-linearity and inelasticity into a continuum-level material model for soda-lime glass. *J. Mater. and Des.* **2012**, 35, 144-155.

‡Souza, F.; Allen, D. H.; Modeling the transition of microcracks into macrocracks in heterogeneous media using a two-way coupled multiscale model. *Intl. J. Solids Structures* **2011**, 48, 3160-3175. (Scientific Services Program administered by Battelle under contract W911NF−07−D−0001; TCN 09-201).

‡Grujicic, M.; Pandurangan, B.; Zhang, Z.; Bell, W.C.; Gazonas, G. A.; Patel, P.; Cheeseman, B. A. Molecular-level analysis of shock-wave physics and derivation of the Hugoniot relations for fused silica. *J. Mater. Eng.* **2011**, Perf., DOI: 10.1007/s11665-011-0005-2.

‡Grujicic, M.; Pandurangan, B.; Bell, W. C.; Cheeseman, B. A.; Patel, P.; Gazonas, G. A. Molecular-level analysis of shock-wave physics and derivation of the Hugoniot relations for soda-lime glass. *J. of Mater. Sci.* **2011**, 46 (22), 7298-7312.

Gazonas, G. A.; McCauley, J. W.; Batyrev, I. G.; Becker, R. C.; Izvekov, S.; Jenkins, T. A.; Patel, P.; Rice, B. M.; Schuster, B. E.; Weingarten, N. S.; Wildman, R. A. *Multiscale modeling of non-crystalline ceramics (glass) (final report)*; ARL-TR-6353; U.S. Army Research Laboratory: Aberdeen Proving Ground, MD, February 2013.

Gazonas, G. A.; McCauley, J. W.; Batyrev, I. G.; Becker, R. C.; Izvekov, S.; Patel, P.; Rice, B. M.; Schuster, B. E.; Weingarten, N. S.; Wildman, R. A. *Multiscale modeling of non-crystalline ceramics (glass) (FY11)*; ARL-MR-0802; U.S. Army Research Laboratory: Aberdeen Proving Ground, MD, January 2012.

---

‡Funded in part by the Glass DSI program.

Gazonas, G. A.; McCauley, J. W.; Batyrev, I. G.; Becker, R. C.; Patel, P.; Rice, B. M.; Weingarten, N.S. *Multiscale modeling of non-crystalline ceramics (glass)*; ARL-MR-0765; U.S. Army Research Laboratory: Aberdeen Proving Ground, MD, February 2011.

Strassburger, E.; Bauer, S.; Hunzinger, M.; *Analysis of the fragmentation of AlON and bi-modal grain sized Spinel, Final Report Report E 36/12*; Research period: 10/2010-10/2011; Contract No. W911NF-10-2-0100 Contractor: Fraunhofer-Gesellschaft zur Förderung der angewandten Forschung e.V.

‡Becker, R. *Formulation of a glass model to capture observations from high-rate ballistic penetration*; ARL-TR-6086; U.S. Army Research Laboratory: Aberdeen Proving Ground, MD, August, 2012.

15.3   Personnel Hires

An Oak Ridge Institute of Science and Education (ORISE) post-doctoral fellow was hired in FY12 and offered a full-time government position in FY13. An ORISE summer student was hired in FY11.

15.4   Transition to Core

The DSI program has been transitioned to a core mission program in WMRD for fiscal year 2013 and beyond. In addition, a glass processing facility (infrastructure enhancement) has been established in WMRD to produce small samples of glass to conduct composition-structure-property relationship studies as part of the new core mission program.

15.5   Computational Code Development

The 1-, 2-, and 3-D axisymmetric peridynamics codes with PMLs capable of modeling wave propagation and fracture in brittle materials have been developed and verified under this DSI program.

15.6   Other

A one-day short course on the "Fundamentals of Glass Science," which was taught by Professor Arun K. Varshneya, Alfred University, at ARL on October 29, 2010. Course attendees received copies of Varshneya's *Fundamentals of Inorganic Glasses* (*26*).

A short-term conceptual project to determine an effective experimental and theoretical approach to model and characterize the role of glassy materials in resisting ballistic impact was conducted by Professor Richard Lehman, Rutgers University. A short synopsis of this project was briefed at ARL on 17 November, 2011 (section 12).

Seminars: "Atomistic Simulations of Vitreous Silica," Cormack, A. N., and Inamori, K., School of Engineering, NY State College of Ceramics, Alfred University, 9 January 2012.

INTENTIONALLY LEFT BLANK.

16. References

1. Moran, B.; Glenn, L. A.; Kusubov, A. Jet penetration in glass. *J. Phys. IV* **1991**, *1 (C3)*, 147–154.

2. Frye, K. *Modern Mineralogy*; Prentice-Hall, Inc.: Englewood Cliffs, NJ, 1974.

3. Bando, Y.; Ito, S.; Tomozawa, M. Direct observation of crack tip geometry of SiO_2 glass by high-resolution electron microscopy. *J. Am. Ceram. Soc.* **1984**, *67* (3), C36-C37.

4. Ito, S. Structural study on mechanical behavior of glass. *J. Ceram. Soc. Jpn.* **2004**, *112* (1309), 477–485.

5. Wilantewicz, T. E. *Failure behavior of glass and aluminum oxynitride (AlON) tiles under spherical indenters*; ARL-TR-5180; U.S. Army Research Laboratory: Aberdeen Proving Ground, MD 2010.

6. Strassburger, E.; Patel, P.; McCauley, J.; Templeton, D. W. High-speed photographic study of wave and fracture propagation in fused silica. In *Proceedings of the 22nd International Symposium on Ballistics*, Vancouver, BC, 2005.

7. Strassburger, E.; Bauer, S.; Hunzinger, M. Analysis of the fragmentation of AlON and bi-modal grain sized spinel. In *Interim Report, Report E 39/11, Contract No. W911NF-10-2-0100*, 2011.

8. Mackenzie, J. D. High-pressure effects on oxide glasses: I, densification in rigid state. *J. Am. Ceram. Soc.* **1963**, *46 (10)*, 461–470.

9. Roy, R.; Cohen, H. M. Effects of high pressure on glass: a possible piezometer for the 100-kilobar region. *Nature* **1961**, *190 (4778)*, 789–799.

10. Christiansen, E. B.; Kistler, S. S.; Gogarty, W. B. Compressibility of silica glasses as a means of determining distribution of force in high pressure cells. *J. Am. Ceram. Soc.* **1962**, *45 (4)*, 172–177.

11. Bridgman, P. W.; Simon, I. Effect of very high pressures on glass. *J. Appl. Phys.* **1953**, *24 (4)*, 405–413.

12. Shen, G.; Mei, Q.; Prakapenka, V. B.; Lazor, P.; Sinogeikin, S.; Meng, Y.; Park, C. Effect of helium on structure and compression behavior of SiO_2 glass. *Proc. Natl. Acad. Sci.* **2011**, *108* (15), 6004-6007.

13. Wakabayashi, D.; Funamori, N.; Sato, T.; Taniguchi, T. Compression behavior of densified SiO$_2$ glass. *Phys. Rev. B* **2011**, *84*, 144103.

14. Izvekov, S.; Rice, B. M. Mechanism of densification in silica glass under pressure as revealed by bottom-up pairwise effective interaction model. *J. Chem. Phys.* **2012**, *136* (13), 134508.

15. Sato, T.; Funamori, N. Sixfold-coordinated amorphous polymorph of SiO$_2$ under high pressure. *Phys. Rev. Lett.* **2008**, *101* (25), 255502.

16. Marsh, S. P., Ed. *LASL Shock Hugoniot Data*; University of California Press: Berkeley, CA, 1980.

17. Roesler, F. C. Brittle fractures near equilibrium. *Proc. Phys. Soc. Lond. B* **1956**, *B69*, 47–54.

18. Benbow, J. J. Cone cracks in fused silica. *Proc. Phys. Soc. Lond. B* **1960**, *B75*, 697–699.

19. Barenblatt, G. I. Scaling phenomena in fatigue and fracture. *Int. J. Fracture* **2006**, *138* (1–4), 19–35; 11th International Conference on Fracture, Torino, ITALY, MAR 20–25, 2005.

20. Scheidler, M. *On the coupling of pressure and deviatoric stress in isotropic hyperelastic materials*; ARL-TR-954; U.S. Army Research Laboratory: Aberdeen Proving Ground, MD 1996.

21. Zu, E.; Li, S.; Yu Zou, Y.; Zhao, X.; Sun, Y.; Lin, Y.; Li, H. Study of natural and synthetic quartz by Raman spectra. *Key Eng. Mat.* **2012**, *492*, 341–344.

22. Music, S.; Filipovic-Vincekovic, N.; Sekovanic, L. Precipitation of amorphous SiO_2 particles and their properties. *Braz. J. Chem. Eng.* **2011**, *28* (1), 89–94.

23. Alexander, C. S.; Chhabildas, L. C.; Reinhart, W. D.; Templeton, D. W. Changes to the shock response of fused quartz due to glass modification. *Int. J. Impact Eng.* **2008**, *35*, 1376–1385.

24. Zha, C. S.; Hemley, R. J.; Mao, H. K.; Duffy, T. S.; Mede, C. Acoustic velocities and refractive index of SiO_2 glass to 57.5 GPa by Brillouin scattering. *Phys. Rev. B* **1994**, *50*, 13105–13111.

25. Sneddon, I. N. *Fourier Transforms*; McGraw-Hill Book Company: New York, 1951.

26. Varshneya, A. K. *Fundamentals of Inorganic Glasses*; 2nd ed.; Society of Glass Technology: Sheffield, 2006.

27. Gazonas, G. A.; McCauley, J. W.; Batyrev, I. G.; Casem, D.; Clayton, J. D.; Dandekar, D. P.; Kraft, R.; Love, B. M.; Rice, B. M.; Schuster, B. E.; Weingarten, N. S. Multiscale modeling of armor ceramics: Focus on AlON. In *Proceedings of the 27th Army Science Conference*, Orlando, FL, 2010.

28. Souza, F. V.; Allen, D. H. Multiscale modeling of impact on heterogeneous viscoelastic solids containing evolving microcracks. *Int. J. Numer. Meth. Eng.* **2010**, *82* (4), 464–504.

29. Strassburger, E.; Patel, P.; McCauley, J. W.; Templeton, D. W. Experimental methods for characterization and evaluation of transparent armor materials. In *34th International Conference and Exposition on Advanced Ceramics and Composites*, Daytona Beach, FL, 2010.

30. Uhlman, D. R. Densification of alkali silicate glasses at high pressure. *J. Non-Cryst. Solids* **1973**, *13*, 89–99.

31. Zukas, J. A. *Impact Dynamics*; 1st ed.; John Wiley and Sons: New York, 1982.

32. Saito, K.; Kakiuchida, H.; Ikushima, A. J. Light scattering studies on the glass transition and the structure in silica glass. *Jap. J. Appl. Phys.* **1998**, *37 (37-1)*, 32–35.

33. Bradt, R. C.; Martens, R. L. Shattering glass cookware. *Am. Ceram. Soc. Bull.,* **2012**, *91 (7)*, 33–38.

34. Wilding, M. C.; Benmore, C. J. Structure of glasses and melts. *Rev. Mineral. Geochem.* **2006**, *63* (1), 275-311.

35. Benmore, C. J.; Soignard, E.; Amin, S. A.; Guthrie, M.; Shastri, S. D.; Lee, P. L.; Yarger, J. L. Structural and topological changes in silica glass at pressure. *Phys. Rev. B* **2010**, *81*, 054105.

36. Salmon, P. S.; Drewitt, J.; Whittaker, D.; Zeidler, A.; Wezka, K.; Bull, C. L.; Tucker, M. G.; Wilding, M. C.; Guthrie, M.; Marrocchelli, D. Density-driven structural transformations in network forming glasses: a high-pressure neutron diffraction study of GeO_2 glass up to 17.5 GPa. *J. Phys.: Condens. Mat.* **2012**, *24* (41), 415102.

37. Mao, H. K.; Bell, P. M.; Shaner, J. W.; Steinberg, D. J. Specific volume measurements of Cu, Mo, Pd, and Ag and calibration of the ruby R1 fluorescence pressure gauge from 0.06 to 1 Mbar. *J. Appl. Phys.* **1978**, *49 (6)*, 3276–3282.

38. Oliver, W. C.; Pharr, G. M. Measurement of hardness and elastic modulus by instrumented indentation: Advances in understanding and refinements to methodology. *J. Mater. Res.* **2004**, *19* (1), 3-20.

39. Izvekov, S.; Swanson, J. Using force-matching to reveal essential differences between density functional in ab initio molecular dynamics simulations. *J. Chem. Phys.* **2011**, *134 (19)*, 194109.

40. Saraev, D.; Miller, R. E. Atomistic simulation of nanoindentation into copper multilayers. *Model. Simul. Mater. Sci. Eng.* **2005**, *13* (7), 1089-1099.

41. Janakiraman, N.; Aldinger, F. Yielding, strain hardening, and creep under nanoindentation of precursor-derived $Si - C - N$ ceramics. *J. Am. Ceram. Soc.* **2010**, *93* (3), 821-829.

42. Nomura, K.; Chen, Y.-C.; Kalia, R. K.; Nakano, A.; Vashishta, P. Defect migration and recombination in nanoindentation of silica glass. *Appl Phys. Lett.* **2011**, *99* (11).

43. Chen, Y.-C.; Nomura, K.; Kalia, R. K.; Nakano, A.; Vashishta, P. Molecular dynamics nanoindentation simulation of an energetic material. *Appl Phys. Lett.* **2008**, *93* (17).

44. Gazonas, G. A.; McCauley, J. W.; Batyrev, I. G.; Becker, R. C.; Izvekov, S.; Patel, P.; Rice, B. M.; Schuster, B. E.; Weingarten, N. S.; Wildman, R. A. *Multiscale modeling of non-crystalline ceramics (glass) (FY11)*; ARL-MR-0802; U.S. Army Research Laboratory: Aberdeen Proving Ground, MD January 2012.

45. Plimpton, S. J. Fast parallel algorithms for short-range molecular dynamics. *J. Comput. Phys.* **1995**, *117* (1), 1–19.

46. Pedone, A.; Malavasi, G.; Menziani, M. C.; Cormack, A. N.; Segre, U. A new self-consistent empirical interatomic potential model for oxides, silicates, and silica-based glasses. *J. Phys. Chem. B* **2006**, *110* (24), 11780–11795.

47. Chen, S. D.; Ke, F. J. MD simulation of the effect of contact area and tip radius on nanoindentation. *Sci. China Ser. G-Phys. Astron.* **2004**, *47* (1), 101-112.

48. Miyake, K.; Fujisawa, S.; Korenaga, A.; Ishida, T.; Sasaki, S. The effect of pile-up and contact area on hardness test by nanoindentation. *Jap. J. Appl. Phys.* **2004**, *43* (7B),

4602–4605; 11th International Colloquium on Scanning Probe Microscopy (ICSPM 11), Haitsu, Japan, December 11-13, 2003.

49. Oliver, W. C.; Pharr, G. M. An improved technique for determining hardness and elastic modulus using load and displacement sensing indentation experiments. *J. Mater. Res.* **1992**, *7* (6), 1564–1583.

50. Barenblatt, G. I. The mathematical theory of equilibrium cracks in brittle fracture. *Adv. Appl. Mech.* **1962**, 7, 55–129.

51. Sedov, L. I. *Similarity and Dimensional Methods in Mechanics*; 10th ed.; CRC Press, Inc.: Boca Raton, FL, 1993.

52. Buckingham, E. On physically similar systems; illustrations of the use of dimensional equations. *Phys. Rev.* **1914**, *4*, 345–376.

53. Boussinesq, M. J. *Applications des potentiels à l'étude de l'équilibre et du mouvement des solides élastiques*; Gauthier-Villars: Paris, 1885.

54. Love, A. Boussinesq problem for a rigid cone. *Q. J. Math.* **1939**, *10*, 161–175.

55. Sneddon, I. N. Boussinesq's problem for a flat-ended cylinder. *Math. Proc. Camb. Phil. Soc.* **1946**, *42*, 29–39.

56. Harding, J. W.; Sneddon, I. N. The elastic stresses produced by the indentation of the plane surface of a semi-infinite elastic solid by a rigid punch. *Proc. Camb. Phil. Soc.* **1945**, *41*, 16–26.

57. Titchmarsh, E. C. *An Introduction to the Theory of Fourier Integrals*; Oxford: London, 1937.

58. Fischer-Cripps, A. C. *Introduction to Contact Mechanics*; Springer: New York, 2007.

59. Barquins, M.; Maugis, D. Adhesive contact of axisymmetric punches on an elastic half-space: the modified Hertz-Huber's stress tensor for contacting spheres. *J. Mec. Theor. Appl.* **1982**, *1* (2), 331–357.

60. Dahan, M. Contact between an axisymmetric punch and a semi-infinite transversely isotropic elastic body . *J. Mec. Appl.* **1979**, *3* (3), 373–386.

61. Mauri, F.; Pasquarello, A.; Pfrommer, B.; Yoon, Y.; Louie, S. $Si - O - Si$ bond-angle distribution in vitreous silica from first-principles Si-29 NMR analysis. *Phys. Rev. B* **2000**, *62* (8), R4786-R4789.

62. Kresse, G.; Hafner, J. Norm-conserving and ultrasoft pseudopotentials for first-row and transition-elements. *J. Phys.: Condens. Mat.* **1994**, *6* (40), 8245–8257.

63. Clark, S. J.; Segall, M. D.; Pickard, C. J.; Hasnip, P. J.; Probert, M. J.; Refson, K.; Payne, M. C. First principles methods using CASTEP. *Z. Kristall.* **2005**, *220* (5-6), 567-570.

64. Batyrev, I. G.; Tuttle, B.; Fleetwood, D. M.; Schrimpf, R. D.; Tsetseris, L.; Pantelides, S. T. Reactions of water molecules insilica-based network glasses. *Phys. Rev. Lett.* **2008**, *100* (10), 105503–105508.

65. Deschamps, T.; Kassir-Bodon, A.; Sonneville, C.; Margueritat, J.; Martinet, C.; de Ligny, D.; Mermet, A.; Champagnon, B. Permanent densification of compressed silica glass: a Raman-density calibration curve. *J. Phys.: Condens. Mat.* **2013**, *25* (2), 025402–025406.

66. Gazonas, G. A.; McCauley, J. W.; Batyrev, I. G.; Becker, R. C.; Patel, P.; Rice, B. M.; Weingarten, N. S. *Multiscale modeling of non-crystalline ceramics (glass)*; ARL-MR-0765; U.S. Army Research Laboratory: Aberdeen Proving Ground, MD 2011.

67. Sugiura, H.; Kondo, K.; Sawaoka, A. Dynamic response of fused quartz in the permanent densification region. *J. Appl. Phys.* **1981**, *52*, 3375–3382.

68. Silling, S. A. Reformulation of elasticity theory for discontinuities and long-range forces. *J. Mech. Phys. Solids* **2000**, *48* (1), 175–209.

69. Demmie, P. N.; Silling, S. A. An approach to modeling extreme loading of structures using peridynamics. *J. Mech. Mater. Struct.* **2007**, *2* (10), 1921–1945.

70. Gerstle, W.; Sau, N.; Silling, S. Peridynamic modeling of plain and reinforced concrete. In *18th International Conference on Structural Mechanics in Reactor Technology*, Beijing, China, 2005.

71. Ha, Y. D.; Bobaru, F. Studies of dynamic crack propagation and crack branching with peridynamics. *Int. J. Fracture* **2010**, *162* (1-2), 229–244.

72. Emmrich, E.; Weckner, O. Analysis and numerical approximation of an integrodifferential equation modeling non-local effects in linear elasticity. *Mathematics and Mechanics of Solids* **2005**, *12* (4), 363–384.

73. Kilic, B.; Agwai, A.; Madenci, E. Peridynamic theory for progressive damage prediction in center-cracked composite laminates. *Compos. Struct.* **2009**, *90* (2), 141–151.

74. Silling, S.; Askari, E. A meshfree method based on the peridynamic model of solid mechanics. *Comput. Struct.* **2005**, *83* (17-18), 1526–1535.

75. Silling, S. A.; Epton, M.; Weckner, O.; Xu, J.; Askari, E. Peridynamic states and constitutive modeling. *J. Elasticity* **2007**, *88* (2), 151–184.

76. Berenger, J. A perfectly matched layer for the absorption of electromagnetic-waves. *J. Comput. Phys.* **1994**, *114* (2), 185–200.

77. Chew, W.; Weedon, W. A 3D perfectly matched medium from modified Maxwell's equations with stretched coordinates. *Microw. Opt. Tech. Lett.* **1994**, 7 (13), 599–604.

78. Wildman, R. A.; Gazonas, G. A. *A perfectly matched layer for peridynamics in one dimension*; ARL-TR-5626; U.S. Army Research Laboratory: Aberdeen Proving Ground, MD 2011.

79. Du, Q.; Gunzburger, M. D.; Lehoucq, R. B.; Zhou, K. *A nonlocal vector calculus, nonlocal volume-constrained problems, and nonlocal balance laws*; SAND 2010-8353J; Sandia National Laboratories: Sandia, NM 2010.

80. Malvern, L. *Introduction to the Mechanics of a Continuous Medium*; Prentice-Hall: NJ, 1969.

81. Foster, J. T.; Silling, S. A.; Chen, W. W. Viscoplasticity using peridynamics. *Int. J. Numer. Meth. Eng.* **2010**, *81*, 1242–1258.

82. Johnson, S. G. Notes on Perfectly Matched Layers. http://math.mit.edu/ ~stevenj/18.369/pml.pdf, (accessed 2010).

83. Eringen, A. C.; Suhubi, E. S. *Elastodynamics, Vol. II, Linear Theory*; Academic Press: New York, 1975.

84. Becker, R.; Lucas, R. J. *An assessment of peridynamics for pre and post failure deformation*; ARL-TR-5811; U.S. Army Research Laboratory 2011.

85. Plimpton, S. J. *LAMMPS Users Manual: Large-scale Atomic/Molecular Massively Parallel Simulator*; Sandia Corporation: Sandia National Laboratories, 2003.

86. Izvekov, S.; Parrinello, M.; Burnham, C. J.; Voth, G. A. Effective force fields for condensed phase systems from ab initio molecular dynamics simulation: A new method for force-matching. *J. Chem. Phys.* **2004**, *120* (23), 10896–10913.

87. Wildman, R. A.; Gazonas, G. A. A perfectly matched layer for peridynamics in two dimensions. *J. Mech. Mater. Struct.* **2012**, *7 (8-9)*, 765-781.

List of Symbols, Abbreviations, and Acronyms

1-D	one-dimensional
2-D	two-dimensional
$\alpha\text{-}SiO_2$	crystalline quartz
Al	aluminum
$AlON$	aluminum oxynitride
ARL	U.S. Army Research Laboratory
AIMD	ab initio molecular dynamics
a-SiO_2	fused silica or amorphous quartz
B	boron
Ca	calcium
CSM	continuous stiffness measurement
DAC	diamond anvil cell
DSI	Director's Strategic Initiative
EOI	edge-on-impact
EOS	equation of state
FEM	finite element method
FIB	focused-ion-beam
HEL	Hugoniot elastic limit
IRO	intermediate-range order
LAMMPS	large-scale atomic/molecular massively parallel simulator
LB	less brittle
MD	molecular dynamics
Na	sodium
MEDE	materials in extreme dynamic environments
O	oxygen
PAW	projector augmented wave
PML	perfectly matched layer
RDF	radial distribution function
SAXS	small-angle x-ray scattering
SCJ	shaped-charge jet
SEET	strain energy equivalence theory
SEM	scanning electron microscopy

Si	silicon
SiC	silicon carbide
SL	soda lime
SRO	short-range order
STEM	scanning tunneling electron microscopy
VASP	Vienna ab initio simulation package
WMRD	Weapons and Materials Research Directorate

110

INTENTIONALLY LEFT BLANK.